Measurement of jet substructure in boosted $t\bar{t}$ events with the ATLAS detector using 140 fb^{-1} of 13 TeV pp collisions

G. Aad *et al.*[*]
(ATLAS Collaboration)

(Received 8 December 2023; accepted 8 May 2024; published 21 June 2024)

Measurements of the substructure of top-quark jets are presented, using 140 fb^{-1} of 13 TeV pp collision data recorded with the ATLAS detector at the LHC. Top-quark jets reconstructed with the anti-k_t algorithm with a radius parameter $R = 1.0$ are selected in top-quark pair ($t\bar{t}$) events where one top quark decays semileptonically and the other hadronically, or where both top quarks decay hadronically. The top-quark jets are required to have transverse momentum $p_{\mathrm{T}} > 350$ GeV, yielding large samples of data events with jet p_{T} values between 350 and 600 GeV. One- and two-dimensional differential cross sections for eight substructure variables, defined using only the charged components of the jets, are measured in a particle-level phase space by correcting for the smearing and acceptance effects induced by the detector. The differential cross sections are compared with the predictions of several Monte Carlo simulations in which top-quark pair-production quantum chromodynamic matrix-element calculations at next-to-leading-order precision in the strong coupling constant α_{S} are passed to leading-order parton shower and hadronization generators. The Monte Carlo predictions for measures of the broadness, and also the two-body structure, of the top-quark jets are found to be in good agreement with the measurements, while variables sensitive to the three-body structure of the top-quark jets exhibit some tension with the measured distributions.

DOI: 10.1103/PhysRevD.109.112016

I. INTRODUCTION

Observation of the production and decay of top quarks in high-energy proton-proton (pp) collisions has provided information about the production of massive particles through the strong force. The Large Hadron Collider (LHC) has enabled the collection of large samples of top-quark events and the measurement of top-quark production processes with excellent kinematic resolution [1–4]. These results have been compared with quantum chromodynamics (QCD) calculations at lowest order in the strong coupling constant α_{s}, as well as next-to-leading-order (NLO) and next-to-next-to-leading-order (NNLO) results. The top-quark decay process and the resulting parton-showering and hadronization effects have been measured with less precision. This paper reports a measurement of the substructure observed in high transverse-momentum (p_{T}) top-quark jets produced in pp collisions at a center-of-mass energy of 13 TeV using 140 fb^{-1} of data recorded by the ATLAS detector.

The large top-quark pair-production ($t\bar{t}$) cross section at the LHC allows detailed studies of the substructure of jets arising from light quarks, b-quarks, and gluons, as well as large-radius jets containing the decay products of boosted top quarks. It also allows tests of the Standard Model (SM) at both the top-quark mass scale relevant for substructure measurements and the TeV scales relevant for jet production measurements [5,6]. Furthermore, effects beyond the SM can appear as deviations of top-quark jet substructure from the SM predictions [7–11] that may not be detectable with inclusive cross-section measurements. A precise measurement of top-quark differential cross sections as a function of several complementary substructure variables therefore tests SM predictions and increases the sensitivity to possible effects beyond the SM. Top-quark jet substructure variables are also employed in the development of sophisticated taggers, used to separate top-quark jets from energetic jets arising from lighter quarks or gluons [12–14]. These taggers are used in measurements and searches targeting final states including highly energetic top quarks [15–20].

The SM predicts that top quarks decay into a W boson and a b-quark almost 100% of the time. In the cases where the W boson decays hadronically ($W \to q\bar{q}'$), the final state consists of an all-hadronic top-quark decay with three charged decay products. The resulting quarks and gluons shower and hadronize to form semistable objects that can

[*]Full author list given at the end of the article.

be studied as a single, collimated system when the top quark is produced at high p_{T}, above approximately 300 GeV. This top-quark jet remains connected to the rest of the event through color connections, specifically to additional radiation and the other top quark's decay products. Measurements of the substructure of these top-quark jets test the models used to describe this decay, the parton shower, and the hadronization process.

Interest in the properties of jets, both experimental and theoretical, extends back several decades and remains an active area of study [21]. At the LHC, measurements of jet substructure have been performed in proton-proton collisions by the ATLAS, CMS, ALICE, and LHCb collaborations in several topologies, as dijet and inclusive jet production [22–38], electroweak boson production and top-quark production [28,30,37,39–46]. The substructure studies examined variables based on energy flow within the jet, such as angularity, planar flow, and jet mass, and also variables that are sensitive to the three-prong structure of the top-quark jet, such as N-subjettiness and energy correlation variables. These measurements indicated possible disagreement with the SM predictions for some substructure variables, although most of the measurements were limited by large statistical and systematic uncertainties. In addition, the measurements focusing on jets from top-quark decays typically involved a lower average jet p_{T} than employed in the analysis reported here. At higher p_{T}, the three-body structure of high-p_{T} top-quark jets is less well defined because the three partons are more collimated, making it more difficult to separate out their showers.

The measurements reported here are performed in two independent channels, using two classes of $t\bar{t}$ final states, the lepton + jets (ℓ + jets) channel where one top quark has decayed semileptonically and the other hadronically, and the all-hadronic final state where both top quarks have decayed hadronically. Even though the top-quark jet substructure in the two channels is described by the same underlying theory, the different final states require different approaches to their selection and reconstruction to separate the signal events from the background, giving rise to differing effects on the resolution, uncertainty and shape of the measured observables. In addition, the two final states differ in the amount of final-state radiation.

In both channels, reconstructed top-quark jets with $p_{\mathrm{T}} > 350$ GeV are used to measure the substructure variables by "unfolding" detector effects to stable-particle level in order to obtain differential cross-section measurements. These unfolded variables are defined in specific kinematic regions, or fiducial phase-spaces, in order to avoid significant extrapolation of results from the kinematic region in which the measurements are made to the region in which they are compared with predictions. The ℓ + jets fiducial phase-space is characterized by the requirement of a single lepton, a top-quark jet with $p_{\mathrm{T}} > 350$ GeV and an additional jet arising from the b-quark hadronization. The all-hadronic fiducial phase-space is defined by requiring two top-quark jets, each containing a b-hadron, with one jet having $p_{\mathrm{T}} > 500$ GeV and a second jet having $p_{\mathrm{T}} > 350$ GeV, and the absence of isolated leptons. Only the charged components of the top-quark jets are considered when defining the substructure, as the substructure measurements using this approach have higher resolution than those using a combination of charged and neutral components. The unfolded differential cross sections are then compared with the predictions of different Monte Carlo (MC) generators. The top-quark pair-production matrix element is calculated at NLO precision in QCD. The modeling of radiation beyond the first emission, the top-quark decay, and the showering is at leading-order (LO) precision, and the hadronization is described by a phenomenological model. These predictions are referred to later in the text as NLOME + PS.

The measured substructure variables are the N-subjettiness variable τ_3, as well as the ratios $\tau_{32} \equiv \tau_3/\tau_2$ and $\tau_{21} \equiv \tau_2/\tau_1$ [47,48], the normalized energy-correlation function $ECF2$, as well as the associated variables D_2 and C_3 [49,50], and the Les Houches angularity LHA and the scaled p_{T} dispersion $p_{\mathrm{T}}^{\mathrm{d},*}$, which are two generalized angularities [51]. This list of variables has been selected to provide complete and condensed information about the jet substructure while taking into consideration multiple factors: sensitivity to the differences between NLOME + PS predictions, resolution, minimal correlation among the measured variables, and their relevance in tagging algorithms.

The results are intended to complement the recent measurements of top-quark jet substructure performed by the ATLAS [42] and CMS [43] collaborations by including several new features. The measurement focuses on boosted top quarks, and the inclusion of an all-hadronic channel allows the substructure to be studied for top-quark jets with an average p_{T} around 500 GeV for the first time. In addition, using tracks to reconstruct the substructure improves the resolution, with the diagonal elements of the migration matrix increasing by approximately 50%, and also leads to lower uncertainties than in the previous results.

The paper is organized as follows. Section II describes the ATLAS detector, while Sec. III presents the data and simulation samples used in the measurements. Both the reconstruction of lepton and jet candidates and the event selection is explained in Sec. IV. The estimation of the backgrounds in the selected $t\bar{t}$ final states is described in Sec. V. The measured substructure variables are defined in Sec. VI and the unfolding is described in Sec. VII. Systematic uncertainties are discussed in Sec. VIII. The results are presented in Sec. IX, where the comparison with theoretical predictions is also discussed. Finally, a summary is presented in Sec. X.

II. ATLAS DETECTOR

The ATLAS detector [52] at the LHC covers nearly the entire solid angle around the collision point.[1] It is a multipurpose detector consisting of an inner tracking detector (ID) surrounded by a thin superconducting solenoid, electromagnetic and hadronic sampling calorimeters, and a muon spectrometer incorporating three large superconducting air-core toroidal magnets.

The ID is immersed in a 2 T axial magnetic field and provides charged-particle tracking in the range $|\eta| < 2.5$. The calorimeter system covers the pseudorapidity range $|\eta| < 4.9$. Within the region $|\eta| < 3.2$, electromagnetic calorimetry is provided by barrel and end cap high-granularity lead/liquid-argon (LAr) calorimeters. Hadron calorimetry is provided by the steel/scintillator-tile calorimeter, segmented into three barrel structures within $|\eta| < 1.7$, and two copper/LAr end cap hadron calorimeters. The muon spectrometer (MS) comprises separate trigger and high-precision tracking chambers measuring the deflection of muons in a magnetic field generated by the superconducting air-core toroidal magnets.

Events of interest are selected by the first-level trigger system implemented in custom hardware, followed by selections made by algorithms implemented in software in the high-level trigger [53].

An extensive software suite [54] is used in data simulation, in the reconstruction and analysis of real and simulated data, in detector operations, and in the trigger and data acquisition systems of the experiment.

III. DATA SAMPLES, SIMULATION, AND THEORETICAL PREDICTIONS

The data were collected from LHC pp collisions at $\sqrt{s} = 13$ TeV during 2015–2018. Data quality requirements are applied to ensure that all detector components were fully operational [55]. The resulting data sample corresponds to an integrated luminosity of 140.1 fb^{-1}. The uncertainty in the combined 2015–2018 integrated luminosity is 0.83% [56], obtained using the LUCID-2 detector [57] for the primary luminosity measurements, complemented by measurements using the inner detector and calorimeters.

The $t\bar{t}\,\ell$ + jets events were selected with inclusive lepton triggers [53,58,59] that required an event to have an electron or muon candidate with $p_{\mathrm{T}} > 26$ GeV (or $p_{\mathrm{T}} > 24$ GeV and $p_{\mathrm{T}} > 20$ GeV, respectively, for electrons and muons in 2015 data). Events in the all-hadronic channel were selected inclusively using a collection of single- and double-large-R jet triggers, with the single-jet triggers using both trimmed[2] and untrimmed jets. The required p_{T} for the single-jet triggers ranged from 360 to 480 GeV, depending on the instantaneous luminosity when the data were selected. For the double-jet triggers, both large-R jets were required to have $p_{\mathrm{T}} > 330$ GeV. The lower-p_{T} jet triggers additionally required the large-R jets to have a mass above either 35 or 40 GeV, depending on the trigger. Although both the single- and double-jet triggers were employed to select the events for the all-hadronic channel, the single-jet triggers were highly efficient for events that pass the preselection described in Sec. IV C. The same trigger requirements are applied to data and simulated events; this allows corrections for trigger inefficiencies to be made in the cross-section extraction procedure described in Sec. VII.

Simulated events were produced using several MC calculations, and both the effects and response of the detector were incorporated using a simulation of the ATLAS detector [61] based on either the GEANT4 program [62] or a faster approach employing parametrized showers in the calorimeter [63]. The faster approach was only used to simulate a subset of alternative $t\bar{t}$ samples produced for the ℓ + jets channel. The data events and simulated events were processed with the same reconstruction and analysis algorithms.

The production of $t\bar{t}$ events was modeled using the POWHEG BOX v2 [64–67] generator to provide matrix elements at NLO precision with the NNPDF3.0NLO [68] parton distribution functions (PDFs) and the h_{damp} parameter[3] set to $1.5m_t$ [69], where the top-quark mass m_t was set to 172.5 GeV unless otherwise noted. To assess the effect of an uncertainty in h_{damp}, an additional $t\bar{t}$ sample with h_{damp} set to $3.0m_t$ is used. To assess the effect of a top-quark mass uncertainty, two additional $t\bar{t}$ samples were simulated with m_t set to 169 GeV and 176 GeV. These samples are used to accurately estimate the dependance on m_t of the measured observables, and estimate the uncertainty arising from a ± 0.5 GeV variation of m_t from the nominal value. The functional form of the renormalization and factorization scale was set to the default scale $\sqrt{m^2 + p_{\mathrm{T}}^2}$, where m and p_{T} represent the mass and transverse momentum of the top quark in each event. Parton showering and hadronization were modeled with the PYTHIA8.230 generator [70] using the A14 set of tuned parameters [71] and the NNPDF2.3LO set of PDFs [72]. The value of $\alpha_{\mathrm{s}}^{\mathrm{FSR}}$ set in the tuning is $\alpha_{\mathrm{s}}^{\mathrm{FSR}}(m_Z) = 0.127$.

[1] ATLAS uses a right-handed coordinate system with its origin at the nominal interaction point (IP) in the center of the detector and the z-axis along the beam pipe. The x-axis points from the IP to the center of the LHC ring, and the y-axis points upward. Cylindrical coordinates (r, ϕ) are used in the transverse plane, ϕ being the azimuthal angle around the z-axis. The pseudorapidity is defined in terms of the polar angle θ as $\eta = -\ln\tan(\theta/2)$. Angular distance is measured in units of $\Delta R \equiv \sqrt{(\Delta\eta)^2 + (\Delta\phi)^2}$.

[2] Here the trimming [60] employs a radius parameter of $R = 0.2$ and removes subjets with less than 4% of the large-R jet p_{T}.

[3] The h_{damp} parameter controls the matching in POWHEG and effectively regulates the high-p_{T} radiation against which the $t\bar{t}$ system recoils.

The uncertainty due to the parton-shower and hadronization model is estimated by comparing the results from the nominal generator setup with those from a sample produced with the POWHEG BOXv2 generator and the HERWIG7.1.3 [73,74] parton-shower and hadronization model. In this alternative sample, the HERWIG7.1 default set of tuned parameters [74,75] and the MMHT2014LO PDF set [76] were used.

An uncertainty also arises from the procedure used to match the hard-scatter and parton-shower generators. The results from the nominal generator were compared with those from a sample produced by the MADGRAPH5_AMC@NLO+PYTHIA8 generator [77]. For the calculation of the hard scattering, the MADGRAPH5_AMC@NLO2.6.0 generator (hereafter called aMC@NLO) was used with the NNPDF3.0NLO PDF set. Parton showering and hadronization were modeled with the PYTHIA 8.230 generator, using the A14 tune and the NNPDF2.3LO set of PDFs. Top quarks were decayed at LO, using the MADSPIN model [78,79] to preserve top-quark spin correlations. The shower-starting scale had the functional form $\mu_{\mathrm{q}} = H_{\mathrm{T}}/2$ [80], where H_{T} is defined as the scalar sum of the p_{T} of all outgoing partons. The renormalization and factorization scale choice was the same as for the POWHEG generator setup. Some of the PYTHIA settings used in the alternative sample differ from those in the nominal sample, since they must accommodate a different matching algorithm. One important difference concerns the matrix element (ME) corrections applied to the radiation modeled by the PYTHIA parton shower, which cannot be enabled when the PYTHIA parton-shower and hadronization model is matched to the aMC@NLO ME calculation. To remove the effects of ME corrections from the matching uncertainty, an additional POWHEG+PYTHIA sample was used in comparison with the AMC@NLO+PYTHIA 8 sample, differing from the nominal sample only in the PYTHIA ME corrections, which were disabled.

All $t\bar{t}$ samples were normalized to the cross-section prediction at NNLO in QCD including the resummation of next-to-next-to-leading logarithmic (NNLL) soft-gluon terms calculated using the TOP++ 2.0 program [81–87]. This cross section corresponds to $\sigma(t\bar{t})_{\mathrm{NNLO+NNLL}} = 832 \pm 51$ pb, where the uncertainty is due to scale variations, α_{s} and the PDFs. Their contributions are calculated using the PDF4LHC prescription [88] with the MSTW2008NNLO (68% CL) [89,90], CT10NNLO [91,92] and NNPDF2.3LO PDF sets. The samples employed for the signal modeling are filtered according to the number of leptons arising from the $t\bar{t}$ decay: only events with no leptons are used in the all-hadronic channel and only events with at least one lepton are used in the ℓ + jets channel.

In addition to the signal, the contributions of several background processes to the selected event sample are estimated using MC predictions.

The production of a top quark in association with a W boson (tW) was modeled with the POWHEG BOXv2 [65–67,93] generator at NLO in QCD, using the five-flavor scheme and the NNPDF3.0NLO set of PDFs. The diagram-removal (DR) scheme [94] was used to remove interference and overlap with $t\bar{t}$ production. The related uncertainty was estimated by comparison with an alternative sample generated using the diagram-subtraction (DS) scheme [69,94]. The PYTHIA8.230 generator modeled the parton showering and hadronization, using the A14 tune and the NNPDF2.3LO set of PDFs.

Single-top-quark t-channel production was modeled with the POWHEG BOXv2 generator at NLO in QCD, using the four-flavor scheme and the corresponding NNPDF3.0NLO PDFs. Parton showering and hadronization in these events was modeled with the PYTHIA8.230 generator using the A14 tune and the NNPDF2.3LO PDFs. Single-top s-channel production was modeled using the POWHEG BOXv2 generator at NLO in QCD in the five-flavor scheme with the NNPDF3.0NLO PDFs. Parton showering and hadronization in these events was modeled with the PYTHIA8.230 generator using the A14 tune and the NNPDF2.3LO PDFs. For both t-channel and tW-channel single-top production, an additional sample, produced with POWHEG BOXv2 and HERWIG7.04 and using the H7UE set of tuned parameters, is employed to estimate the uncertainty arising from the choice of parton-showering and hadronization models.

Simulated W/Z + jets events were produced with the SHERPA2.2.1 [95] generator using NLO matrix elements for up to two partons, and LO matrix elements for up to four partons, calculated with the Comix [96] and OPENLOOPS [97–99] libraries. They were matched with the SHERPA parton-shower model [100] using the MEPS@NLO prescription [101–104] and the set of tuned parameters developed by the SHERPA authors. The NNPDF3.0NNLO PDFs were used and the samples were normalized to a NNLO prediction [105].

The production of $t\bar{t}Z$ and $t\bar{t}W$ events was modeled using the aMC@NLO V2.3.3 generator at NLO with the NNPDF3.0NLO PDFs. Parton showering and hadronization in these events was modeled with the PYTHIA 8.210 generator using the A14 tune and the NNPDF2.3LO PDFs. The production of $t\bar{t}H$ events was modeled using the POWHEG BOXv2 [64–67,106] generator at NLO with the NNPDF3.0NLO PDFs. Parton showering and hadronization in these events was performed with PYTHIA 8.230 using the A14 tune and the NNPDF2.3LO PDFs.

Samples of diboson final states (VV) were modeled with the SHERPA 2.2.2 generator, including off-shell effects and virtual Higgs boson contributions where appropriate. The samples were generated using NLO matrix elements for up to one additional parton and at LO accuracy for up to three additional parton emissions. The matrix-element calculations were matched and merged with the SHERPA parton shower based on Catani–Seymour dipole factorization using the MEPS@NLO prescription. The virtual QCD correction were provided by the OPENLOOPS library.

The NNPDF3.0NNLO PDFs were used along with the dedicated set of tuned parton-shower parameters developed by the SHERPA authors.

The decays of bottom and charm hadrons in processes containing top quarks were simulated using the EVTGEN program [107].

In all simulated samples, the effect of multiple interactions in the same bunch crossing (pile-up) was incorporated by overlaying the hard-scattering interaction with a number of simulated inelastic pp events generated with the PYTHIA 8.186 MC generator using the NNPDF2.3LO PDFs and the A3 tune [108].

IV. EVENT RECONSTRUCTION AND SELECTION

A. Detector-level objects reconstruction

The jet substructure measurements at detector level use electron candidates, muon candidates, jet candidates, the missing transverse momentum, and charged tracks, all of which are required to be associated with the primary vertex. The primary vertex is defined as the reconstructed vertex with the highest $\sum p_{\mathrm{T}}^2$ of the associated tracks and is required to have at least two associated tracks with $p_{\mathrm{T}} > 0.5$ GeV.

Four types of jets are reconstructed independently: (1) trimmed large-R jets created from calorimeter energy deposits [109] using the anti-k_t clustering algorithm [110] with radius parameter $R = 1.0$ implemented in the FASTJET package [111], (2) small-R jets created from both tracking and calorimeter information using the particle-flow algorithm [112] and the anti-k_t algorithm with radius parameter $R = 0.4$, (3) trimmed large-R reclustered jets (RC large-R jets) created from the small-R jets using the anti-k_t algorithm with radius parameter $R = 1.0$ [113], and (4) variable-R track-jets created from ID tracks with the variable-R algorithm [114] implemented in the FASTJET package and defining jets with a p_{T}-dependent variable-radius parameter ranging between $R = 0.02$ and $R = 0.4$ in accord with a constant parameter $\rho = 30$ GeV scaling as ρ/p_{T} [115]. The two channels use different combinations of these jets in their selection.

In order to suppress jets originating from pile-up, small-R jets with $20 < p_{\mathrm{T}} < 60$ GeV and $|\eta| < 2.5$ must be associated with the primary vertex according to the jet-vertex-tagger (JVT) algorithm [116]. The small-R jet energies are corrected by using energy- and η-dependent calibration factors derived from simulation and *in situ* measurements [117]. Only small-R jets with $p_{\mathrm{T}} > 30$ GeV are employed. Large-R jets are calibrated using the local hadronic cell weighting (LCW) scheme [109], which exploits the cluster shape to provide a weighted calibration between the electromagnetic and hadronic scales [118]. The effects of pile-up and the underlying event are mitigated by the application of a trimming algorithm [60]: the constituents of the large-R jets are reclustered by the k_t algorithm [111] into smaller $R = 0.2$ jets which are removed if they comprise less than 5% of the p_{T} of the original large-R jet.

The RC large-R jet calibration is propagated from the calibration of the small-R jets that are used as input to the reclustering [119]. Most of the pile-up mitigation is thus inherited by the RC large-R jets from the techniques applied to the small-R jets. In addition, a trimming technique is applied to the RC large-R jets that removes all small-R jets comprising less than 5% of the p_{T} of the RC large-R jet. RC large-R jets are discarded if they have only one constituent to avoid a dependence on the calibration of the small-R jet mass. Such jets comprise ∼1.5% of the jets in the sample. Only RC large-R jets with $p_{\mathrm{T}} > 350$ GeV and $|\eta| < 2.0$ are considered when measuring the substructure variables.

The use of different types of large-R jets in the two $t\bar{t}$ final states is motivated by the topologies of the ℓ + jets and all-hadronic channels and the different background contamination. In the all-hadronic channel the signal is separated from the large multijet background by using a deep-neural-network (DNN) top-quark-tagging algorithm optimized for large-R jets [12]. Because this top-quark tagger employs several substructure variables, a tag-and-probe method described in Sec. VI is used to avoid biasing the measured observables in the all-hadronic channel. The DNN top-quark-tagging algorithm has not been trained and tested on RC large-R jets, and consequently can only be applied to the (non-RC) large-R jets. The ℓ + jets topology, on the other hand, is identified by requiring the presence of a semileptonically decaying top quark, which allows the top-quark jet to be identified without any top-quark-tagging requirement. The use of RC large-R jets in this channel is also motivated by several other factors: the mass resolution of the RC large-R jet, the resolution of the substructure variables, and the stability of the substructure measures in the presence of pile-up. In addition, the usage of RC large-R jets allows a single type of jet calibration (small-R jets) to be applied across the whole event. While the jet definitions are different in the two channels, the substructure variables measured in the same jet when it is reconstructed as either a large-R jet or a RC large-R jet are highly correlated, with correlation coefficients > 90%.

The DL1r multivariate algorithm [120] is used to identify small-R jets and variable-R jets that contain b-hadrons. This is a DNN algorithm exploiting information from the large-impact-parameter tracks, the topological decay chain, and the displaced vertices of b-hadron decays [121,122]. The jets are considered b-tagged if the value of the discriminant is larger than a threshold that provides 77% efficiency as measured in inclusive $t\bar{t}$ events. The corresponding rejection factors for gluon/light-quark jets and charm-quark jets are approximately 200 and 5, respectively. A lower efficiency of ∼70% is observed in the b-tagging of large-R top-quark jets in this analysis because of the

increased collimation and charged-track density in the boosted top-quark jets.

A large-R jet in the all-hadronic channel is labeled "b-matched" if a ghost-matching algorithm [123,124] matches it with one or more b-tagged variable-R jets. The ghost-matching procedure treats the objects to be matched as four-vectors of negligible magnitude in the standard jet reconstruction described above.

Top-quark tagging of large-R jets in the all-hadronic channel is performed with the DNN top-quark tagger noted above. The top-quark tagger's working point is set such that 80% of simulated top-quark jets are tagged, where the efficiency is determined using jets that fully contain the top-quark decay products. The tagger's efficiency in the simulated events is corrected to the observed efficiency in data by means of scale factors [12,125], evaluated in samples enriched in ℓ + jets $t\bar{t}$ decays.

Tracks are reconstructed in the inner detector using an iterative algorithm [126]. Reconstructed tracks are required to pass quality requirements based on the number of silicon-detector layers crossed and are required to have $p_{\mathrm{T}} > 500$ MeV and $|\eta| < 2.5$. Moreover, to reduce pile-up contamination, the tracks must be closely matched to the primary vertex: the transverse impact parameter calculated relative to the beam line must satisfy $|d_0| < 2$ mm and the longitudinal impact parameter z_0 calculated relative to the primary vertex must satisfy $|z_0 \sin(\theta)| < 3$ mm. The tracks are assigned to the small-R jets and large-R jets using the ghost-association technique and then used to calculate the substructure of the jet to which they are assigned. The use of tracks, as opposed to the energy flow measured with the calorimeter, provides greater precision for the substructure variables measured in the large-R jets and RC large-R jets.

The reconstruction of electron candidates combines information from the ID with calorimetry information [127,128]. Tracks from the ID are matched to energy deposits in the electromagnetic calorimeter (ECAL). These tracks must have trajectories consistent with originating from the primary vertex. The ECAL clusters must fall within the central acceptance, $|\eta| < 2.47$, and have $E_{\mathrm{T}} > 27$ GeV. Clusters must also be outside the transition region between the barrel and end cap sections of the ECAL, $1.37 < |\eta| < 1.52$. The electron candidates are required to have $p_{\mathrm{T}} > 27$ GeV and are identified using a likelihood-based method requiring that they satisfy the "TightLH" working point [127]. The charged track matched to the electron candidate must satisfy specific requirements on the impact parameters: the longitudinal impact parameter z_0 calculated relative to the primary vertex must satisty $|z_0 \sin(\theta)| < 0.5$ mm, and the significance of the transverse impact parameter calculated relative to the beam line must satisfy $|d_0/\sigma(d_0)| < 5$, where $\sigma(d_0)$ is the expected uncertainty in d_0. The "FCTight" criteria [127] must also be satisfied to ensure that the electron candidates are well isolated from nearby energy flow.

The reconstruction of muon candidates combines charged tracks in the ID with those found in the muon spectrometer [129]. The ID tracks must be consistent with coming from the primary vertex. Muon candidates must satisfy the "Medium" [129] identification criteria and the "FCTight" condition is imposed for muon isolation. In addition, the muons must have impact parameters satisfying $|d_0/\sigma(d_0)| < 3$ and $|z_0 \sin(\theta)| < 0.5$ mm. Muon candidates are required to have $p_{\mathrm{T}} > 27$ GeV and $|\eta| < 2.5$.

An overlap removal procedure is applied to reduce any double counting of objects that are independently reconstructed. An electron candidate is rejected if it shares a track with a muon candidate or if it has a track overlapping with another electron candidate. For small-R jets that are within $\Delta R(j, e) = 0.2$ of an electron candidate, the closest jet fulfilling this criterion is removed. If there are other small-R jets within $\Delta R(j, e) = 0.4$ of the electron candidate, the electron candidate is removed. Small-R jets that are within $\Delta R(j, \mu) = 0.2$ of a muon candidate or share a track with that muon candidate are removed if they comprise fewer than three tracks. Any muon candidate that is within $\Delta R(j, \mu) = 0.4$ of a small-R jet is removed.

Neutrinos are not measured by the detector so their presence is inferred from the missing transverse momentum, $E_{\mathrm{T}}^{\mathrm{miss}}$. This is the magnitude of the negative vector sum of the p_{T} of all selected and calibrated lepton candidates and small-R jets in an event, as well as a "soft" term [130] calculated from the p_{T} of ID tracks that are not associated with any of the lepton candidates or small-R jets.

B. ℓ + jets event selection

In the ℓ + jets channel, each event is required to have a primary vertex, to have passed a single-lepton trigger and to contain exactly one lepton candidate corresponding to the passed trigger. To reduce contributions from the multijet background and misidentified or nonprompt leptons, requirements are placed on $E_{\mathrm{T}}^{\mathrm{miss}}$ and the sum of the $E_{\mathrm{T}}^{\mathrm{miss}}$ and transverse mass[4] m_{T}^{W}. Each event is required to have $E_{\mathrm{T}}^{\mathrm{miss}} > 20$ GeV and $E_{\mathrm{T}}^{\mathrm{miss}} + m_{\mathrm{T}}^{W} > 60$ GeV. Small-R jets in these events must have $p_{\mathrm{T}} > 30$ GeV and $|\eta| < 2.5$. The leading[5] RC large-R jet must contain at least two small-R jets and is required to have $|\eta| < 2$ and $p_{\mathrm{T}} > 350$ GeV. In the 5% of selected events where there is more than one RC large-R jet satisfying these criteria, the

[4]The transverse mass is defined as $m_{\mathrm{T}}^{W} = \sqrt{2 p_{\mathrm{T}}^{\ell} E_{\mathrm{T}}^{\mathrm{miss}} [1 - \cos\Delta\phi(p_{\mathrm{T}}^{\ell}, E_{\mathrm{T}}^{\mathrm{miss}})]}$, where p_{T}^{ℓ} is the lepton p_{T}.

[5]If not differently specified, the term leading object always refers to the highest p_{T} object.

hadronic top-quark candidate is defined as the one with jet mass closest to the top-quark mass ($m_t = 172.5$ GeV). This choice maximizes the probability that the top-quark jet is identified correctly.

Events are required to contain at least one small-R jet that has been b-tagged. Requiring $\Delta R(\ell, b\text{-jet}) \leq 1.5$ ensures that one of these b-tagged jets will be close to the lepton candidate. The b-tagged small-R jet that is closest to the lepton candidate is chosen as the "leptonic" b-jet. This reflects the requirement that these objects should originate from the decay of the same top quark.

Additional requirements are imposed to further reduce backgrounds. The hadronic top-quark candidate is required to have a jet mass within 50 GeV of the top-quark mass to reduce background contributions from boosted W and Z bosons. To further ensure that the correct RC large-R jet is being chosen for measurement, the leptonic b-jet cannot be one of the constituents of the hadronic top-quark candidate. The lepton candidate is required to satisfy $\Delta R(\ell,$ hadronic top-quark candidate$) \geq 1.0$ to ensure that it is outside the selected RC large-R jet. Finally, the invariant mass $m(\ell, b)$ of the lepton candidate and the leptonic b-jet must satisfy $m(\ell, b) < 120$ GeV, reducing contributions from misidentified and nonprompt lepton candidates and from single-top-quark production.

C. All-hadronic event selection

The all-hadronic $t\bar{t}$ event selection is divided into two stages, with a preselection consisting of kinematic requirements on the jets, followed by a selection based on large-R-jet flavor tagging.

Events are required to have a primary vertex, satisfy the jet triggers described in Sec. III, and have two large-R jets with $p_{\mathrm{T}} > 350$ GeV and $|\eta| < 2.0$. The leading large-R jet is required to have $p_{\mathrm{T}} > 500$ GeV, and both jets are required to have a jet mass within 50 GeV of the top-quark mass. Events are rejected if they contain an electron or muon candidate with $p_{\mathrm{T}} > 25$ GeV in order to suppress contamination from events with top quarks decaying semileptonically. This lepton candidate veto also ensures that the two channels are orthogonal. This defines the preselection for the all-hadronic channel.

The preselected events are divided into 16 categories, called "regions" in the following, depending on whether the leading and second-leading large-R jets are top-quark-tagged and/or b-matched. These regions are used in the data-driven estimation of the multijet background described in Sec. V C. The regions used to measure the substructure are defined by requiring the leading and second-leading large-R jets to be b-matched and one of the large-R jets to be top-quark-tagged.

Only large-R jets with p_{T} above 500 GeV are used to measure the jet substructure.

V. BACKGROUND ESTIMATION

The backgrounds in the two channels are estimated using a combination of MC-based techniques and data-driven measurements.

A. MC-estimated backgrounds

All the backgrounds in the ℓ + jets channel, except those from nonprompt and misidentified leptons, are estimated using the MC simulations described in Sec. III. Single-top-quark production represents the largest background, with tW production being the dominant process. The W + jets process represents the second-largest background, at the same level as the background from events containing nonprompt or misidentified lepton candidates. Backgrounds from other sources, including the Z + jets, $VV(V = Z/W)$, and $t\bar{t}V(V = Z/W/H)$ processes, are negligible.

The largest MC-estimated background in the all-hadronic channel comes from $t\bar{t}$ production where one of the top quarks decays semileptonically and the charged lepton arising from this decay is not identified. The next largest background arises from single-top-quark production in the tW-channel and t-channel. The $t\bar{t}V(V = Z/W/H)$ processes produce the smallest backgrounds.

These MC-estimated backgrounds comprise ∼6% and ∼9% of the ℓ+jets and all-hadronic samples, respectively.

B. Misidentified- and nonprompt-lepton backgrounds in the ℓ + jets channel

Some background events in the ℓ + jets channel contain an isolated-lepton candidate that does not originate from a W-boson decay. This type of background includes lepton candidates arising from misidentified jets and leptons coming from the weak decay of a hadron—nonprompt (NP) leptons. These background processes are estimated with a data-driven technique known as the matrix method [131], used in recent differential measurements in the ℓ + jets channel [2].

The matrix method is based on "tight" and "loose" selections for the lepton candidates. The tight selection is the nominal one described in Sec. IV, while the loose selection has no isolation requirement and less stringent lepton identification requirements. Loose electron candidates are reconstructed at the "MediumLH" [127] working point, while the "Medium" [129] working point is used for muon candidates. The resulting misidentified- and nonprompt-lepton (NP/Misid.) background comprises 2% of the sample.

C. Multijet-background estimation in the all-hadronic channel

The dominant background in the all-hadronic channel arises from multijet production and is estimated using a data-driven technique. The present measurement uses the "ABCD" estimate, which was first developed [132] to

2nd large-R jet \ 1st large-R jet	t0b0	t1b0	t0b1	t1b1
t1b1	J	K	L	S
t0b1	B	D	H	N
t1b0	E	F	G	M
t0b0	A	C	I	O

FIG. 1. Events passing the preselection requirements are divided into 16 regions according to the b-matching and top-quark-tagging status of the leading and second-leading large-R jets, here labeled simply 1st and 2nd large-R jet, respectively. Labels t1 and t0 indicate whether the large-R jet has passed or failed the top-quark tagger, respectively. Labels b1 and b0 indicate whether the large-R jet has or has not been b-matched, respectively. Regions L, S, and N constitute the regions used to measure the jet substructure, while K and M are the validation regions.

measure the $t\bar{t}$ differential cross section using an all-hadronic event selection. This approach is adapted here to estimate the multijet background in bins of large-R-jet substructure observables.

The technique uses the correlations between the mistagging rates of b-tagging and top-quark-tagging algorithms for one large-R jet to determine the multijet background. As described in Sec. IV C, events passing the preselection are divided into categories depending on whether the leading and second-leading large-R jets are top-quark-tagged and/or b-matched, creating 16 regions with different multijet background contributions, shown in Fig. 1. Among these regions, the ones where both leading large-R jets are b-matched and at least one is top-tagged represent the signal regions. The two regions defined by requiring both large-R jets to be top-tagged but only one to be b-matched are not directly used in the ABCD estimate, but employed as validation regions. The remaining 11 regions are considered as control regions.

The estimated contributions from $t\bar{t}$ signal events and other MC-predicted backgrounds are subtracted from the total event yields in the control regions, and the remaining event yields are used as input to calculate a bin-by-bin estimate of the multijet background in the signal and validation regions, using the ABCD method, described in detail in Ref. [15]. The validation regions, labeled K and M in Fig. 1, are employed to validate the modeling of the multijet background with the substructure variables.

D. Comparisons of data with predictions

The event yields for data, predicted $t\bar{t}$ signal, and all backgrounds after applying the selection described in Sec. IV are shown for both channels in Table I. Since the $Z+$jets and $VV(V=Z/W)$ backgrounds are small in the $\ell+$jets channel, they are combined into the "Other" category in the table and following plots. The event selection is able to separate the signal from the various background sources in both channels, with the signal purity reaching 92% and 65% in the $\ell+$jets and all-hadronic channels, respectively.

TABLE I. Detector-level event yields for data, simulated $t\bar{t}$ signal, and background processes. All uncertainties affecting the detector and background modeling are included. Due to the tag-and-probe method employed by the all-hadronic channel, the numbers here refer to the number of measured large-R jets, rather than events present. The signal purity is defined by the number of data events minus background events divided by the total sample size.

Category	Event yields $\ell+$jets selection	Number of large-R jets all-hadronic selection
Data	**83 069**	**30 524**
Predictions	**97 200±3 700**	**36 500±1 400**
$t\bar{t}$ ($\ell+$jets)	90 600 ± 3 400	1 610 ± 140
$t\bar{t}$ (all-hadronic)	···	25 700 ± 1 400
Multijet	···	8 100 ± 300
Single-top quark	2 200 ± 300	710 ± 70
NP/Misid. leptons	1 500 ± 600	
$W+$jets	1 500 ± 700	···
$t\bar{t}V$ ($t\bar{t}Z+t\bar{t}W+t\bar{t}H$)	920 ± 120	310 ± 40
Other	400 ± 200	···
Data/Predictions	0.85 ± 0.03	0.84 ± 0.03
(Data—Bkg)/Signal	0.84 ± 0.03	0.77 ± 0.05
Signal purity	0.92 ± 0.01	0.65 ± 0.01

The predicted yields overestimate the data yields in the $\ell+$jets and all-hadronic channels by 16% and 20%, respectively. This is consistent with observed yields in the boosted $t\bar{t}$ regime in other measurements [132–136], and is believed to come from missing higher orders in the NLOME + PS differential cross-section calculation, which mostly affect the high-p_{T} regions. A correction for this overestimate is made by defining a normalization scaling evaluated as (Data–Background)/Signal and shown in Table I. This scaling is used to compare the shapes of the observed distributions with those predicted by the MC calculations and estimated backgrounds.

Comparisons of the observed kinematic distributions with the ones predicted by the nominal signal MC sample and background estimates in the $\ell+$jets channel are shown in Fig. 2. The figure shows the distributions of the number of RC large-R jets in the event, the p_{T} of the RC large-R jet, and $m(\ell, b)$. Comparisons between the observed and predicted kinematic distributions of the leading and second-leading large-R jets in the all-hadronic

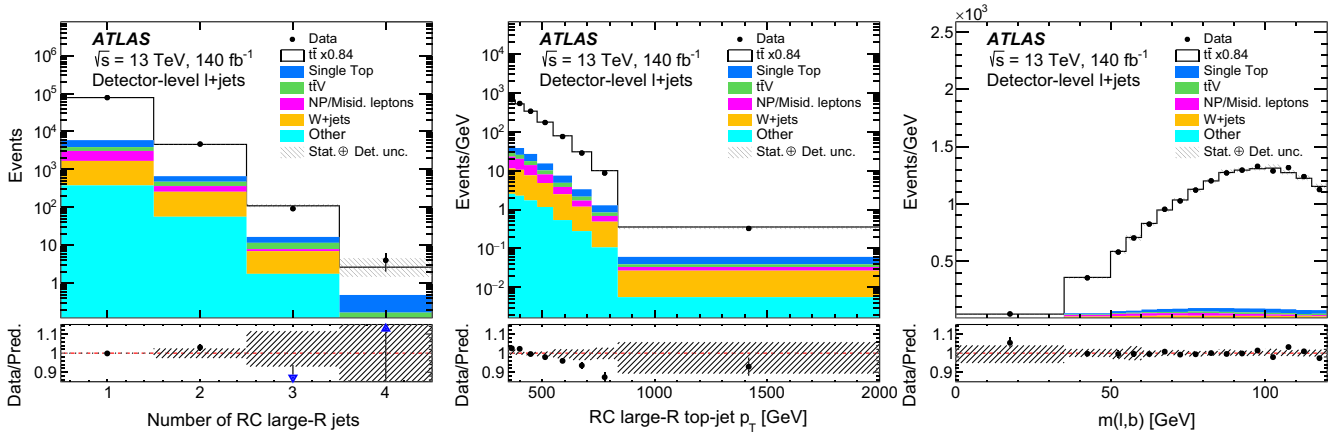

(a) (b) (c)

FIG. 2. Detector-level distributions in the ℓ + jets channel for (a) the number of RC large-R jets, (b) the p_{T} of the hadronic-top-quark candidate RC large-R jet, and (c) $m(\ell, b)$. The lower graph shows the ratios of the data to the predictions; triangles in (d) indicate ratio values outside the shown range. The hatched band represents the sum of the detector-related uncertainties in the predictions. The statistical uncertainties are shown for the data points. Larger values of the observables for the left and middle plots, beyond the histogram range, are included in the last bin. The predicted $t\bar{t}$ yield is adjusted so that the total predicted yield equals the observed number of data events. The bin contents are divided by the bin widths.

channel are shown in Fig. 3. The shapes of most of the compared distributions are in good agreement, validating the modeling of the kinematics of the jets in $t\bar{t}$ events and the estimated backgrounds. The only discrepancy appears in the comparison of the p_{T} distributions of the top-quark candidate jets, where the predicted distributions have a flatter p_{T} dependence consistent with the increasing overestimate of the $t\bar{t}$ cross section as a function of top-quark p_{T} as noted above.

VI. MEASURED SUBSTRUCTURE OBSERVABLES

The observed substructure variables are calculated using the charged tracks associated with the hadronic top-quark candidate. In the all-hadronic analysis the charged tracks are ghost-associated with the large-R jet. In this case, the trimming procedure, described in Section IV A, is applied concurrently to the ghost-tracks. In the ℓ + jets channel,

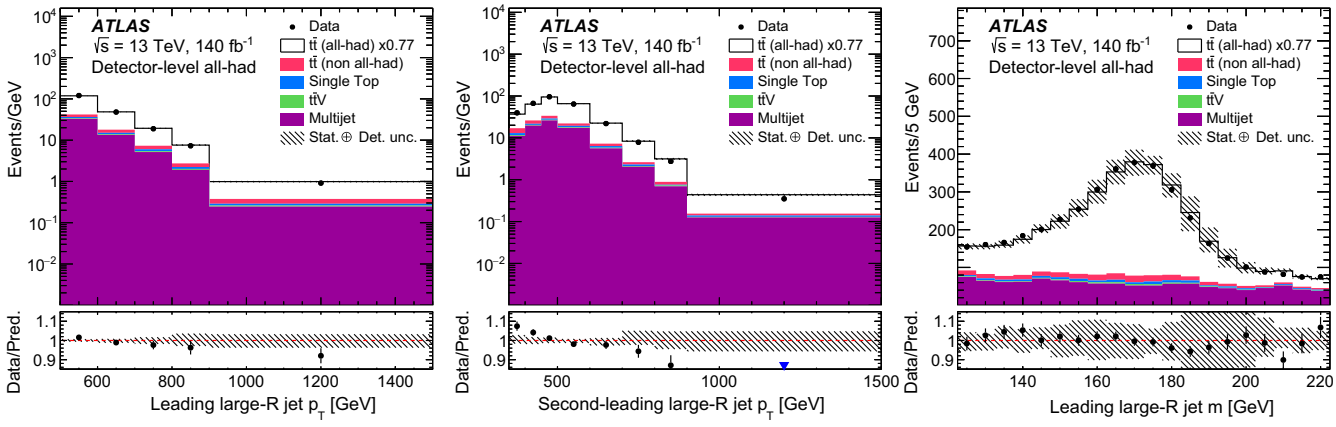

(a) (b) (c)

FIG. 3. Detector-level distributions in the all-hadronic channel for (a) the p_{T} of the leading large-R jet, (b) the p_{T} of the second-leading large-R jet, and (c) the mass of the leading large-R jet. The lower graph shows the ratios of the data to the predictions; the triangle in (d) indicates a ratio value below the shown range. The hatched band represents the sum of the detector-related uncertainties in the predictions. The statistical uncertainties are shown for the data points. Larger values of the observables for the left and middle plots, beyond the histogram range, are included in the last bin. The predicted $t\bar{t}$ event yield is adjusted so that the total predicted yield equals the observed number of data events. The bin contents are divided by the bin widths.

tracks are ghost-associated with the small-R jets that constitute the reclustered large-R jet.

Several classes of observables are measured:

(i) Generalized angularities [51]:

$$\lambda_\beta^\kappa = \sum_{i \in J} z_i^\kappa \left(\frac{\Delta R(i, \hat{n})}{R} \right)^\beta.$$

Given a jet J, z_i is the fraction of the jet's p_{T} carried by the ith constituent, $\hat{n}$ is the jet axis, and R is the jet radius. The variables κ and β are parameters chosen to weight the p_{T} and angular terms, respectively. In this analysis, only λ_0^2 and $\lambda_{0.5}^1$ are measured and are referred to as the jet p_{T} dispersion ($p_{\mathrm{T}}^{\mathrm{d}}$) and the Les Houches angularity (LHA), respectively. The jet p_{T} dispersion is highly correlated with the particle multiplicity (N) and thus a scaled p_{T} dispersion variable is used to mitigate this correlation:

$$p_{\mathrm{T}}^{\mathrm{d},*} = \sqrt{\left(p_{\mathrm{T}}^{\mathrm{d}} - \frac{1}{N} \right) \frac{N}{N-1}}.$$

(ii) Energy correlation functions (ECFs) [49,137]: the general formula for these functions in a jet produced by a hadron collider is

$$\mathrm{ECF}(N) = \sum_{i_1 < i_2 < \ldots < i_N \in J} \left(\prod_{a=1}^{N} p_{\mathrm{T},i_a} \right) \times \left(\prod_{b=1}^{N-1} \prod_{c=b+1}^{N} \Delta R(i_b, i_c) \right).$$

Here the sum runs over all constituents of the jet, ordered by index i so that no pairwise calculations are repeated, and N represents the number of prongs. Ratios of the ECFs can be used to probe N-pronged substructure. Here C_3 and D_2 are measured:

$$C_3 = \frac{\mathrm{ECF}(4)\,\mathrm{ECF}(2)}{\mathrm{ECF}(3)^2},$$

$$D_2 = \frac{\mathrm{ECF}(3)\,\mathrm{ECF}(1)^3}{\mathrm{ECF}(2)^3}.$$

A jet with a pronounced three-body (two-body) structure will have C_3 (D_2) close to 0. The normalized energy correlation function $ECF2$ is also measured. The normalized version is used to reduce the dependence on the jet-constituent multiplicity:

$$\mathrm{ECF2} = \frac{\mathrm{ECF}(2)}{\mathrm{ECF}(1)^2}.$$

(iii) N-subjettiness [47]: a jet's N-subjettiness provides a measure of the degree to which that jet is compatible with comprising N or fewer subjets. It is defined as:

$$\tau_N = \frac{1}{d_0} \sum_k p_{\mathrm{T},k} \min\{\Delta R_{1,k}, \Delta R_{2,k}, \ldots, \Delta R_{N,k}\}, \quad \text{with} \quad d_0 = \sum_k p_{\mathrm{T},k} R_0.$$

The constituents of the jet are reclustered using the exclusive k_t algorithm [138], with the winner-takes-all (WTA) recombination scheme. The clustering continues until N subjets are returned. The calculation of τ_N then runs over the constituents of the jet, with $p_{\mathrm{T},k}$ the p_{T} of the kth constituent. The variable R_0 is the jet radius parameter. The ratios $\tau_{21} \equiv \tau_2/\tau_1$ and $\tau_{32} \equiv \tau_3/\tau_2$ are measured, along with τ_3. A jet with a pronounced three-body (two-body) structure will have τ_3 (τ_2) close to 0. The ratios are used to discriminate between jets with different N-prong structures, e.g., a jet better described by a 3-prong structure than by a 2-prong one will have a τ_{32} value closer to 0 than to 1.

This set of eight substructure variables includes observables sensitive to the modeling of three-prong (τ_{32}, C_3) or two-prong (D_2, τ_{21}) objects, to the distribution of the momentum of the constituents inside the jet ($p_{\mathrm{T}}^{\mathrm{d},*}$) and to the broadness of the jet (LHA). Two of these variables (D_2, τ_{32}) are the most sensitive in the multivariable discriminator developed by the ATLAS Collaboration [12] to identify W-boson- and top-quark-initiated jets. Given the importance of D_2 and τ_{32} for particle tagging, these observables are also measured as a function of the particle-level top-quark-jet mass (m^{top}) and p_{T} ($p_{\mathrm{T}}^{\mathrm{top}}$). The $ECF2$ and τ_3 observables are also measured, since they are relevant in the calculation of D_2, C_3, and τ_{32}. The substructure variable τ_3 is selected also because it appears to be poorly described by MC predictions. These variables are not highly correlated and show sensitivity to showering, hadronization, and final-state radiation.

In the all-hadronic channel, the substructure measurement takes advantage of the presence of two large-R jets. It follows a tag-and-probe approach that involves first measuring the substructure distribution of the leading large-R jet by requiring that the second-leading large-R jet is top-quark tagged. In this configuration, the leading large-R jet is the "probe" jet and the second-leading jet is the "tag" jet. The substructure distribution of the second-leading jet is then measured in those events where it satisfies the same kinematic requirements as the leading jet, namely $p_{\mathrm{T}} > 500$ GeV, and where the leading jet is top-quark tagged. This avoids biasing the substructure of the probe jet through the substructure-dependent DNN top-quark-tagging algorithm. This technique requires that there is no

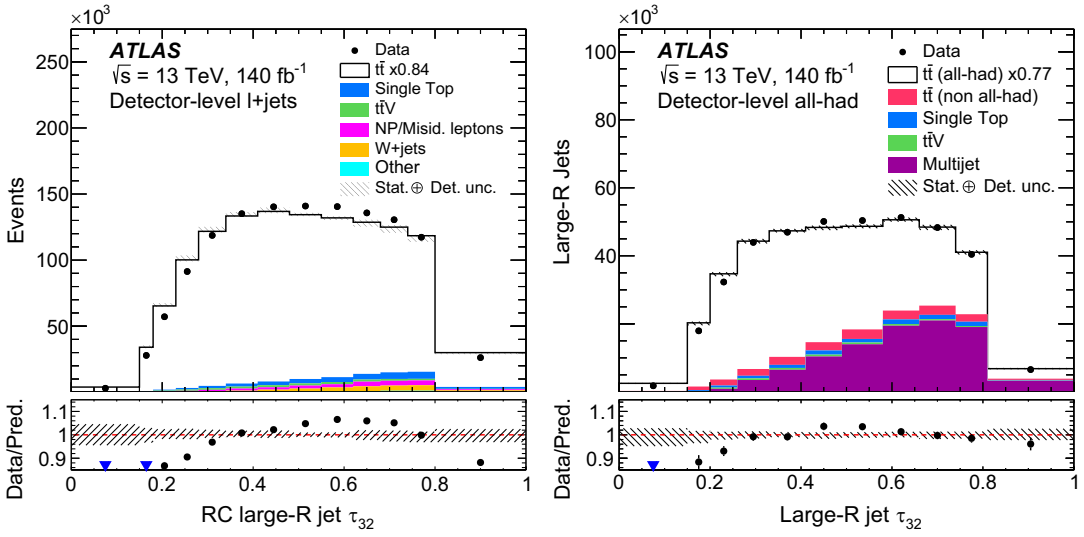

(a) (b)

FIG. 4. Detector-level τ_{32} distributions in the (a) $\ell+$jets and (b) all-hadronic channel for data, predicted $t\bar{t}$ signal, and measured backgrounds. The predicted $t\bar{t}$ signal is normalized so that the total predicted yield agrees with the observed number of events. The lower pad shows the ratios of the data to the predictions; triangles indicate ratio values below the shown range. The hatched band represents all the detector-related uncertainties of the predictions. The modeling uncertainties of the signal are not included in the band. The data points are presented with their statistical uncertainty.

event-to-event correlation in the substructure measurement in the leading and second-leading jets, which is confirmed by MC studies.

The distributions of the substructure variables for the leading and second-leading large-R jets are added together to produce a combined measurement. The combined distribution is then unfolded using the technique described in Sec. VII. This combined measurement increases the number of jets by ∼50%.

The observed shapes of the distributions of the substructure observables are compared with the nominal $t\bar{t}$ model predictions and background estimates for both the $\ell+$jets and all-hadronic channels. While the observed and predicted shapes are generally in good agreement, the distributions of some observables, such as $p_{\mathrm{T}}^{\mathrm{d},*}$ or τ_{32}, are poorly described by the predictions. The latter observable, τ_{32}, is shown in Fig. 4, where only the statistical uncertainty and detector-level systematic uncertainties are included.

VII. CROSS-SECTION MEASUREMENT

The observed distributions are affected by the detector and selection acceptance, resolution, and efficiency. An unfolding technique is used to correct for these effects. It unfolds the observed distributions to particle level in a suitably chosen kinematic region called the fiducial phase-space.

A. Particle-level fiducial phase-space

The particle-level objects are defined using the stable particles (those with $c\tau > 10$ mm where τ is the proper lifetime of the particle) in the MC calculations. The selection requirements imposed on these objects define the particle-level fiducial phase-space, and are similar to the detector-level requirements so that large extrapolations of the measured quantities are avoided.

Electrons and muons from the electroweak decays of top quarks are selected by rejecting those that come from the decay of hadrons, directly or through τ-lepton decays. Leptons arising from τ-lepton decays that are not the result of prompt hadron decays are also accepted. Leptons are then "dressed" by summing their four-momenta with any prompt photons within $\Delta R = 0.1$. The dressed leptons are required to have $p_{\mathrm{T}} > 27$ GeV and $|\eta| < 2.5$. Dressed muons and electrons separated by $\Delta R < 0.4$ from a jet are excluded. Neutrinos are required to come from a top-quark electroweak decay, and the $E_{\mathrm{T}}^{\mathrm{miss}}$ is calculated from the four-momenta sum of the selected neutrinos.

Particle-level small-R and large-R jets are built by clustering all stable particles, except for the selected dressed leptons, neutrinos not coming from hadron decays, and photons not used in the dressing. The decay products of hadronically decaying τ-leptons are included. The RC large-R jets are built by the anti-k_t jet-clustering algorithm with a radius parameter of $R = 1.0$, using the particle-level small-R jets as input. The same trimming algorithms as described earlier for large-R jets and RC large-R jets are employed for the particle-level objects.

Particle-level b-tagging is performed by ghost-matching b-hadrons to jets. A particle-level small-R or large-R jet with at least one ghost-matched b-hadron with $p_{\mathrm{T}} > 5$ GeV is defined as being b-tagged. No specific top-quark

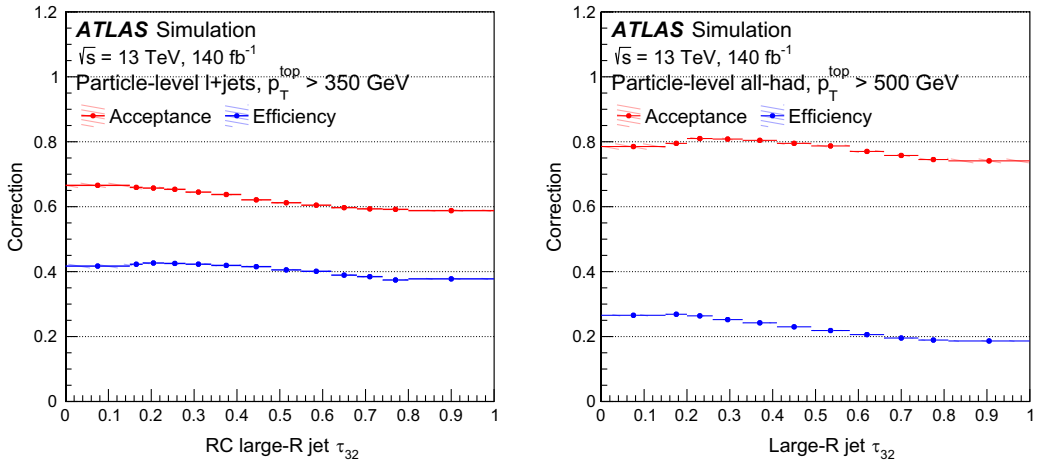

FIG. 5. Acceptance and efficiency corrections for the τ_{32} variable in the (a) ℓ + jets and (b) all-hadronic channels.

tagging is performed on particle-level large-R jets beyond the requirement on the large-R jet mass, and particle-level large-R jets are not required to be matched to parton-level top quarks.

The event selection for both channels closely follows the detector-level selection described in Sections IV B and IV C, with the only difference being in the selection of the jets used to reconstruct the variables in the all-hadronic channel, where the tag-and-probe method is not applied at particle level. Top-quark candidates in the event are required to be b-tagged, and the ones with $p_{\mathrm{T}} > 500$ GeV are employed to reconstruct the jet substructure. The reconstruction of the jet substructure at particle level closely follows the definition employed at detector level. In the all-hadronic case, only the charged components of the large-R jets are considered as input when reconstructing the observables. In the ℓ + jets case, the substructure observables are built by using the charged constituents of the small-R jets as components of the RC large-R jets. In both channels, only charged particles with p_{T} above 500 MeV and $|\eta| < 2.5$ are considered.

B. Iterative Bayesian-unfolding method

The iterative Bayesian-unfolding algorithm [139], as implemented in RooUnfold [140] is employed to unfold the observed data distributions to the particle-level distributions. The differential cross section (both single and double) in bin j of a particle-level distribution is represented heuristically as

$$\frac{\mathrm{d}\sigma_j}{\mathrm{d}X_j} = \frac{1}{\int \mathcal{L}\mathrm{d}t \cdot \Delta X_j} \frac{1}{f_j^{\mathrm{eff}}} \sum_i M_{ij}^{-1} f_{\mathrm{acc}}^i (D^i - B^i), \quad (1)$$

where i runs over the detector-level bins, X represents one or a pair of variables, $\int \mathcal{L}\mathrm{d}t$ is the integrated luminosity of the sample, and ΔX_j represents the width of bin j. The variable D_i represents the data histogram obtained after the event selection, and B_i represents the distributions of the estimated backgrounds. By concatenating the bins of a given substructure observable for each region of $p_{\mathrm{T}}^{\mathrm{top}}$ or m^{top}, a one-dimensional distribution can be constructed in order to apply this formula to the double-differential distributions [133]. The functions f^{eff} and f_{acc} are unfolding corrections, derived using the nominal POWHEG+PYTHIA8 prediction for $t\bar{t}$ production and decay. The efficiency correction f^{eff} accounts for events passing the particle-level phase-space requirements but not the detector-level requirements. The acceptance correction f_{acc} accounts for events that pass the detector-level selection but fail the particle-level fiducial phase-space requirements.

Examples of the f_{acc} and f^{eff} corrections in the ℓ+jets and all-hadronic channels are illustrated in Fig. 5. The efficiency is driven by the use of algorithms which are not fully efficient, such as b- and top-tagging. The acceptance is driven by the resolution on the quantities used for the selection requirements. As a consequence, the unfolding corrections differ between the two channels due to the differences in the selection: the cuts on $E_{\mathrm{T}}^{\mathrm{miss}}$ and $m(\ell, b)$ decrease the acceptance in the ℓ + jets channel, while the requirements on the number of b-tagged jets and the top-tagging lowers the efficiency in the all-hadronic channel.

The migration matrix M quantifies the smearing that arises from detector-resolution effects. It is evaluated by using MC events that pass both the detector-level and particle-level fiducial phase-space selections and binning them into the matrix, where the rows and columns represent the particle-level and detector-level bins, respectively. Each row is normalized to sum to unity. In Eq. (1), M^{-1} represents the effects of the iterative Bayesian-unfolding procedure that is employed to unfold the detector-level distributions. The amount of regularization introduced by

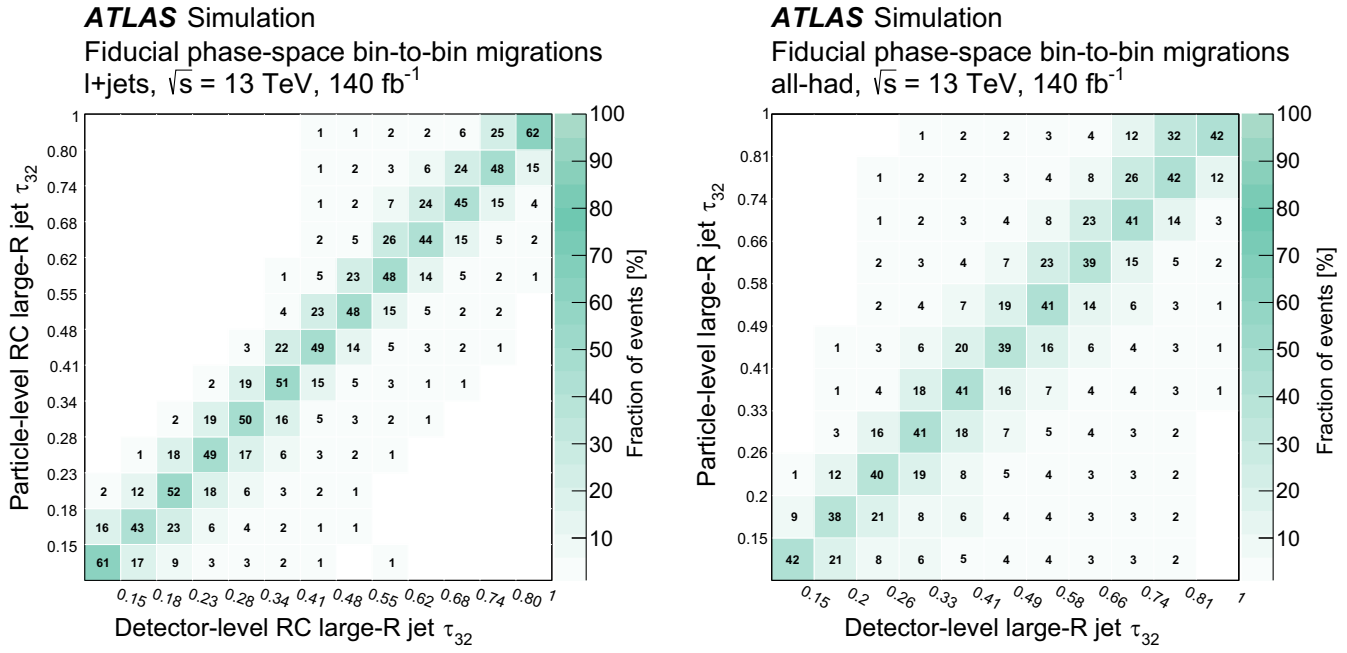

FIG. 6. Migration matrices for the variable τ_{32} in the (a) ℓ + jets channel and (b) all-hadronic channel.

this unfolding method is determined by the number of iterations. A large number of iterations corresponds to fully unregularized matrix-inversion. The number of iterations employed in this analysis for all distributions is six, chosen as a compromise between the bias and the statistical fluctuations. The absence of a non-negligible bias is verified with the methods described in Sec. VII C.

The bin widths chosen for the substructure distributions optimize the robustness of the unfolding procedure while retaining as many bins as possible to resolve detailed features in the unfolded distributions. The first criterion is addressed by employing bin widths that result in unfolding matrices that are largely diagonal by requiring that at least 40% of the jets fall in the diagonal bins.

The migration matrices for the observable τ_{32} in the ℓ + jets and all-hadronic channels are shown in Fig. 6, and are similar to the other migration matrices.

C. Unfolding validation

Tests are performed to ensure the unfolded distributions have the correct statistical properties, reproduce input distributions that differ from the nominal ones used to produce the corrections and unfolding matrices, and are stable within the expected statistical uncertainty. In order to check for stability amid statistical fluctuations, each bin of the nominal MC distributions is smeared according to a Poisson distribution, with mean equal to the bin content, to create pseudoexperiments. The distributions of the unfolded variables in the pseudoexperiments are then compared with the particle-level input distributions to verify that the unfolding procedure is unbiased and the statistical uncertainty of the unfolded distributions matches the precision as observed in the ensemble of pseudoexperiments.

Additional tests are performed to verify the absence of bias originating from the choice of MC model used to derive the corrections in Eq. (1). Nine pseudoexperiments are created for each observable by reweighting the nominal MC distributions, at detector level and particle level, with nine different weighting functions. Each function is based on a polynomial fit to the ratio of the data to the nominal MC prediction of the measured observables. An additional pseudoexperiment is based on the disagreement between the data and the nominal prediction on the top-quark jet p_{T}, in this case a linear fit is employed and the slope of the fit is doubled to derive the weight function used for the test. The fit is performed separately in the two channels and in the all-hadronic channel separately for the leading and subleading jet. The pseudoexperiments are then unfolded using the nominal set of corrections. The reweighted unfolded distributions are compared with the weighted distributions at particle level. The procedure correctly reproduces most of the weighted distributions, verifying the robustness of the unfolding procedure. The only exception is the reweighting as a function of top-quark p_{T}, where a relatively small degree of nonclosure is observed. This nonclosure, due to the top-quark p_{T} shape, is included as an additional source of uncertainty and described in Sec. VIII D.

VIII. SYSTEMATIC UNCERTAINTIES

The systematic uncertainties in the unfolded distributions are separated into uncertainties arising from the

reconstruction and calibration of the jet and lepton candidates, the background estimates, and the modeling of the $t\bar{t}$ final state.

Uncertainties related to modeling of the detector and background are propagated to the unfolded distributions by creating pseudoexperiments from simulated signal and background events in which a single source of uncertainty is varied by one standard deviation. The resulting distributions are then treated as if they were data and unfolded using the nominal unfolding corrections, as described in Section VII B.

The signal-modeling uncertainties affect the measured cross section through the unfolding corrections. To estimate these uncertainties, the alternative $t\bar{t}$ simulations at detector level are used to create pseudodata, which are then unfolded using the nominal unfolding correction (efficiency, acceptance, migration matrix, and background subtraction). The nonclosure between the unfolded pseudodata and the alternative particle-level prediction is taken as an uncertainty in the measured cross section.

A. Detector uncertainties

Lepton reconstruction and identification uncertainties are estimated by comparing the identification performance in data and MC samples and adjusting the performance in the MC samples to match that in data. The uncertainties from these comparisons are used as the systematic uncertainties associated with the lepton reconstruction in both channels. Uncertainties in the lepton-momentum scale and resolution are determined by comparing the performance measured in data and in MC samples [128,129].

The jet energy scale (JES) uncertainties for small-R and large-R jets are determined from test beam data, simulation, and *in situ* measurements of the p_{T} balance between jets and recoiling objects in $Z+$ jet, $\gamma+$ jet, and multijet events [117,118]. The jet energy resolution (JER) uncertainty is measured in dijet events as the width of the best-fit p_{T}-asymmetry distribution. The JES and JER uncertainties associated with the RC large-R jets are derived from the uncertainties in the constituent small-R jets.

Uncertainties in the $E_{\mathrm{T}}^{\mathrm{miss}}$ modify both the magnitude and direction of its vector. They are determined from the uncertainties in the momentum calibration and resolution of the leptons and jets used to calculate this observable, as well as an uncertainty in the soft term [130].

The jet mass scale (JMS) uncertainty for large-R jets is estimated by fitting the top-quark-jet and W-jet mass peaks in $\ell+$ jets $t\bar{t}$ events and by measuring the relative response for calorimeter-based jets and track-jets in data and MC samples of dijet events [118,141]. The jet mass resolution (JMR) uncertainty for large-R jets is derived from the same fits of the top-quark-jet and W-jet mass peaks [141]. The JMR is conservatively set to 20% outside the phase space covered by these measurements.

The uncertainty in the efficiency of the JVT algorithm is determined from studies of its performance in data samples and MC events [116].

The b-tagging performance is measured in data events and MC samples, and any difference is used to correct the MC b-tagging efficiency. The uncertainty in this calibration is used as the systematic uncertainty in the b-tagging efficiency [121,122]. An efficiency uncertainty for jets with $p_{\mathrm{T}} > 300$ GeV is estimated by extrapolating the efficiency measured at lower p_{T} to these higher-p_{T} jets [142].

The efficiency and mis-tagging rate of the DNN top-quark tagger, and their uncertainties, are derived using hadronically decaying top quarks in boosted $t\bar{t}$ events, $\gamma+$ jet events, and dijet events [12]. The uncertainty includes effects arising from JES and modeling uncertainties that affect the substructure of the top-quark jets.

Several sources of systematic uncertainty are considered for the tracks used in the substructure measurements [143]. The uncertainty in the fake rate is derived from template fits to data and simulated events performed in a control region enriched in fake tracks. An additional uncertainty is used to account for differences in the impact parameter resolution between simulated and real data events. This uncertainty is estimated in bins of jet η and p_{T} and applied to simulated events in the form of a random smearing of the transverse and longitudinal track impact parameters. Uncertainties in efficiencies and alignment of the tracking detectors are also considered. In addition, uncertainties in the reconstruction of tracks associated with high-p_{T} jets are also included [126]. The track uncertainties are propagated to the track requirements employed to select the tracks used to identify the primary vertex and measure the jet substructure.

B. ℓ + jets-channel background modeling

Several sources of uncertainty affect the single-top-quark background, the largest background process in the $\ell+$ jets channel. The uncertainty associated with the initial-state-radiation (ISR) model is determined by modifying the nominal POWHEG+PYTHIA8 calculation by varying μ_{r} and μ_{f} independently by factors of 0.5 and 2.0 in the matrix-element calculation, and by varying the scales in the showering model according to the Var3c eigentune of the A14 tune. The final-state-radiation (FSR) uncertainty is determined using a separate POWHEG+PYTHIA8 sample where the renormalization scale is varied from its nominal value by factors of 0.5 and 2. The uncertainties due to the PYTHIA scale variations are correlated with the corresponding $t\bar{t}$ variations. The uncertainty arising from the scheme used to remove interference between the $t\bar{t}$ and tW processes is determined by taking the difference between the DR and DS approaches. The uncertainty due to the choice of showering and hadronization scheme is determined by comparing the nominal prediction with an alternative model using the HERWIG generator. The

uncertainty in the NNLO cross section for the single-top-quark processes arising from the choice of PDF set and α_s is 4.2% for the t-channel process, 5.4% for the tW process, and 3.9% for the s-channel process [144,145].

The uncertainties in the $W+$jets background estimates are evaluated using two alternative MC samples where μ_r and μ_f in the matrix-element and showering models are varied simultaneously by factors of 0.5 and 2.0 [146]. The uncertainty in the cross-section calculation for the associated-production processes $t\bar{t}Z$, $t\bar{t}W$, and $t\bar{t}H$ are 13.3%, 12%, and 9.9%, respectively [147]. The uncertainty in the sum of these backgrounds is set to 13.3%, which is the largest of the three individual uncertainties.

The uncertainty in the cross sections for the $Z+$jets and diboson processes is conservatively estimated to be 50% [146]. However, these backgrounds contribute $< 1\%$ and thus are negligible.

The uncertainty in the misidentified-lepton background is assessed by comparing the estimates from the matrix-element method, described in Sec. V B, with an alternative method. In this method, the shape of the distributions of the misidentified-lepton events is derived from a MC estimate, obtained using all-hadronic $t\bar{t}$ and $V+$jets samples, while the normalization is obtained through a fit of the observed E_T^{miss} and $E_T^{miss}+m_T^W$ distributions. The uncertainty in the misidentified-lepton estimate is below 1%, except in some poorly populated regions, where it can reach 5%.

C. All-hadronic-channel background modeling

The main uncertainty in the multijet background estimate is due to the data statistical uncertainty in the control regions introduced in Sec. V C and used in the ABCD method. All the detector- and signal-modeling uncertainties are propagated through the multijet estimation, in the subtraction of the estimated signal and MC backgrounds from the control regions. The largest uncertainty in the multijet background arises from the uncertainty in the top-quark mis-tagging rate in the MC-subtracted backgrounds.

The uncertainties associated with the non-all-hadronic background, the single-top-quark background, and the background due to the associated-production processes $t\bar{t}W$, $t\bar{t}Z$, and $t\bar{t}H$ arise from their cross-section uncertainties and are incorporated into the overall uncertainty in these background estimates.

D. Signal modeling

The uncertainties arising from the modeling of the $t\bar{t}$ production and decay processes are evaluated by using alternative MC samples to create pseudoexperiments and unfolding them with the nominal unfolding matrices. The differences between the unfolded results and the predictions of the alternative MC samples are taken as the modeling uncertainty.

The uncertainties in the modeling of ISR in the $t\bar{t}$ process are estimated using the samples where the scales μ_r and μ_f in the matrix element are varied independently by factors of 0.5 and 2.0 in the POWHEG calculations, and two samples employing the Var3cUp/Down eigentune of the A14 tune of PYTHIA 8. The FSR uncertainty is estimated using the samples where the renormalization scale regulating FSR is changed by factors of 0.5 and 2.0, corresponding to $\alpha_s^{FSR}(m_Z)=0.142$ (FSR Down) and $\alpha_s^{FSR}(m_Z)=0.114$ (FSR Up), respectively. The uncertainty associated with the choice of h_{damp} parameter value is estimated using a sample with h_{damp} a factor of 2 larger than the nominal value. The resulting changes in the unfolded results are symmetrized as an up-and-down systematic uncertainty. All uncertainties pertaining to radiative corrections are combined into *IFSR*.

The *Parton Shower* uncertainty arises from the choice of parton-shower, hadronization, underlying-event, and color-reconnection models. It is estimated by employing the HERWIG 7 parton-showering and hadronization model instead of the nominal PYTHIA 8 model, with the resulting uncertainty being symmetrized. The *Hard Scattering* uncertainty arises from the matching method, and is estimated by comparing the results of a POWHEG +PYTHIA8 MC sample with the one created using the AMC@NLO+PYTHIA MC generator. This uncertainty takes into account a different choice of parton-matching scheme and renormalization scheme [148]. To exclude the differences arising from the matrix-element corrections applied to all emissions in the nominal POWHEG+PYTHIA8 sample, a dedicated POWHEG+PYTHIA8 simulation with these corrections turned off is used for this comparison. The uncertainty arising from the choice of PDF is estimated using the 30 eigenvectors decomposed from the Hessian representation of the PDF4LHC30 PDF uncertainties [88].

An additional source of uncertainty is the effect of the top-quark mass uncertainty on the measured distributions. The uncertainty considered for the top-quark mass is 0.5 GeV, reflecting the precision of the top-quark mass measurements reached by the ATLAS [149] and CMS [150] collaborations. The resulting uncertainty is evaluated by creating pseudoexperiments with an alternative top-quark mass and propagating it through the analysis. This uncertainty is negligible in all the measured differential cross sections.

Finally, a modeling uncertainty arises from the observed difference between the observed and predicted shapes of the top-quark p_T distribution. This difference, between the data and the nominal POWHEG+PYTHIA8 prediction, is used to define a reweighting function, which is then applied to the nominal prediction to obtain an alternative sample. Pseudoexperiments created from this alternative sample are then propagated through the unfolding procedure, and the difference between these results and those from the nominal procedure is taken as the uncertainty. This

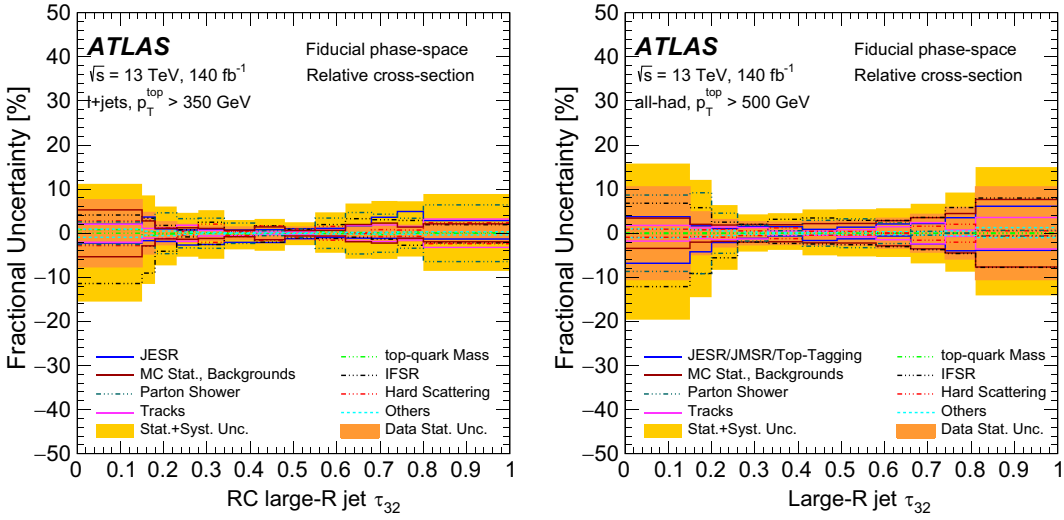

FIG. 7. Fractional uncertainties in the particle-level differential $t\bar{t}$ production cross section as a function of τ_{32}. The uncertainties are evaluated in the (a) ℓ + jets channel and (b) all-hadronic channel. The orange band represents the data statistical uncertainty, while the yellow band represents the total uncertainty. The uncertainties in the top-quark p_{T} mismodeling, leptons, $E_{\mathrm{T}}^{\mathrm{miss}}$, flavor tagging, pile-up and PDF have a very limited impact and are grouped in the plot under the label "Others".

uncertainty was already mentioned as unfolding nonclosure in Sec. VII C.

E. Summary of systematic uncertainties

The resulting systematic uncertainties affect each unfolded variable differently and are determined bin-by-bin, although their scales are comparable. As an example, the sizes of the systematic uncertainties in the normalized differential cross section as a function of τ_{32} are shown in Fig. 7. The uncertainties are generally below 5% and around 5% in the ℓ + jets channel and all-hadronic channel, respectively, and reach ∼40% at low and high τ_{32}, where the differential cross section is smaller, especially at low values of τ_{32}. The dominant uncertainty varies bin-by-bin. The FSR and the parton-shower and hadronization models are the sources of the largest signal-modeling uncertainties, while the JES/JER and charged-track uncertainties yield the largest detector-level uncertainties.

IX. RESULTS

The normalized particle-level fiducial phase-space differential cross sections as a function of the substructure observables are shown for both the ℓ + jets and all-hadronic channels. A set of double-differential cross sections is also presented. The results are compared with several NLOME + PS predictions of the Standard Model, including several tuning variations of the nominal POWHEG+PYTHIA8 prediction.

A quantitative comparison with the predictions is shown in Sec. IX C, where χ^2 and p-value calculations are presented.

A. Single-differential cross sections

The normalized particle-level single-differential cross sections for the ℓ + jets and all-hadronic channels are shown in Figs. 8–15.

The unfolded distributions are generally similar in shape between the two channels, although the distributions from the all-hadronic channel tend to be narrower, consistent with the SM predictions and arising from the higher p_{T}-interval used in the all-hadronic channel. The precision of the unfolded distributions allows qualitative and quantitative comparisons with SM predictions. The effect of the mismodeling of the top-quark p_{T}, introduced in Sec. V D, on the measured distributions is covered by the dedicated uncertainty introduced in Sec. VIII D. This uncertainty is non-negligible only in the observables correlated with the top-quark p_{T} (ECF2, *LHA*, $p_{\mathrm{T}}^{\mathrm{d},*}$) and relevant only in the tails of the distributions, where it reaches a 10% effect in the all-hadronic channel.

The τ_{32} distributions show a rapid increase around 0.2 followed by a plateau out to about 0.8 for the ℓ + jets channel and a decrease out to 0.8 for the all-hadronic channel. The general behavior reflects the three-body nature of the top-quark decay. The SM nominal POWHEG+PYTHIA8 and FSR Up predictions tend to overestimate the τ_{32} distributions at low values and correspondingly underestimate them at higher values. The prediction made by the POWHEG+HERWIG7 MC generator is in best agreement with the data. The same behavior is also observed for the τ_3 prediction.

The τ_{21} distributions show a rising trend from 0.0 out to 0.5, where they then fall off quickly. This reflects

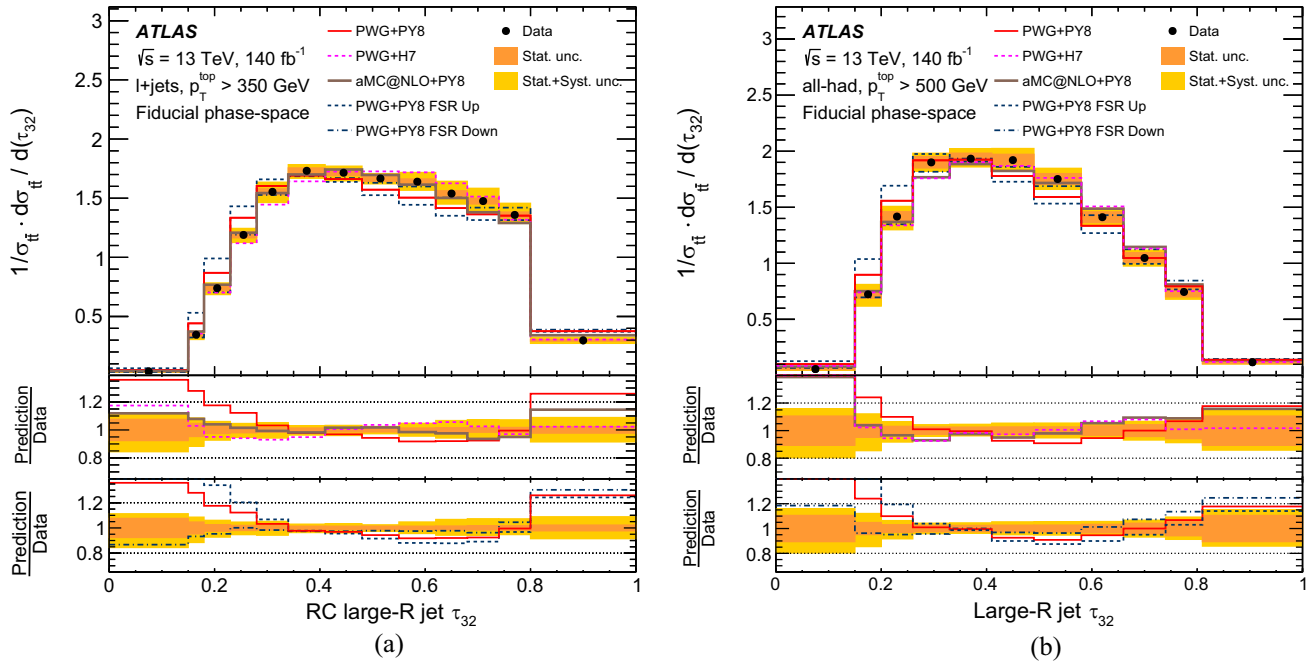

FIG. 8. Particle-level normalized differential cross sections as a function of τ_{32} for the data and several NLOME + PS MC predictions. The unfolded results shown here are in the (a) ℓ + jets and (b) all-hadronic channels. The lower pads show the ratios of the predictions to the data. The yellow band represents the total uncertainty of the measured differential cross section, while the orange band shows the statistical component.

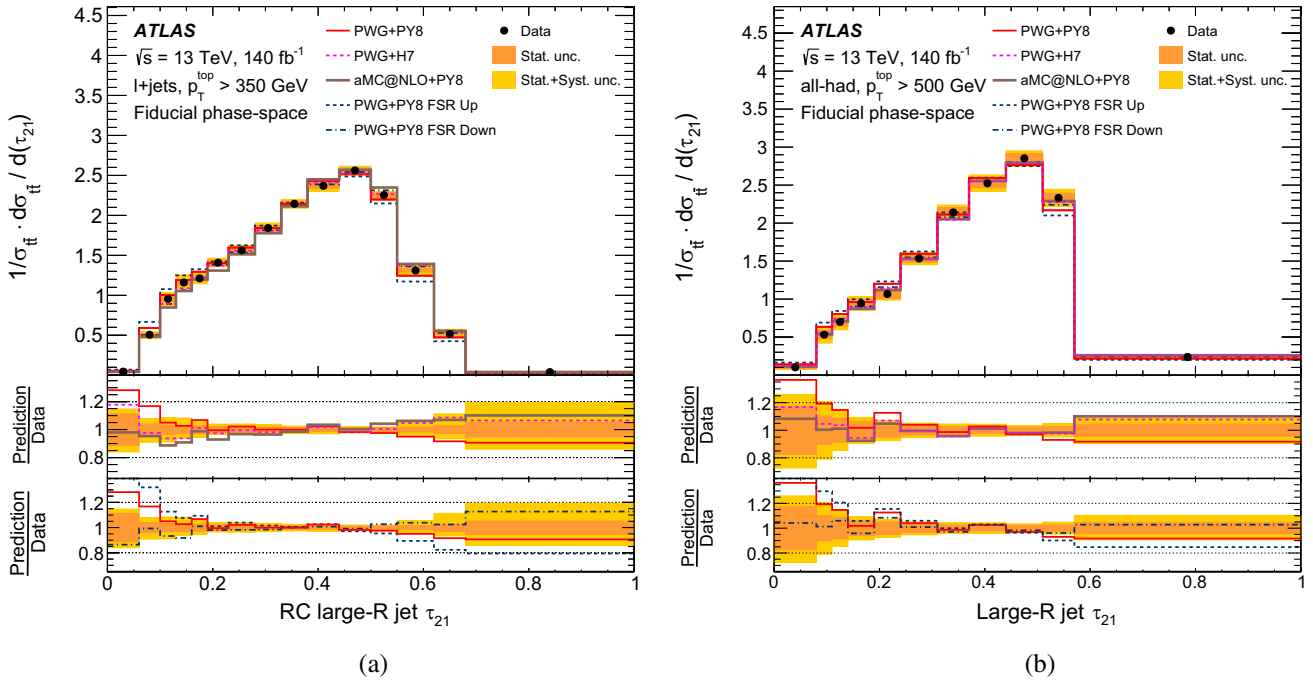

FIG. 9. Particle-level normalized differential cross sections as a function of τ_{21} for the data and several NLOME + PS MC predictions. The unfolded results shown here are in the (a) ℓ + jets and (b) all-hadronic channels. The lower pads show the ratios of the predictions to the data. The yellow band represents the total uncertainty of the measured differential cross section, while the orange band shows the statistical component.

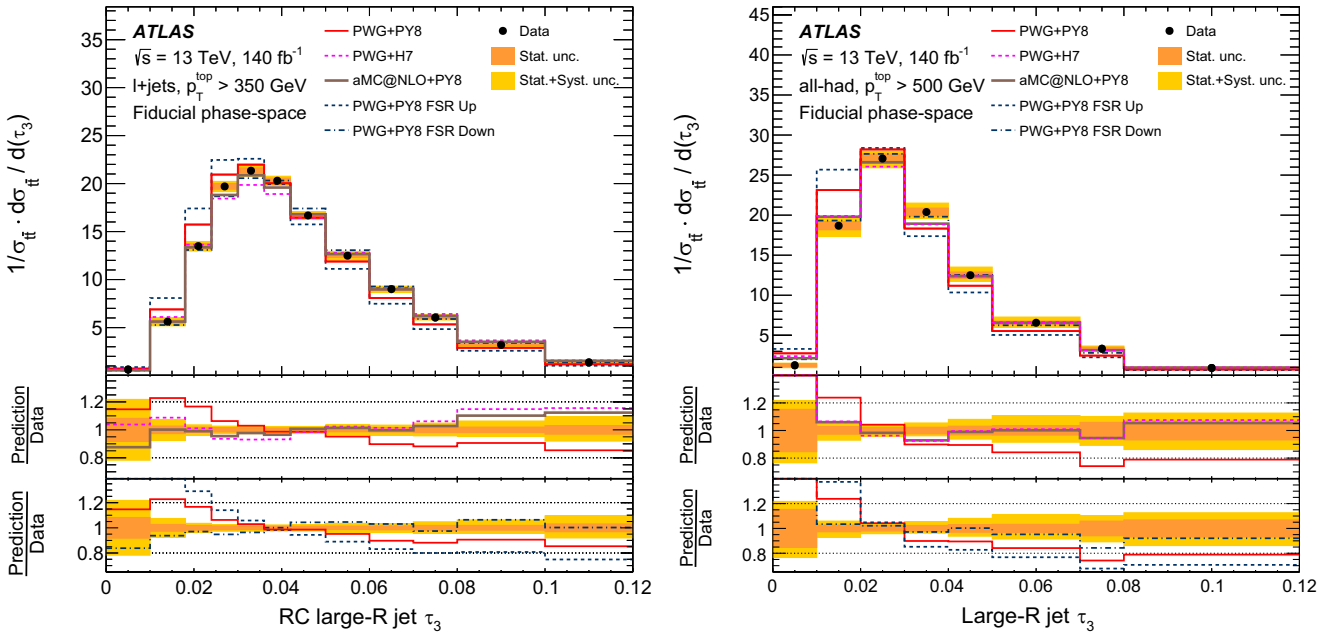

FIG. 10. Particle-level normalized differential cross sections as a function of τ_3 for the data and several NLOME + PS MC predictions. The unfolded results shown here are in the (a) ℓ + jets and (b) all-hadronic channels. The lower pads show the ratios of the predictions to the data. The yellow band represents the total uncertainty of the measured differential cross section, while the orange band shows the statistical component.

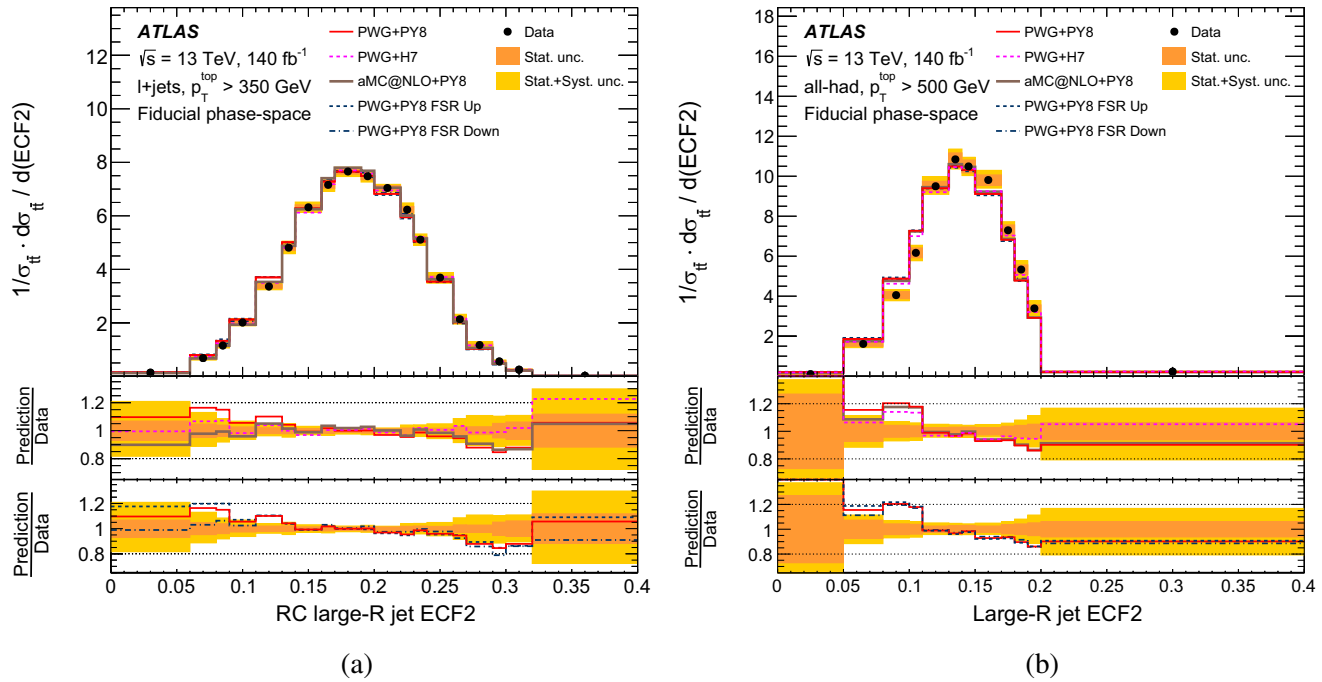

FIG. 11. Particle-level normalized differential cross sections as a function of *ECF*2 for the data and several NLOME + PS MC predictions. The unfolded results shown here are in the (a) ℓ + jets and (b) all-hadronic channels. The lower pads show the ratios of the predictions to the data. The yellow band represents the total uncertainty of the measured differential cross section, while the orange band shows the statistical component.

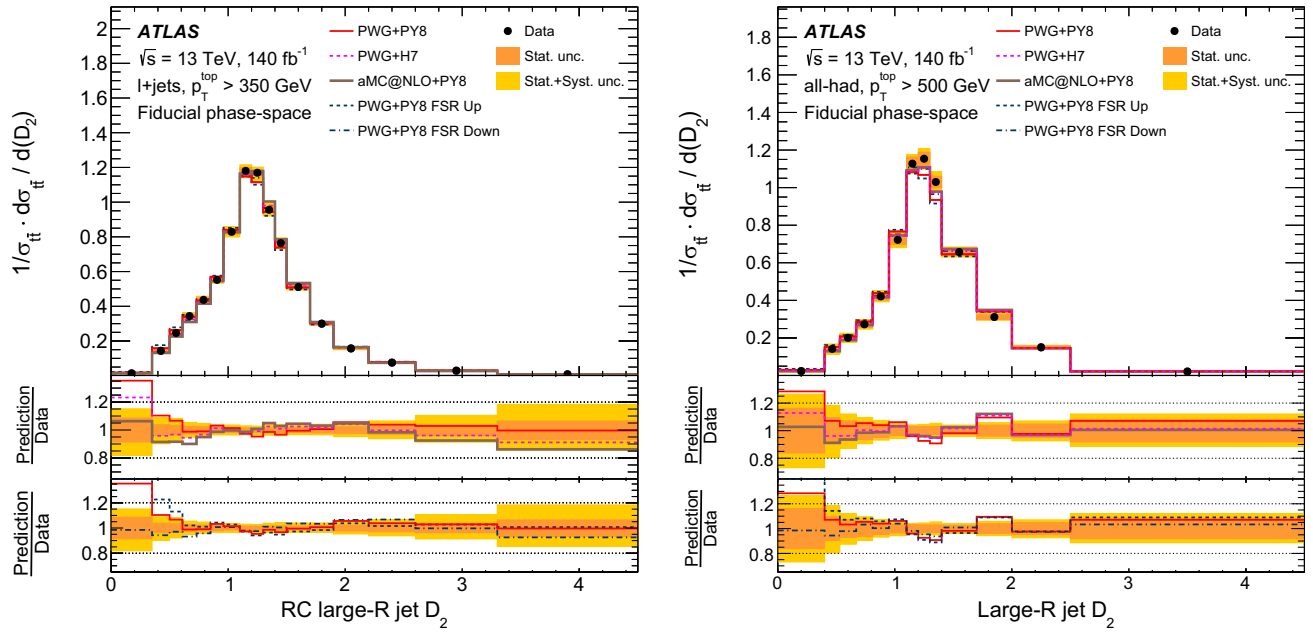

(a) (b)

FIG. 12. Particle-level normalized differential cross sections as a function of D_2 for the data and several NLOME + PS MC predictions. The unfolded results shown here are in the (a) ℓ + jets and (b) all-hadronic channels. The lower pads show the ratios of the predictions to the data. The yellow band represents the total uncertainty of the measured differential cross section, while the orange band shows the statistical component.

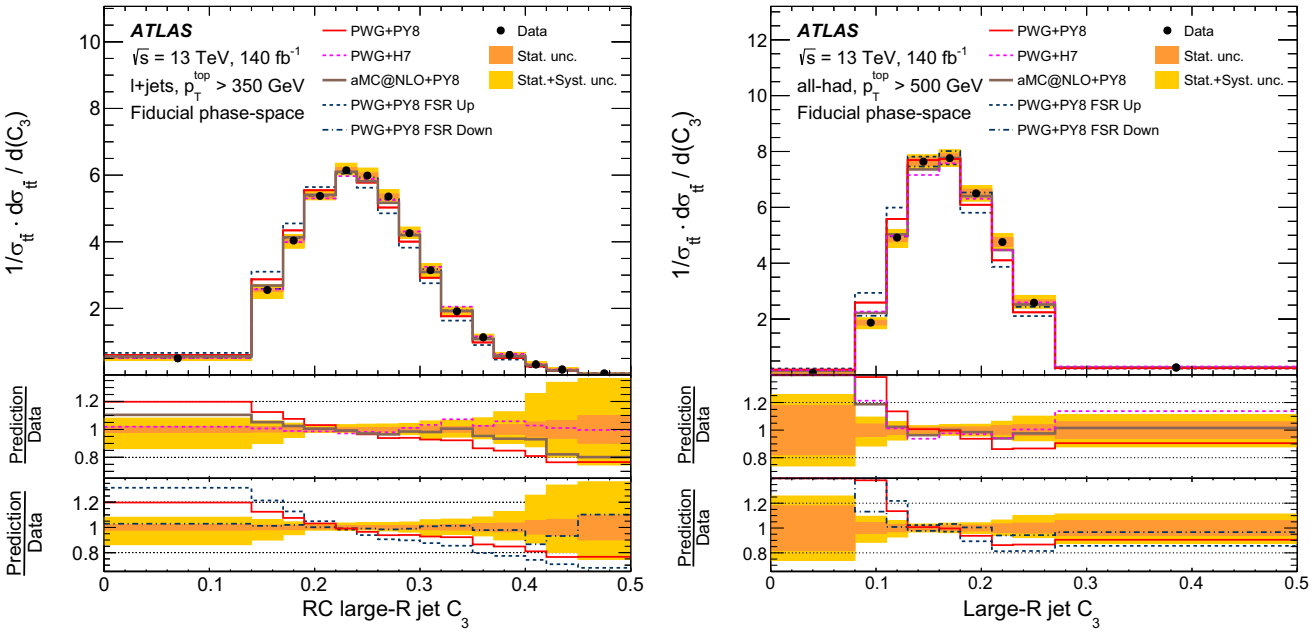

(a) (b)

FIG. 13. Particle-level normalized differential cross sections as a function of C_3 for the data and several NLOME + PS MC predictions. The unfolded results shown here are in the (a) ℓ + jets and (b) all-hadronic channels. The lower pads show the ratios of the predictions to the data. The yellow band represents the total uncertainty of the measured differential cross section, while the orange band shows the statistical component.

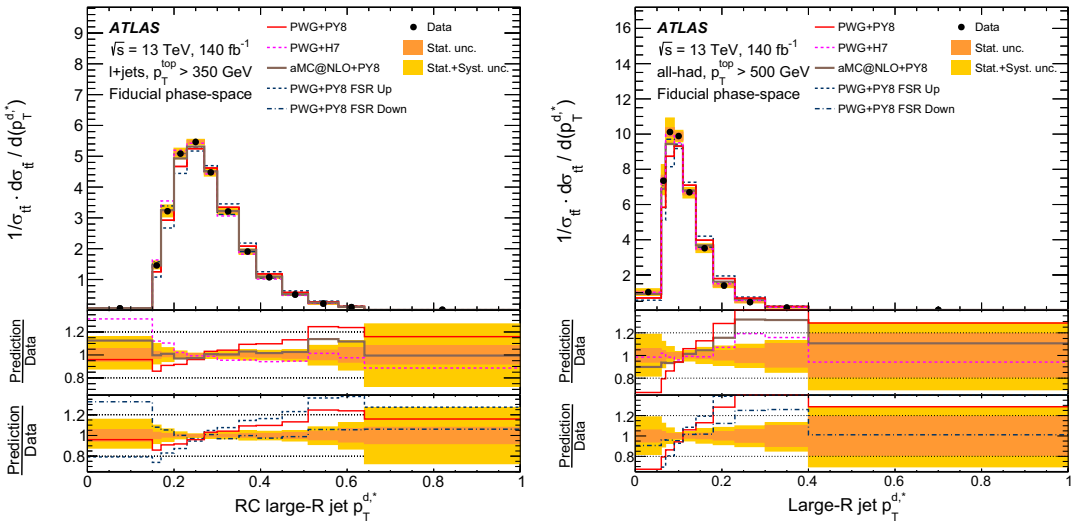

FIG. 14. Particle-level normalized differential cross sections as a function of jet p_{T} dispersion for the data and several NLOME + PS MC predictions. The unfolded results shown here are in the (a) ℓ + jets and (b) all-hadronic channels. The lower pads show the ratios of the predictions to the data. The yellow band represents the total uncertainty of the measured differential cross section, while the orange band shows the statistical component.

the general absence of two-body structure in these jets. The MC predictions are in good agreement with the data, with a slight overestimation of the distributions for τ_{21} below ∼0.3.

The ℓ + jets and all-hadronic channels show a similar trend in the C_3 predictions from several generators, with the SM predictions that tend to overestimate the data at low values of C_3 underestimating it in the right tail of the distribution. The D_2 SM predictions are in good agreement with the ℓ + jets channel's distribution while the predicted distribution in the all-hadronic channel is somewhat broader than what is observed.

While the measured *LHA* and *ECF*2 distributions agree within the uncertainty band with all the predictions in most of the bins, a large discrepancy is observed in the $p_{\mathrm{T}}^{\mathrm{d},*}$ distribution for the POWHEG+PYTHIA8 prediction in both channels, while POWHEG+HERWIG7 seems to provide a better description of this observable.

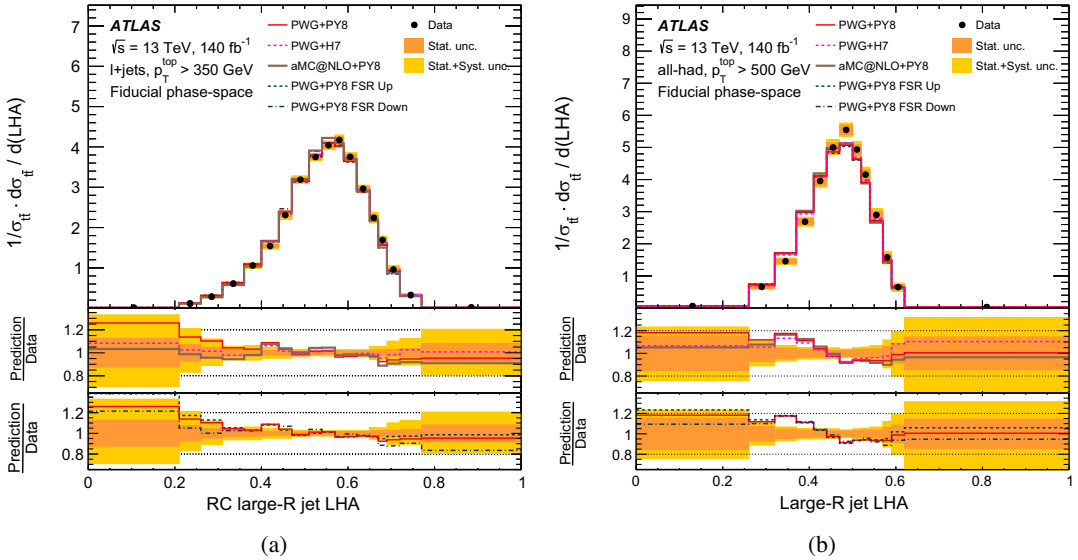

FIG. 15. Particle-level normalized differential cross sections as a function of *LHA* for the data and several NLOME + PS MC predictions. The unfolded results shown here are in (a) the ℓ + jets and (b) the all-hadronic channels. The lower pads show the ratios of the predictions to the data. The yellow band represents the total uncertainty of the measured differential cross section, while the orange band shows the statistical component.

B. Double-differential cross sections

The normalized particle-level double-differential cross sections for the ℓ + jets channel are shown in Figs. 16–19, while the corresponding results for the all-hadronic channel are displayed in Figs. 20–23. The normalization considers the whole spectrum, so each bin is divided by the integral of the double-differential distribution.

The four figures for each channel present the correlations between τ_{32} and m^{top}, τ_{32} and $p_{\text{T}}^{\text{top}}$, D_2 and m^{top}, and D_2 and $p_{\text{T}}^{\text{top}}$. The τ_{32} and D_2 substructure variables have the power to separate jets with three-body or two-body substructure from jets with simpler topologies and have been employed in various taggers. Therefore, their correlations with m^{top} and $p_{\text{T}}^{\text{top}}$ are of particular interest.

The distributions of τ_{32} versus m^{top} predicted by the various MC generators generally show poor agreement in the central m^{top} interval and better agreement at both low and high m^{top}, where there are large systematic uncertainties, due to the jet energy resolution. Agreement between data and predictions is somewhat better in the all-hadronic channel than in the ℓ + jets channel, although similar trends are observed in both.

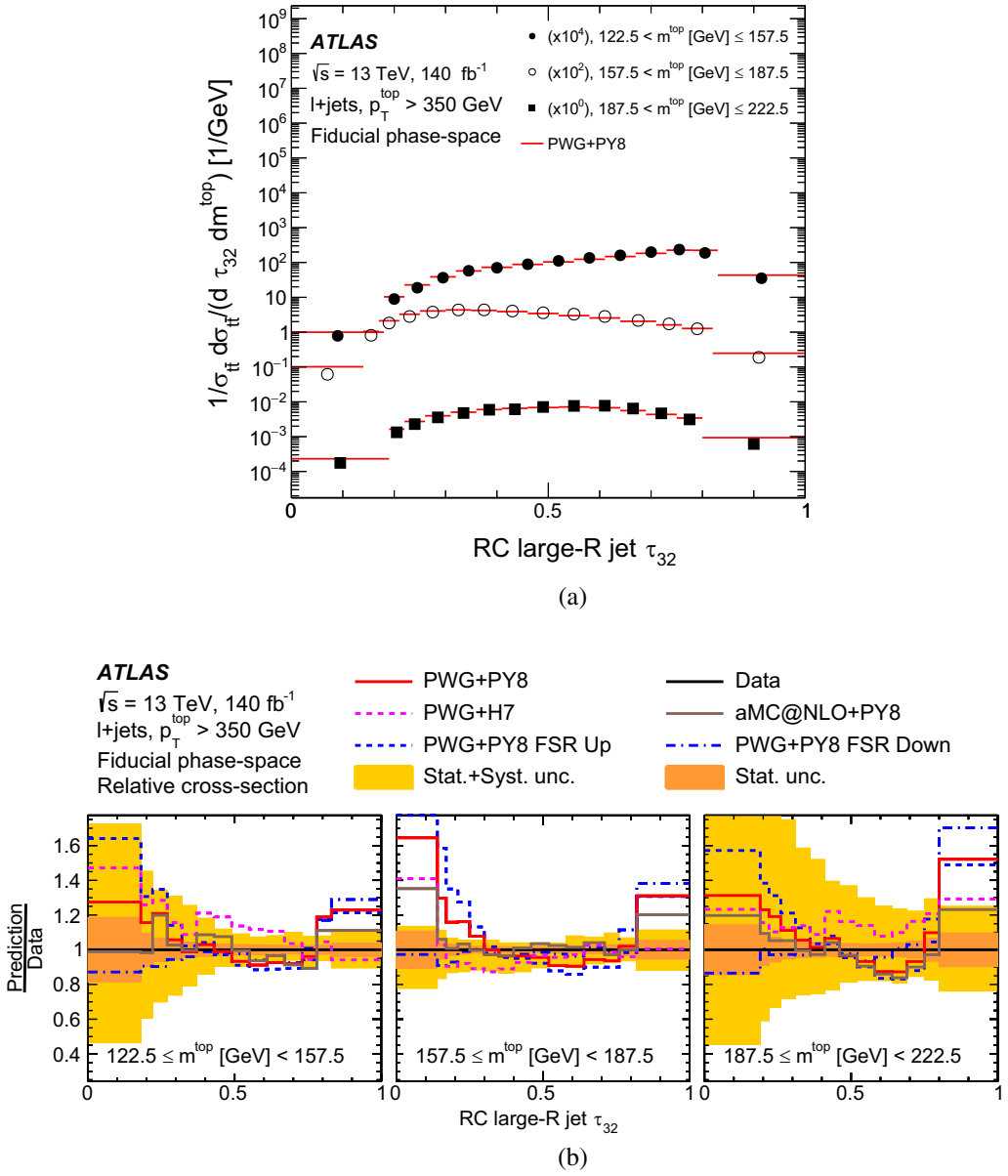

FIG. 16. Particle-level differential $t\bar{t}$ production cross section as a function of τ_{32} and jet mass, for several NLOME + PS predictions of $t\bar{t}$ signal and the data. The events shown here are from the ℓ + jets channel: (a) shows the data and the nominal prediction, while (b) shows the ratios of the predictions to the data. The lighter band represents the total uncertainty of the measured differential cross section, while the darker band shows the statistical component.

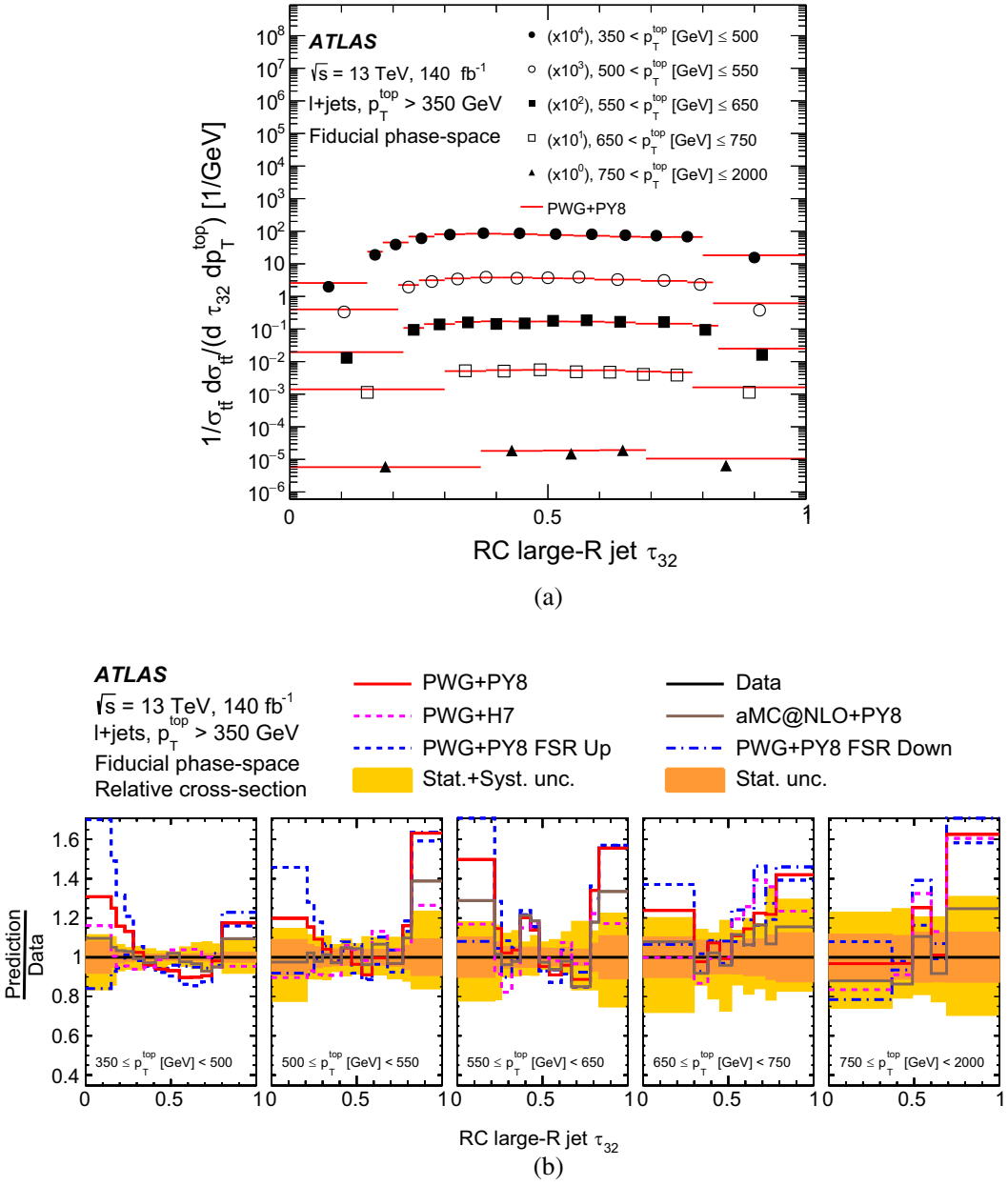

FIG. 17. Particle-level differential $t\bar{t}$ production cross section as a function of τ_{32} and jet p_{T}, for several NLOME + PS predictions of $t\bar{t}$ signal and the data. The events shown here are from the ℓ + jets channel: (a) shows the data and the nominal prediction, while (b) shows the ratios of the predictions to the data. The lighter band represents the total uncertainty of the measured differential cross section, while the darker band shows the statistical component.

The distribution of τ_{32} versus $p_{\mathrm{T}}^{\mathrm{top}}$ and the predictions show similar trends and are in reasonable agreement at values of τ_{32} between 0.4 and 0.7. The MC predictions are generally larger than the data at lower and higher τ_{32}.

The predictions of D_2 correlations with m^{top} and $p_{\mathrm{T}}^{\mathrm{top}}$ from the various MC generators are generally in better agreement with the unfolded data, although there are considerable variations between the predictions at both low and high D_2. However, these variations are smaller than those seen in the comparisons of the τ_{32} predictions.

Overall, these correlations show that the MC predictions tend to have more three-body-like substructure than observed in the data. This disagreement does not have a strong $p_{\mathrm{T}}^{\mathrm{top}}$ dependence, but appears to be larger in the central m^{top} region. The results for the all-hadronic and ℓ + jets channels are similar, although agreement is generally better in the all-hadronic channel.

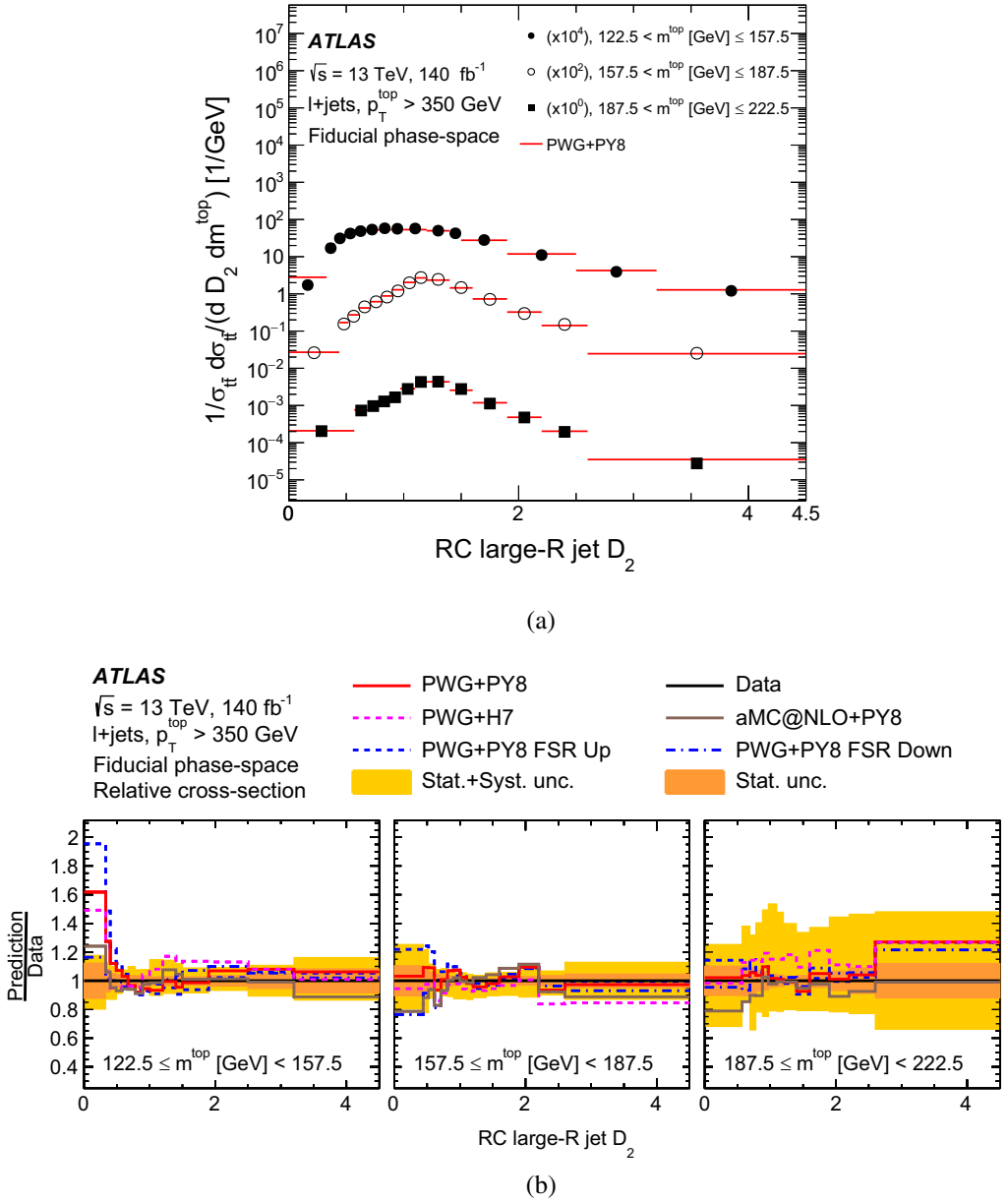

FIG. 18. Particle-level differential $t\bar{t}$ production cross section as a function of D_2 and jet mass, for several NLOME + PS predictions of $t\bar{t}$ signal and the data. The events shown here are from the ℓ + jets channel: (a) shows the data and the nominal prediction, while (b) shows the ratios of the predictions to the data. The lighter band represents the total uncertainty of the measured differential cross section, while the darker band shows the statistical component.

C. Comparisons of predicted and observed substructure variables

The level of agreement between the measured differential cross sections and the SM predictions is quantified by a χ^2 test-statistic and the related p-value extracted from the reduced χ^2 distribution. The χ^2 calculation for the vector V, which contains the residuals between data and the theory predictions, is

$$\chi^2 = V^T \times C^{-1} \times V,$$

where the covariance matrix C incorporates the statistical uncertainties, the bin-by-bin correlations induced by the presence of the systematic uncertainties, and the regularization used to unfold the data to the particle-level differential cross sections. The covariance matrix is evaluated assuming no correlations between the different uncertainty sources. This method has been used in several $t\bar{t}$ differential cross-section measurements [151].

The covariances evaluated for normalized spectra are not invertible since the number of rows and columns is larger than the rank. Consequently, one column and the

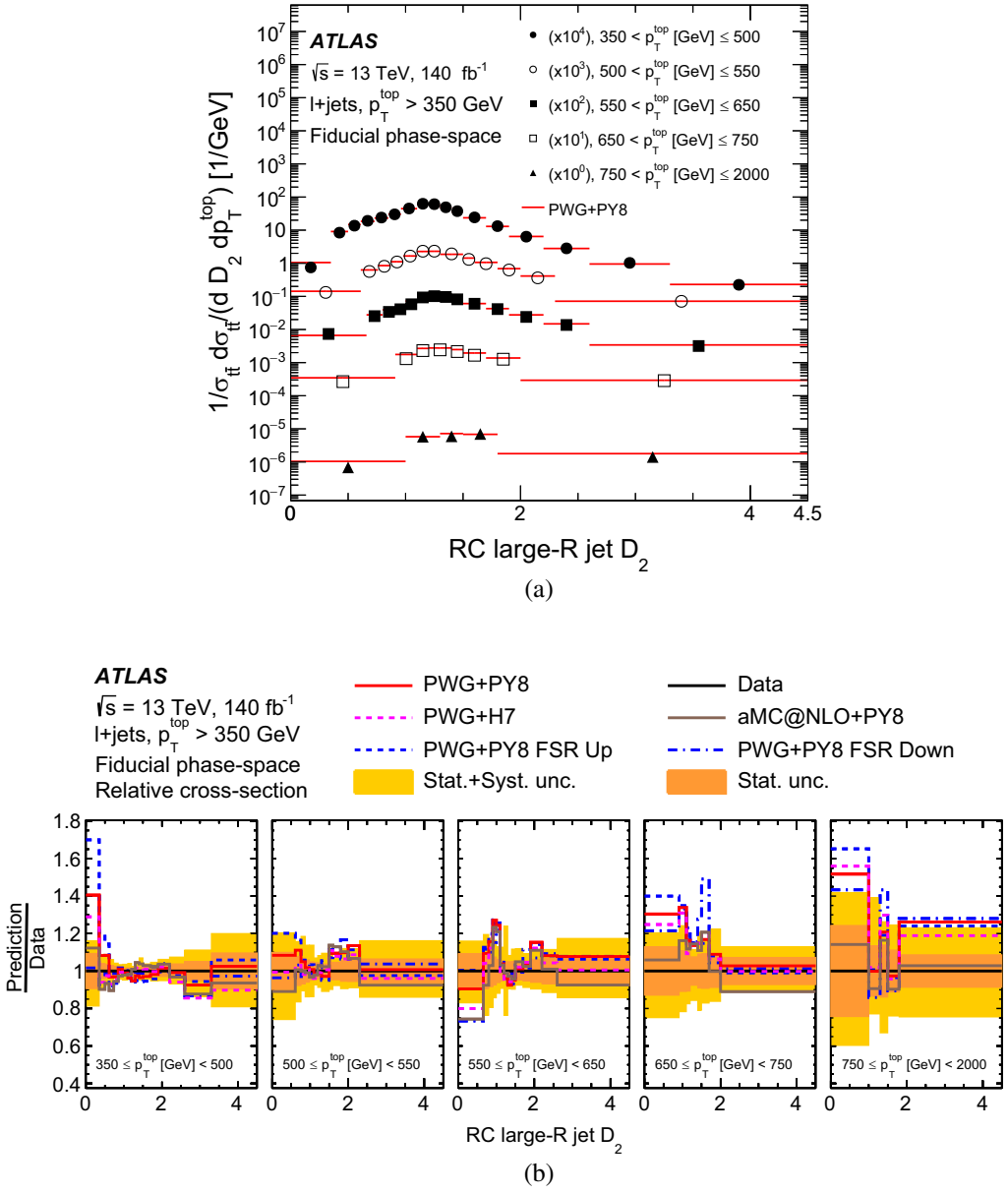

FIG. 19. Particle-level differential $t\bar{t}$ production cross section as a function of D_2 and jet p_{T}, for several NLOME + PS predictions of $t\bar{t}$ signal and the data. The events shown here are from the ℓ + jets channel: (a) shows the data and the nominal prediction, while (b) shows the ratios of the predictions to the data. The lighter band represents the total uncertainty of the measured differential cross section, while the darker band shows the statistical component.

corresponding row are removed from the covariance matrix, as is the relevant element of the residuals vector. The resulting χ^2 does not depend on the row or column removed. No theoretical uncertainties are included in the predictions used in the χ^2 calculation because each χ^2 value reflects the comparison of data with a specific model.

The χ^2 comparisons between the predicted and unfolded distributions are shown in Tables II and III. The unfolded differential cross sections are compared with the five different MC predictions, and the resulting χ^2/NDF and p-values are shown for each distribution.

These quantitative comparisons reflect the qualitative comparisons made earlier, but also illustrate that overall agreement with the data is better for some MC predictions than others. In particular, the predictions from POWHEG+PYTHIA8 (FSR Up) are in quite poor agreement with the observations, with p-values less than 0.01 for all but two ℓ + jets variables. There is similarly poor agreement between the POWHEG+PYTHIA8 (FSR Up) predictions and data in the all-hadronic channel, although in that case the predictions for the τ_{21}, D_2 and LHA variables are in reasonable agreement with data, with a p-value larger than 0.3. Even for these variables the FSR Up predictions give

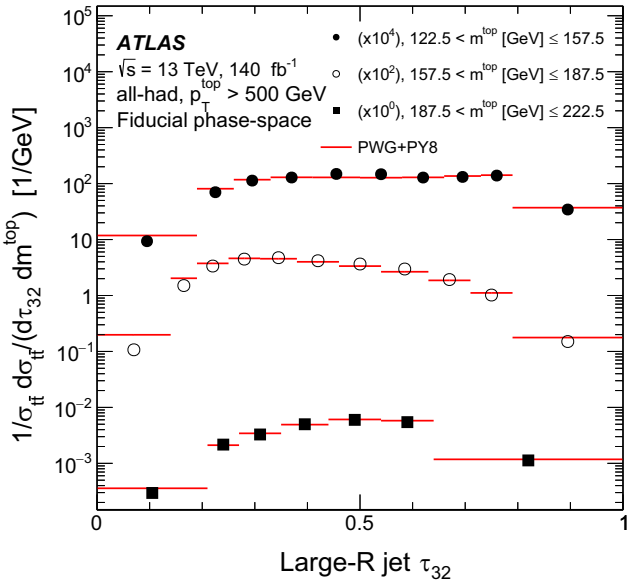

(a)

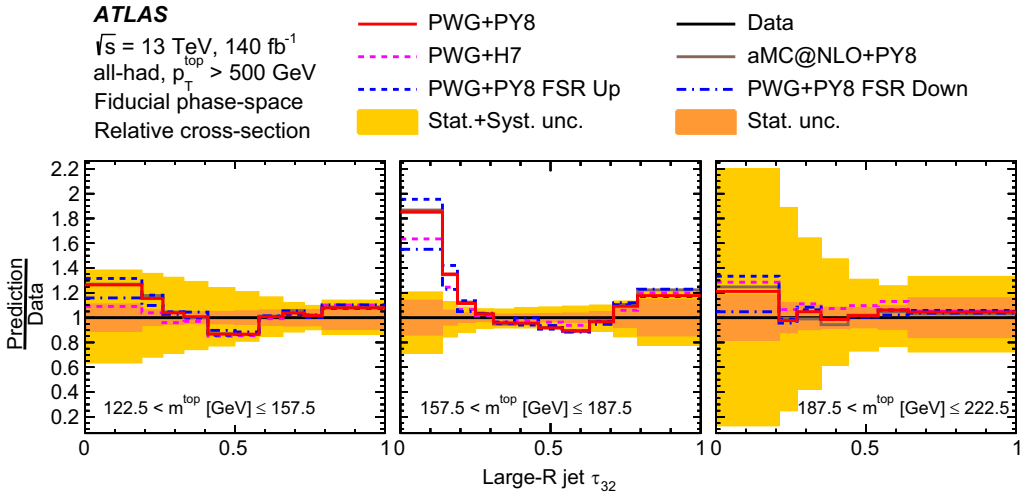

(b)

FIG. 20. Particle-level differential $t\bar{t}$ production cross section as a function of τ_{32} and jet mass, for several NLOME + PS predictions of $t\bar{t}$ signal and the data. The events shown are from the all-hadronic channel: (a) shows the data and the nominal prediction, while (b) shows the ratios of the predictions to the data. The lighter band represents the total uncertainty of the measured differential cross section, while the darker band shows the statistical component.

the worst description of the data among the tested MC predictions. In contrast, the POWHEG+PYTHIA8 (FSR Down) prediction provides a good description, with a p-value larger than 0.01 for all single-differential observables except τ_{32} in the ℓ + jets channel. Overall, the measured distributions favor a lower FSR scale, corresponding to a higher α_s^{FSR} value. This is consistent with recent tuning studies performed using ATLAS data [152] and with the recent CMS top-quark mass measurement using boosted top quarks, which employed the τ_{32} distribution to tune α_s^{FSR} [153].

The predictions of the other NLOME + PS calculations are generally in good agreement with the data. It is noteworthy that most predictions for the τ_{32} variable are generally in poor agreement with the data, with p-values lower than 0.1 for several generator setups and with the POWHEG+PYTHIA8 predictions having $\chi^2/\mathrm{NDF} = 54/12$ and $24/10$ for the ℓ + jets and all-hadronic channels, respectively. This shows that the NLOME + PS predictions are unable to accurately model the three-body nature of boosted top-quark jets. Notably, the τ_3 variable is also generally described poorly by the predictions, at the same

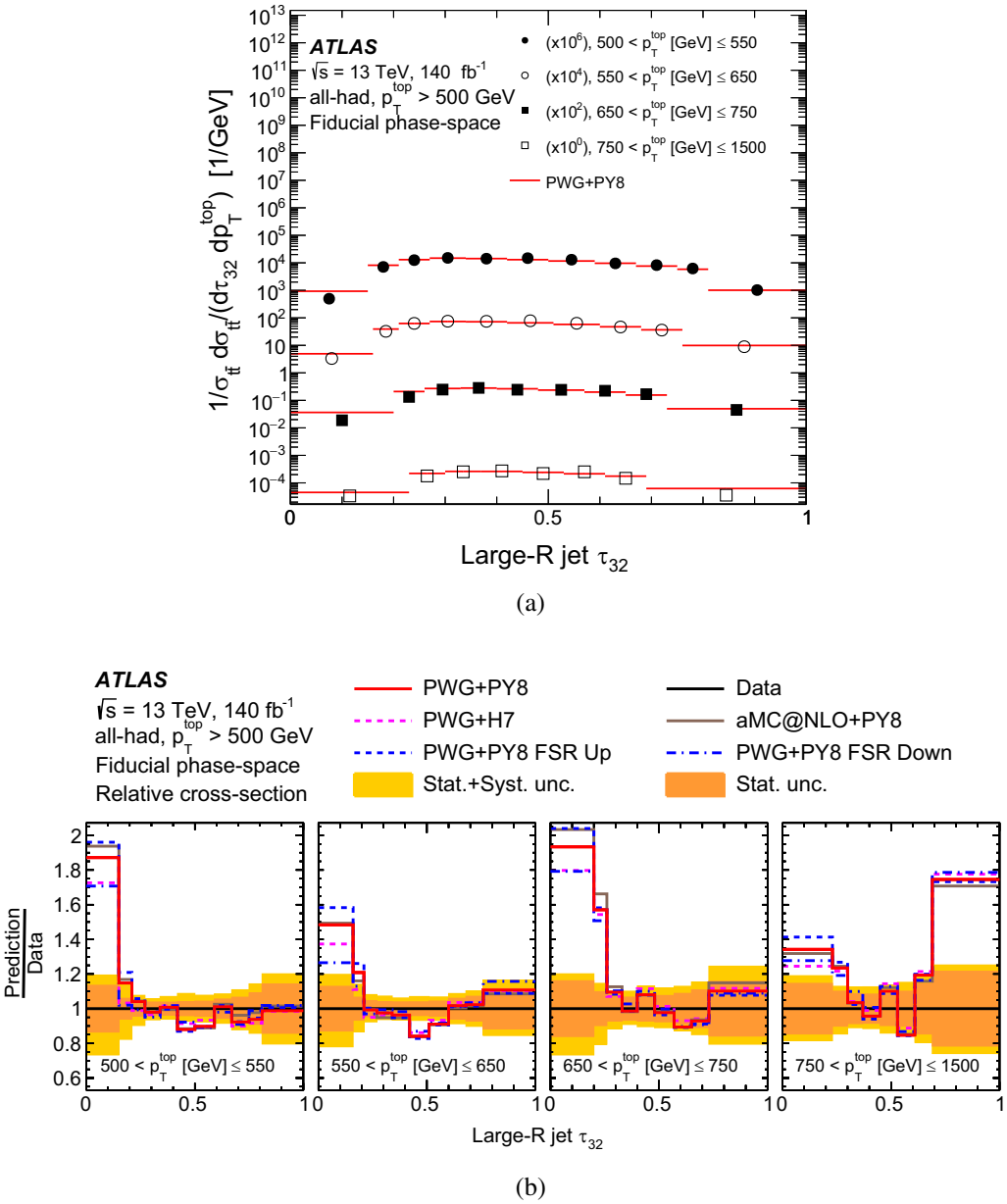

FIG. 21. Particle-level differential $t\bar{t}$ production cross section as a function of τ_{32} and jet p_{T}, for several NLOME + PS predictions of $t\bar{t}$ signal and the data. The events shown here are from the all-hadronic channel: (a) shows the data and the nominal prediction, while (b) shows the ratios of the predictions to the data. The lighter band represents the total uncertainty of the measured differential cross section, while the darker band shows the statistical component.

level as τ_{32} or worse, which correlates with poor τ_{32} agreement and further implicates the three-body modeling. One exception comes from aMC@NLO, which provides a fair description of τ_{32} and τ_3 in both channels, with p-values larger than 0.2. The variables that are sensitive to the modeling of one-body and two-body substructure (τ_{21}, ECF2 and D_2) show good agreement with data, with p-values ranging from 0.2 to 0.82, depending on the generator and the channel.

The C_3 variable, a probe of three-body structure that is interpreted as a measure of the higher-order radiation relative to the lowest-order prediction, is reasonably well modeled by most of the ℓ + jets calculations, with three p-values exceeding 0.9, but interestingly is not well modeled by most predictions in the all-hadronic channel. This could be due to mismodeling of the internal radiation in the top-quark jet at higher p_{T} or perhaps the modeling of the energy flow between these higher-p_{T} jets in this all-hadronic final state.

The $p_{\mathrm{T}}^{\mathrm{d},*}$ variable is a measure of the distribution of the momentum between particles within the jet, and is therefore sensitive to the hadronization model. It is not well

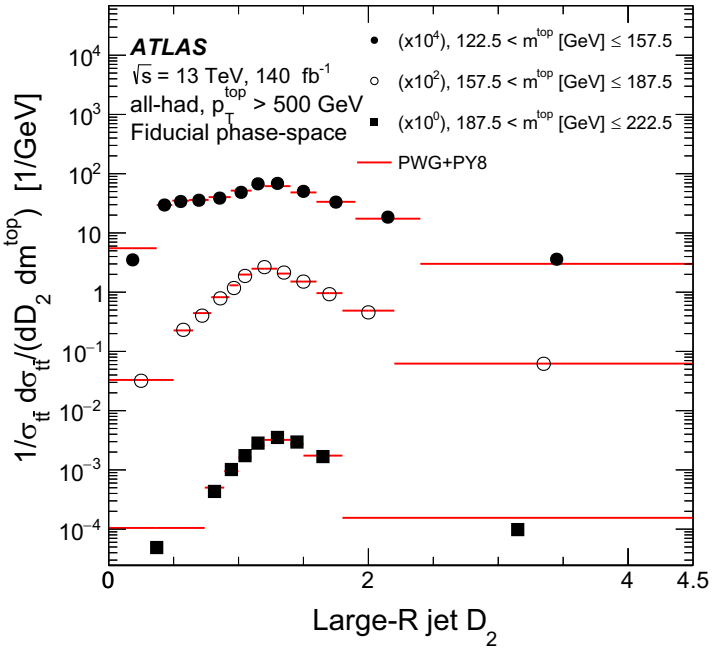

(a)

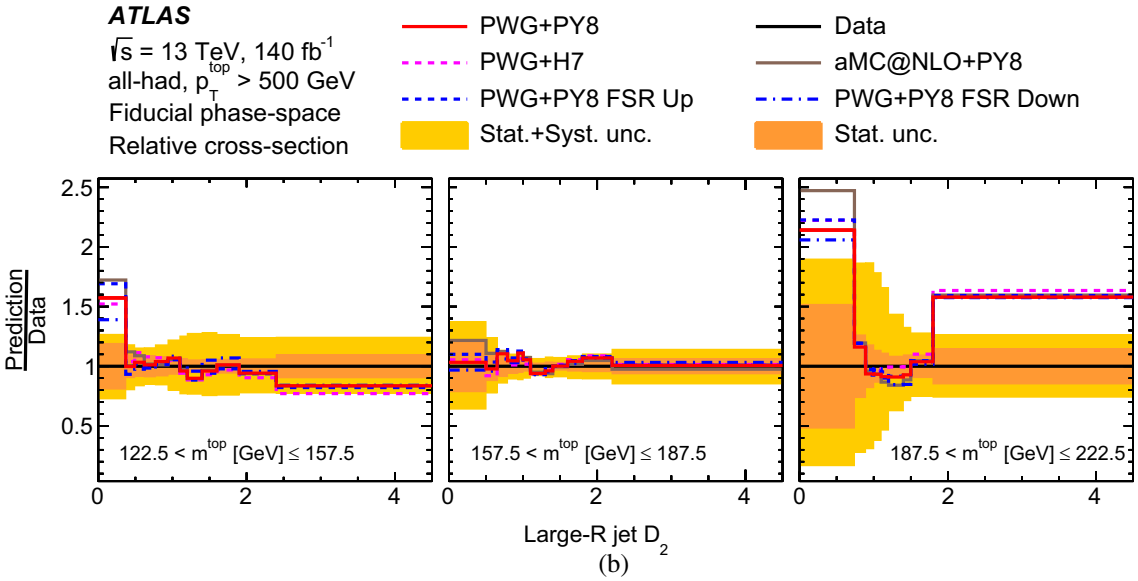

(b)

FIG. 22. Particle-level differential $t\bar{t}$ production cross section as a function of D_2 and jet mass, for several NLOME + PS predictions of $t\bar{t}$ signal and the data. The events shown are from the all-hadronic channel: (a) shows the data and the nominal prediction, while (b) shows the ratios of the predictions to the data. The lighter band represents the total uncertainty of the measured differential cross section, while the darker band shows the statistical component.

described by the POWHEG+PYTHIA8 model, but agreement improves with a higher value of α_s^{FSR}, especially in the all-hadronic channel, where the p-value reaches 0.54.

The *LHA* variable, which is more sensitive to the modeling of the energy of the high-energy constituents, is well described by the predictions. This variable, and also ECF2, was selected because it was not expected to be highly sensitive to the FSR variations. POWHEG+HERWIG7 gives the best description of these variables in both the ℓ + jets and all-hadronic channels, with p-values of 0.92 and 0.74 respectively for *LHA*.

The double-differential cross sections provide more information about the correlations of the two-body and three-body substructure measures, D_2 and τ_{32}. Although D_2 appears to be well modeled overall by most predictions, the modeling of its correlations with m^{top} and $p_{\mathrm{T}}^{\mathrm{top}}$ is

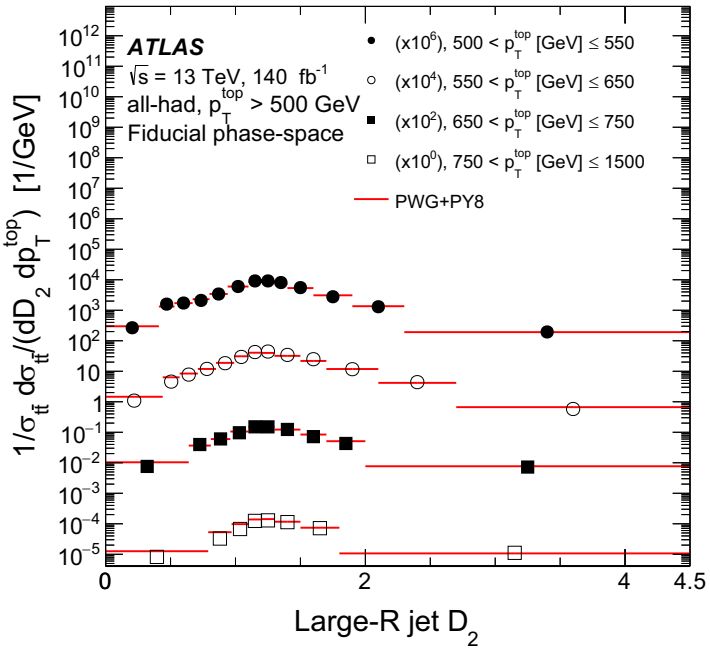

(a)

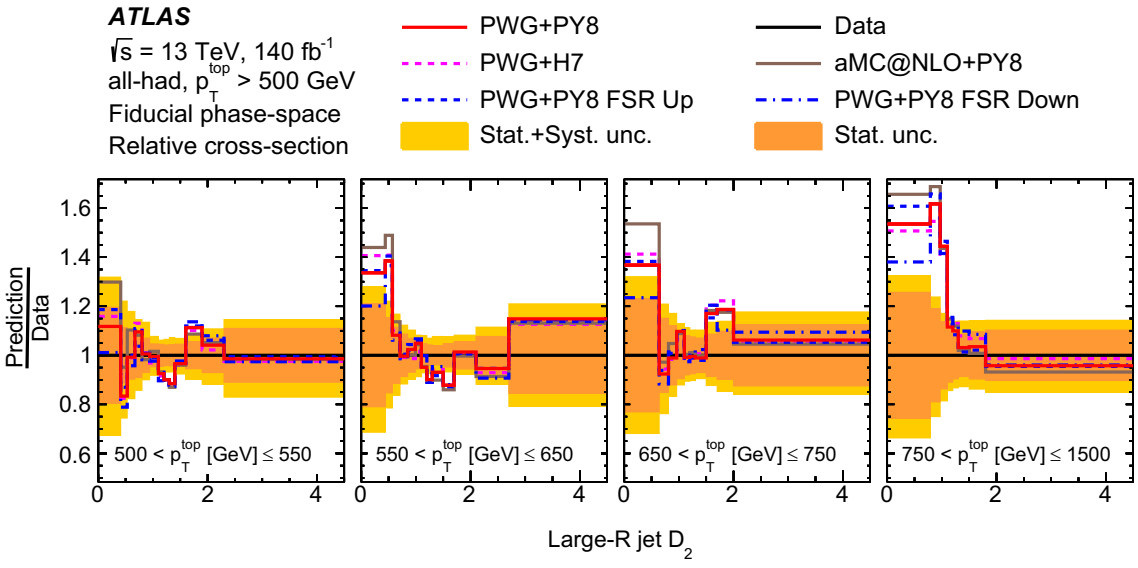

(b)

FIG. 23. Particle-level differential $t\bar{t}$ production cross section as a function of D_2 and jet p_{T}, for several NLOME + PS predictions of $t\bar{t}$ signal and the data. The events shown are from the all-hadronic channel: (a) shows the data and the nominal prediction, while (b) shows the ratios of the predictions to the data. The lighter band represents the total uncertainty of the measured differential cross section, while the darker band shows the statistical component.

relatively poor in the ℓ + jets channel. This arises from the difficulty of modeling D_2 at lower m^{top} and higher $p_{\mathrm{T}}^{\mathrm{top}}$. For τ_{32}, the correlations are even more poorly modeled in the ℓ + jets channel, with p-values less than 0.01 for several NLOME + PS predictions. The trends observed in the double-differential distributions for the two channels are similar, although the discrimination power in the all-hadronic channel is more limited by the statistical uncertainty.

Overall, the picture that emerges is that the POWHEG+PYTHIA8 (FSR Up) model is not successful in describing the substructure of these high-p_{T} jets. Compared with the nominal POWHEG+PYTHIA8 prediction, all POWHEG+HERWIG7, AMC@NLO+PYTHIA8 and POWHEG+PYTHIA8

TABLE II. χ^2 and p-values quantifying the level of agreement between the unfolded spectra in the ℓ + jets channel and several normalized NLO + PS predictions. PWG+PY8 corresponds to the POWHEG+PYTHIA sample and PWG + H7 to the POWHEG+HERWIG sample.

	PWG+PY8		PWG+H7		AMC@NLO+PY8		PWG+PY8(FSR Up)		PWG+PY8(FSR Down)	
Observable	χ^2/NDF	p-value	χ^2/NDF	p-value	χ^2/NDF	p-value	χ^2/NDF	p-value	χ^2/NDF	p-value
τ_{32}	54/12	<0.01	19/12	0.09	15/12	0.24	165/12	<0.01	40/12	<0.01
τ_{21}	14/14	0.41	7/14	0.92	16/14	0.32	42/14	<0.01	8/14	0.91
τ_3	36/11	<0.01	42/11	<0.01	14/11	0.23	130/11	<0.01	23/11	0.02
ECF2	25/18	0.13	13/18	0.78	15/18	0.69	31/18	0.03	24/18	0.14
D_2	20/16	0.20	17/16	0.39	20/16	0.20	37/16	<0.01	15/16	0.49
C_3	11/14	0.65	6/14	0.97	3/14	1.00	35/14	<0.01	3/14	1.00
$p_{\mathrm{T}}^{\mathrm{d},*}$	27/12	<0.01	10/12	0.58	11/12	0.53	56/12	<0.01	24/12	0.02
LHA	14/17	0.65	9/17	0.92	20/17	0.29	14/17	0.69	19/17	0.32
D_2 vs. m^{top}	61/42	0.03	62/42	0.02	59/42	0.05	118/42	<0.01	44/42	0.37
D_2 vs. $p_{\mathrm{T}}^{\mathrm{top}}$	71/56	0.08	68/56	0.13	70/56	0.11	107/56	<0.01	93/56	<0.01
τ_{32} vs. m^{top}	153/42	<0.01	72/42	<0.01	56/42	0.07	413/42	<0.01	77/42	<0.01
τ_{32} vs. $p_{\mathrm{T}}^{\mathrm{top}}$	153/50	<0.01	103/50	<0.01	57/50	0.23	360/50	<0.01	114/50	<0.01

(FSR Down) predictions are in better agreement with the measurements for most observables, and the POWHEG+PYTHIA8 (FSR Down) predictions are in closest agreement with the measurements in both the ℓ + jets and all-hadronic channels. The correlations with m^{top} and $p_{\mathrm{T}}^{\mathrm{top}}$ provide some diagnostic information, which suggests that the most significant disagreement tends to be at lower m^{top} and higher $p_{\mathrm{T}}^{\mathrm{top}}$.

These results highlight the tension between the data and the predictions for key tagging variables such as τ_{32} and D_2, and better agreement will be essential in improving the tuning of the showering parameters. Better agreement with data for these observables would also reduce the modeling uncertainties affecting the top-quark taggers and lead to scaling factors closer to unity when correcting for tagger performance differences between data and simulation.

X. CONCLUSION

Top-quark jet substructure variables are measured for top-quark jets with $p_{\mathrm{T}} > 350$ GeV in a fiducial phase-space defined by the p_{T} and η of the jets. These measurements use 140 fb^{-1} of 13 TeV pp collision data collected by the ATLAS detector at the LHC, and are performed in both the lepton + jets and all-hadronic final states of $t\bar{t}$ events. The inclusion of the all-hadronic final state enables measurements of the substructure of top-quark jets with average p_{T} above 500 GeV. This analysis is the first to

TABLE III. χ^2 and p-values quantifying the level of agreement between the unfolded spectra in the all-hadronic channel and several suitably normalized NLO + PS predictions. PWG + PY8 corresponds to the POWHEG+PYTHIA sample and PWG + H7 to the POWHEG+HERWIG sample.

	PWG+PY8		PWG+H7		AMC@NLO+PY8		PWG+PY8(FSR UP)		PWG+PY8(FSR DOWN)	
Observable	χ^2/NDF	p-value	χ^2/NDF	p-value	χ^2/NDF	p-value	χ^2/NDF	p-value	χ^2/NDF	p-value
τ_{32}	24/10	<0.01	14/10	0.20	9/10	0.52	61/10	<0.01	6/10	0.82
τ_{21}	7/10	0.75	6/10	0.80	6/10	0.80	11/10	0.36	6/10	0.84
τ_3	29/7	<0.01	17/7	0.02	10/7	0.17	58/7	<0.01	8/7	0.29
ECF2	17/11	0.10	12/11	0.39	14/11	0.26	20/11	0.05	15/11	0.19
D_2	11/12	0.55	8/12	0.82	8/12	0.76	14/12	0.27	7/12	0.88
C_3	29/8	<0.01	21/8	<0.01	13/8	0.13	57/8	<0.01	10/8	0.28
$p_{\mathrm{T}}^{\mathrm{d},*}$	21/9	0.01	6/9	0.78	10/9	0.35	35/9	<0.01	8/9	0.54
LHA	12/12	0.49	9/12	0.74	12/12	0.46	12/12	0.43	11/12	0.53
D_2 vs. m^{top}	22/32	0.91	27/32	0.73	20/32	0.95	28/32	0.67	19/32	0.96
D_2 vs. $p_{\mathrm{T}}^{\mathrm{top}}$	29/43	0.96	26/43	0.98	28/43	0.96	32/43	0.88	26/43	0.98
τ_{32} vs. m^{top}	30/27	0.31	21/27	0.79	15/27	0.97	69/27	<0.01	11/27	1.00
τ_{32} vs. $p_{\mathrm{T}}^{\mathrm{top}}$	49/37	0.08	36/37	0.53	34/37	0.63	94/37	<0.01	30/37	0.79

investigate the substructure of top-quark jets with variables defined using only charged components of the jet. Compared to previous ATLAS measurements of top-quark-jet substructure, this approach, together with the larger dataset analyzed, significantly reduces the uncertainties in the measured quantities. These smaller uncertainties provide greater sensitivity to the differences between the various MC predictions. Both single-differential cross-section measurements and a selected set of double-differential cross-section measurements are presented.

The observed substructure distributions are compared with several MC generator predictions, which are all based on NLO calculations for the matrix element, LO calculations for the decay of the top quark, and phenomenological models for parton showering and hadronization. A quantitative comparison between the observed and predicted distributions shows that the τ_{21}, ECF2 and D_2 variables are generally well described in both channels by the POWHEG+PYTHIA8 MC predictions, which were used as the nominal predictions in the analysis. In contrast, the distributions of τ_{32}, τ_3, and C_3 are poorly described by the nominal MC predictions, with the predicted jet substructure being more three-body-like than that observed. These observations are consistent between the two channels. The distribution of p_{T} dispersion, $p_{\mathrm{T}}^{\mathrm{d},*}$, is not well modeled by the nominal MC prediction, with the observed distributions being more strongly peaked at lower values.

Most of these features are also reflected in the alternative MC predictions. Generally speaking, the MC predictions from the HERWIG 7 parton-shower and hadronization model are a better match to the observed distributions, although the distributions of τ_{32}, τ_3, and C_3 are poorly described. The alternative matrix-element predictions from AMC@NLO +PYTHIA8 are in better agreement with the observed distributions in both channels. The predictions made with increased FSR scales are universally poorer descriptions of the data, while for most of the substructure variables the models with decreased FSR scales are generally in better agreement than the nominal predictions, indicating that the data favor an increased value of $\alpha_{\mathrm{s}}^{\mathrm{FSR}}$. In general, the predictions are in better agreement with the measurements in the all-hadronic channel.

The τ_{32} and D_2 variables, which are sensitive to three-body and two-body modeling, have correlations with m^{top} and $p_{\mathrm{T}}^{\mathrm{top}}$ that are poorly modeled by several NLOME + PS calculations, indicating systematic problems in these calculations at low m^{top} and high $p_{\mathrm{T}}^{\mathrm{top}}$.

These observations illustrate that the HERWIG 7 model for parton showering and hadronization is a better match to the observed substructure than the PYTHIA 8 model. In addition, the models with increased $\alpha_{\mathrm{s}}^{\mathrm{FSR}}$ predict jet substructure that is in better agreement with the observations. These observations are consistent with the results of comparisons with the top-quark-jet kinematics observed in the all-hadronic final state, and reinforce the need to improve the models used to predict the substructure of boosted top-quark jets.

ACKNOWLEDGMENTS

We thank CERN for the very successful operation of the LHC, as well as the support staff from our institutions without whom ATLAS could not be operated efficiently. We acknowledge the support of ANPCyT, Argentina; YerPhI, Armenia; ARC, Australia; BMWFW and FWF, Austria; ANAS, Azerbaijan; CNPq and FAPESP, Brazil; NSERC, NRC and CFI, Canada; CERN; ANID, Chile; CAS, MOST and NSFC, China; Minciencias, Colombia; MEYS CR, Czech Republic; DNRF and DNSRC, Denmark; IN2P3-CNRS and CEA-DRF/IRFU, France; SRNSFG, Georgia; BMBF, HGF and MPG, Germany; GSRI, Greece; RGC and Hong Kong SAR, China; ISF and Benoziyo Center, Israel; INFN, Italy; MEXT and JSPS, Japan; CNRST, Morocco; NWO, Netherlands; RCN, Norway; MEiN, Poland; FCT, Portugal; MNE/IFA, Romania; MESTD, Serbia; MSSR, Slovakia; ARRS and MIZŠ, Slovenia; DSI/NRF, South Africa; MICINN, Spain; SRC and Wallenberg Foundation, Sweden; SERI, SNSF and Cantons of Bern and Geneva, Switzerland; MOST, Taiwan; TENMAK, Türkiye; STFC, United Kingdom; DOE and NSF, United States of America. In addition, individual groups and members have received support from BCKDF, CANARIE, Compute Canada and CRC, Canada; PRIMUS 21/SCI/017 and UNCE SCI/013, Czech Republic; COST, ERC, ERDF, Horizon 2020 and Marie Skłodowska-Curie Actions, European Union; Investissements d'Avenir Labex, Investissements d'Avenir Idex and ANR, France; DFG and AvH Foundation, Germany; Herakleitos, Thales and Aristeia programmes co-financed by EU-ESF and the Greek NSRF, Greece; BSF-NSF and MINERVA, Israel; Norwegian Financial Mechanism 2014-2021, Norway; NCN and NAWA, Poland; La Caixa Banking Foundation, CERCA Programme Generalitat de Catalunya and PROMETEO and GenT Programmes Generalitat Valenciana, Spain; Göran Gustafssons Stiftelse, Sweden; The Royal Society and Leverhulme Trust, United Kingdom. The crucial computing support from all WLCG partners is acknowledged gratefully, in particular from CERN, the ATLAS Tier-1 facilities at TRIUMF (Canada), NDGF (Denmark, Norway, Sweden), CC-IN2P3 (France), KIT/GridKA (Germany), INFN-CNAF (Italy), NL-T1 (Netherlands), PIC (Spain), ASGC (Taiwan), RAL (UK) and BNL (USA), the Tier-2 facilities worldwide and large non-WLCG resource providers. Major contributors of computing resources are listed in Ref. [154].

[1] ATLAS Collaboration, Inclusive and differential cross sections for dilepton $t\bar{t}$ production measured in $\sqrt{s} = 13$ TeV pp collisions with the ATLAS detector, J. High Energy Phys. 07 (2023) 141.

[2] ATLAS Collaboration, Measurements of differential cross sections in top-quark pair events with a high transverse momentum top quark and limits on beyond the Standard Model contributions to top-quark pair production with the ATLAS detector at $\sqrt{s} = 13$ TeV, J. High Energy Phys. 06 (2022) 063.

[3] CMS Collaboration, Measurement of differential $t\bar{t}$ production cross sections in the full kinematic range using lepton + jets events from proton-proton collisions at $\sqrt{s} = 13$ TeV, Phys. Rev. D **104**, 092013 (2021).

[4] CMS Collaboration, Measurement of $t\bar{t}$ normalised multi-differential cross sections in pp collisions at $\sqrt{s} = 13$ TeV, and simultaneous determination of the strong coupling strength, top quark pole mass, and parton distribution functions, Eur. Phys. J. C **80**, 658 (2020).

[5] R. Kogler *et al.*, Jet substructure at the large hadron collider, Rev. Mod. Phys. **91**, 045003 (2019).

[6] A. J. Larkoski, I. Moult, and B. Nachman, Jet substructure at the Large Hadron Collider: A review of recent advances in theory and machine learning, Phys. Rep. **841**, 1 (2020).

[7] ATLAS Collaboration, Search for heavy particles decaying into top-quark pairs using lepton-plus-jets events in proton-proton collisions at $\sqrt{s} = 13$ TeV with the ATLAS detector, Eur. Phys. J. C **78**, 565 (2018).

[8] ATLAS Collaboration, Search for supersymmetry in final states with missing transverse momentum and multiple b-jets in proton-proton collisions at $\sqrt{s} = 13$ TeV with the ATLAS detector, J. High Energy Phys. 06 (2018) 107.

[9] ATLAS Collaboration, Search for dark matter produced in association with a Higgs boson decaying to $b\bar{b}$ using 36 fb^{-1} of pp collisions at $\sqrt{s} = 13$ TeV with the ATLAS detector, Phys. Rev. Lett. **119**, 181804 (2017).

[10] ATLAS Collaboration, Search for chargino and neutralino production in final states with a Higgs boson and missing transverse momentum at $\sqrt{s} = 13$ TeV with the ATLAS detector, Phys. Rev. D **100**, 012006 (2019).

[11] ATLAS Collaboration, Search for diboson resonances in hadronic final states in 139 fb^{-1} of pp collisions at $\sqrt{s} = 13$ TeV with the ATLAS detector, J. High Energy Phys. 09 (2019) 091.

[12] ATLAS Collaboration, Performance of top-quark and W-boson tagging with ATLAS in Run 2 of the LHC, Eur. Phys. J. C **79**, 375 (2019).

[13] CMS Collaboration, Identification of heavy, energetic, hadronically decaying particles using machine-learning techniques, J. Instrum. **15**, P06005 (2020).

[14] G. Kasieczka *et al.*, The machine learning landscape of top taggers, SciPost Phys. **7**, 014 (2019).

[15] ATLAS Collaboration, Differential $t\bar{t}$ cross-section measurements using boosted top quarks in the all-hadronic final state with 139 fb^{-1} of ATLAS data, J. High Energy Phys. 04 (2023) 080.

[16] ATLAS Collaboration, Search for dark matter produced in association with a single top quark and an energetic W boson in $\sqrt{s} = 13$ TeV pp collisions with the ATLAS detector, Eur. Phys. J. C **83**, 603 (2023).

[17] ATLAS Collaboration, Measurement of the energy asymmetry in $t\bar{t}j$ production at 13 TeV with the ATLAS experiment and interpretation in the SMEFT framework, Eur. Phys. J. C **82**, 374 (2022).

[18] ATLAS Collaboration, Search for $t\bar{t}$ resonances in fully hadronic final states in pp collisions at $\sqrt{s} = 13$ TeV with the ATLAS detector, J. High Energy Phys. 10 (2020) 061.

[19] CMS Collaboration, Search for $t\bar{t}$ resonances in highly-boosted lepton + jets and fully hadronic final states in proton-proton collisions at $\sqrt{s} = 13$ TeV, J. High Energy Phys. 07 (2017) 001.

[20] CMS Collaboration, Search for resonant $t\bar{t}$ production in proton-proton collisions at $\sqrt{s} = 13$ TeV, J. High Energy Phys. 04 (2019) 031.

[21] G. P. Salam, Towards Jetography, Eur. Phys. J. C **67**, 637 (2010).

[22] ATLAS Collaboration, Jet mass and substructure of inclusive jets in $\sqrt{s} = 7$ TeV pp collisions with the ATLAS experiment, J. High Energy Phys. 05 (2012) 128.

[23] ATLAS Collaboration, Measurement of jet charge in dijet events from $\sqrt{s} = 8$ TeV pp collisions with the ATLAS detector, Phys. Rev. D **93**, 052003 (2016).

[24] ATLAS Collaboration, Measurement of soft-drop jet observables in pp collisions with the ATLAS detector at $\sqrt{s} = 13$ TeV, Phys. Rev. D **101**, 052007 (2020).

[25] CMS Collaboration, Shape, transverse size, and charged hadron multiplicity of jets in pp collisions at $\sqrt{s} = 7$ TeV, J. High Energy Phys. 06 (2012) 160.

[26] CMS Collaboration, Measurements of jet charge with dijet events in pp collisions at $\sqrt{s} = 8$ TeV, J. High Energy Phys. 10 (2017) 131.

[27] CMS Collaboration, Measurements of the differential jet cross section as a function of the jet mass in dijet events from proton-proton collisions at $\sqrt{s} = 13$ TeV, J. High Energy Phys. 11 (2018) 113.

[28] CMS Collaboration, Study of quark and gluon jet substructure in Z + jet and dijet events from pp collisions, J. High Energy Phys. 01 (2022) 188.

[29] CMS Collaboration, Measurement of the splitting function in pp and PbPb collisions at $\sqrt{s_{\mathrm{NN}}} = 5.02$ TeV, Phys. Rev. Lett. **120**, 142302 (2018).

[30] CMS Collaboration, Studies of jet mass in dijet and W/Z + jet events, J. High Energy Phys. 05 (2013) 090.

[31] ALICE Collaboration, Exploration of jet substructure using iterative declustering in pp and Pb-Pb collisions at LHC energies, Phys. Lett. B **802**, 135227 (2020).

[32] ALICE Collaboration, First measurements of N-subjettiness in central Pb-Pb collisions at $\sqrt{s_{\mathrm{NN}}} = 2.76$ TeV, J. High Energy Phys. 10 (2021) 003.

[33] ALICE Collaboration, Measurement of the groomed jet radius and momentum splitting fraction in pp and Pb − Pb collisions at $\sqrt{s_{NN}} = 5.02$ TeV, Phys. Rev. Lett. **128**, 102001 (2022).

[34] ALICE Collaboration, Direct observation of the dead-cone effect in quantum chromodynamics, Nature (London) **605**, 440 (2022); **607**, E22 (2022).

[35] LHCb Collaboration, Study of J/ψ production in jets, Phys. Rev. Lett. **118**, 192001 (2017).

[36] ATLAS Collaboration, Measurement of the soft-drop jet mass in pp collisions at $\sqrt{s} = 13$ TeV with the ATLAS detector, Phys. Rev. Lett. **121**, 092001 (2018).

[37] ATLAS Collaboration, ATLAS measurements of the properties of jets for boosted particle searches, Phys. Rev. D **86**, 072006 (2012).

[38] ATLAS Collaboration, Measurement of the lund jet plane using charged particles in 13 TeV proton-proton collisions with the ATLAS detector, Phys. Rev. Lett. **124**, 222002 (2020).

[39] CDF Collaboration, Studies of high-transverse momentum jet substructure and top quarks produced in 1.96 TeV proton-antiproton collisions, Phys. Rev. D **91**, 032006 (2015).

[40] ATLAS Collaboration, Measurement of colour flow with the jet pull angle in $t\bar{t}$ events using the ATLAS detector at $\sqrt{s} = 8$ TeV, Phys. Lett. B **750**, 475 (2015).

[41] ATLAS Collaboration, Measurement of colour flow using jet-pull observables in $t\bar{t}$ events with the ATLAS experiment at $\sqrt{s} = 13$ TeV, Eur. Phys. J. C **78**, 847 (2018).

[42] ATLAS Collaboration, Measurement of jet-substructure observables in top quark, W boson and light jet production in proton-proton collisions at $\sqrt{s} = 13$ TeV with the ATLAS detector, J. High Energy Phys. 08 (2019) 033.

[43] CMS Collaboration, Measurement of jet substructure observables in $t\bar{t}$ events from proton-proton collisions at $\sqrt{s} = 13$ TeV, Phys. Rev. D **98**, 092014 (2018).

[44] LHCb Collaboration, Measurement of charged hadron production in Z-tagged jets in proton-proton collisions at $\sqrt{s} = 8$ TeV, Phys. Rev. Lett. **123**, 232001 (2019).

[45] CMS Collaboration, Measurement of the jet mass distribution and top quark mass in hadronic decays of boosted top quarks in pp collisions at $\sqrt{s} = 13$ TeV, Phys. Rev. Lett. **124**, 202001 (2020).

[46] CMS Collaboration, Measurement of the jet mass in highly boosted $t\bar{t}$ events from pp collisions at $\sqrt{s} = 8$ TeV, Eur. Phys. J. C **77**, 467 (2017).

[47] J. Thaler and K. Van Tilburg, Identifying boosted objects with N-subjettiness, J. High Energy Phys. 03 (2011) 015.

[48] J. Thaler and K. Van Tilburg, Maximizing boosted top identification by minimizing N-subjettiness, J. High Energy Phys. 02 (2012) 093.

[49] A. J. Larkoski, G. P. Salam, and J. Thaler, Energy correlation functions for jet substructure, J. High Energy Phys. 06 (2013) 108.

[50] A. J. Larkoski, I. Moult, and D. Neill, Power counting to better jet observables, J. High Energy Phys. 12 (2014) 009.

[51] A. J. Larkoski, J. Thaler, and W. J. Waalewijn, Gaining (mutual) information about quark/gluon discrimination, J. High Energy Phys. 11 (2014) 129.

[52] ATLAS Collaboration, The ATLAS experiment at the CERN large hadron collider, J. Instrum. **3**, S08003 (2008).

[53] ATLAS Collaboration, Performance of the ATLAS trigger system in 2015, Eur. Phys. J. C **77**, 317 (2017).

[54] ATLAS Collaboration, The ATLAS Collaboration Software and Firmware, ATL-SOFT-PUB-2021-001, 2021, https://cds.cern.ch/record/2767187.

[55] ATLAS Collaboration, ATLAS data quality operations and performance for 2015–2018 data-taking, J. Instrum. **15**, P04003 (2020).

[56] ATLAS Collaboration, Luminosity determination in pp collisions at $\sqrt{s} = 13$ TeV using the ATLAS detector at the LHC, Eur. Phys. J. C **83**, 982 (2023).

[57] G. Avoni *et al.*, The new LUCID-2 detector for luminosity measurement and monitoring in ATLAS, J. Instrum. **13**, P07017 (2018).

[58] ATLAS Collaboration, Performance of electron and photon triggers in ATLAS during LHC Run 2, Eur. Phys. J. C **80**, 47 (2020).

[59] ATLAS Collaboration, Performance of the ATLAS muon triggers in Run 2, J. Instrum. **15**, P09015 (2020).

[60] D. Krohn, J. Thaler, and L.-T. Wang, Jet trimming, J. High Energy Phys. 02 (2010) 084.

[61] ATLAS Collaboration, The ATLAS simulation infrastructure, Eur. Phys. J. C **70**, 823 (2010).

[62] S. Agostinelli *et al.*, GEANT4—a simulation toolkit, Nucl. Instrum. Methods Phys. Res., Sect. A **506**, 250 (2003).

[63] ATLAS Collaboration, The simulation principle and performance of the ATLAS fast calorimeter simulation FastCaloSim, ATL-PHYS-PUB-2010-013, 2010, https://cds.cern.ch/record/1300517.

[64] S. Frixione, G. Ridolfi, and P. Nason, A positive-weight next-to-leading-order Monte Carlo for heavy flavour hadroproduction, J. High Energy Phys. 09 (2007) 126.

[65] P. Nason, A new method for combining NLO QCD with shower Monte Carlo algorithms, J. High Energy Phys. 11 (2004) 040.

[66] S. Frixione, P. Nason, and C. Oleari, Matching NLO QCD computations with parton shower simulations: The POWHEG method, J. High Energy Phys. 11 (2007) 070.

[67] S. Alioli, P. Nason, C. Oleari, and E. Re, A general framework for implementing NLO calculations in shower Monte Carlo programs: The POWHEG BOX, J. High Energy Phys. 06 (2010) 043.

[68] R. D. Ball *et al.* (The NNPDF Collaboration), Parton distributions for the LHC run II, J. High Energy Phys. 04 (2015) 040.

[69] ATLAS Collaboration, Studies on top-quark Monte Carlo modelling for Top2016, ATL-PHYS-PUB-2016-020, 2016, https://cds.cern.ch/record/2216168.

[70] T. Sjöstrand *et al.*, An introduction to PYTHIA 8.2, Comput. Phys. Commun. **191**, 159 (2015).

[71] ATLAS Collaboration, ATLAS Pythia 8 tunes to 7 TeV data, ATL-PHYS-PUB-2014-021, 2014, https://cds.cern.ch/record/1966419.

[72] R. D. Ball *et al.* (NNPDF Collaboration), Parton distributions with LHC data, Nucl. Phys. **B867**, 244 (2013).

[73] M. Bähr *et al.*, Herwig++ physics and manual, Eur. Phys. J. C **58**, 639 (2008).

[74] J. Bellm *et al.*, Herwig 7.0/Herwig ++3.0 release note, Eur. Phys. J. C **76**, 196 (2016).

[75] J. Bellm *et al.*, HERWIG7.1 Release Note, arXiv:1705.06919.

[76] L. A. Harland-Lang, A. D. Martin, P. Motylinski, and R. S. Thorne, Parton distributions in the LHC era: MMHT 2014 PDFs, Eur. Phys. J. C **75**, 204 (2015).

[77] J. Alwall *et al.*, The automated computation of tree-level and next-to-leading order differential cross sections, and their matching to parton shower simulations, J. High Energy Phys. 07 (2014) 079.

[78] S. Frixione, E. Laenen, P. Motylinski, and B. R. Webber, Angular correlations of lepton pairs from vector boson and top quark decays in Monte Carlo simulations, J. High Energy Phys. 04 (2007) 081.
[79] P. Artoisenet, R. Frederix, O. Mattelaer, and R. Rietkerk, Automatic spin-entangled decays of heavy resonances in Monte Carlo simulations, J. High Energy Phys. 03 (2013) 015.
[80] ATLAS Collaboration, Studies on top-quark Monte Carlo modelling with Sherpa and MG5_aMC@NLO, ATL-PHYS-PUB-2017-007, 2017, https://cds.cern.ch/record/2261938.
[81] M. Beneke, P. Falgari, S. Klein, and C. Schwinn, Hadronic top-quark pair production with NNLL threshold resummation, Nucl. Phys. **B855**, 695 (2012).
[82] M. Cacciari, M. Czakon, M. Mangano, A. Mitov, and P. Nason, Top-pair production at hadron colliders with next-to-next-to-leading logarithmic soft-gluon resummation, Phys. Lett. B **710**, 612 (2012).
[83] P. Bärnreuther, M. Czakon, and A. Mitov, Percent-level-precision physics at the tevatron: Next-to-next-to-leading order QCD corrections to $q\bar{q} \to t\bar{t} + X$, Phys. Rev. Lett. **109**, 132001 (2012).
[84] M. Czakon and A. Mitov, NNLO corrections to top-pair production at hadron colliders: The all-fermionic scattering channels, J. High Energy Phys. 12 (2012) 054.
[85] M. Czakon and A. Mitov, NNLO corrections to top pair production at hadron colliders: The quark-gluon reaction, J. High Energy Phys. 01 (2013) 080.
[86] M. Czakon, P. Fiedler, and A. Mitov, Total top-quark pair-production cross section at hadron colliders through $O(\alpha_S^4)$, Phys. Rev. Lett. **110**, 252004 (2013).
[87] M. Czakon and A. Mitov, Top ++: A program for the calculation of the top-pair cross section at hadron colliders, Comput. Phys. Commun. **185**, 2930 (2014).
[88] J. Butterworth *et al.*, PDF4LHC recommendations for LHC Run II, J. Phys. G **43**, 023001 (2016).
[89] A. D. Martin, W. J. Stirling, R. S. Thorne, and G. Watt, Parton distributions for the LHC, Eur. Phys. J. C **63**, 189 (2009).
[90] A. D. Martin, W. J. Stirling, R. S. Thorne, and G. Watt, Uncertainties on α_S in global PDF analyses and implications for predicted hadronic cross sections, Eur. Phys. J. C **64**, 653 (2009).
[91] H.-L. Lai *et al.*, New parton distributions for collider physics, Phys. Rev. D **82**, 074024 (2010).
[92] J. Gao *et al.*, CT10 next-to-next-to-leading order global analysis of QCD, Phys. Rev. D **89**, 033009 (2014).
[93] E. Re, Single-top Wt-channel production matched with parton showers using the POWHEG method, Eur. Phys. J. C **71**, 1547 (2011).
[94] S. Frixione, E. Laenen, P. Motylinski, C. White, and B. R. Webber, Single-top hadroproduction in association with a W boson, J. High Energy Phys. 07 (2008) 029.
[95] E. Bothmann *et al.*, Event generation with Sherpa 2.2, SciPost Phys. **7**, 034 (2019).
[96] T. Gleisberg and S. Höche, Comix, a new matrix element generator, J. High Energy Phys. 12 (2008) 039.
[97] F. Buccioni *et al.*, OpenLoops 2, Eur. Phys. J. C **79**, 866 (2019).
[98] F. Cascioli, P. Maierhöfer, and S. Pozzorini, Scattering amplitudes with open loops, Phys. Rev. Lett. **108**, 111601 (2012).
[99] A. Denner, S. Dittmaier, and L. Hofer, Collier: A Fortran-based complex one-loop library in extended regularizations, Comput. Phys. Commun. **212**, 220 (2017).
[100] S. Schumann and F. Krauss, A parton shower algorithm based on Catani–Seymour dipole factorisation, J. High Energy Phys. 03 (2008) 038.
[101] S. Höche, F. Krauss, M. Schönherr, and F. Siegert, A critical appraisal of NLO + PS matching methods, J. High Energy Phys. 09 (2012) 049.
[102] S. Höche, F. Krauss, M. Schönherr, and F. Siegert, QCD matrix elements + parton showers. The NLO case, J. High Energy Phys. 04 (2013) 027.
[103] S. Catani, F. Krauss, B. R. Webber, and R. Kuhn, QCD matrix elements + parton showers, J. High Energy Phys. 11 (2001) 063.
[104] S. Höche, F. Krauss, S. Schumann, and F. Siegert, QCD matrix elements and truncated showers, J. High Energy Phys. 05 (2009) 053.
[105] C. Anastasiou, L. Dixon, K. Melnikov, and F. Petriello, High-precision QCD at hadron colliders: Electroweak gauge boson rapidity distributions at next-to-next-to leading order, Phys. Rev. D **69**, 094008 (2004).
[106] H. B. Hartanto, B. Jäger, L. Reina, and D. Wackeroth, Higgs boson production in association with top quarks in the POWHEG BOX, Phys. Rev. D **91**, 094003 (2015).
[107] D. J. Lange, The EvtGen particle decay simulation package, Nucl. Instrum. Methods Phys. Res., Sect. A **462**, 152 (2001).
[108] ATLAS Collaboration, The Pythia 8 A3 tune description of ATLAS minimum bias and inelastic measurements incorporating the Donnachie–Landshoff diffractive model, ATL-PHYS-PUB-2016-017, 2016, https://cds.cern.ch/record/2206965.
[109] ATLAS Collaboration, Topological cell clustering in the ATLAS calorimeters and its performance in LHC Run 1, Eur. Phys. J. C **77**, 490 (2017).
[110] M. Cacciari, G. P. Salam, and G. Soyez, The anti-k_t jet clustering algorithm, J. High Energy Phys. 04 (2008) 063.
[111] M. Cacciari, G. P. Salam, and G. Soyez, FASTJET user manual, Eur. Phys. J. C **72**, 1896 (2012).
[112] ATLAS Collaboration, Jet reconstruction and performance using particle flow with the ATLAS detector, Eur. Phys. J. C **77**, 466 (2017).
[113] B. Nachman, P. Nef, A. Schwartzman, M. Swiatlowski, and C. Wanotayaroj, Jets from Jets: Re-clustering as a tool for large radius jet reconstruction and grooming at the LHC, J. High Energy Phys. 02 (2015) 075.
[114] D. Krohn, J. Thaler, and L.-T. Wang, Jets with variable R, J. High Energy Phys. 06 (2009) 059.
[115] ATLAS Collaboration, Identification of boosted Higgs bosons decaying into $b\bar{b}$ with neural networks and variable radius subjets in ATLAS, ATL-PHYS-PUB-2020-019, 2020, https://cds.cern.ch/record/2724739.
[116] ATLAS Collaboration, Performance of pile-up mitigation techniques for jets in pp collisions at $\sqrt{s} = 8$ TeV using the ATLAS detector, Eur. Phys. J. C **76**, 581 (2016).

[117] ATLAS Collaboration, Jet energy scale and resolution measured in proton-proton collisions at $\sqrt{s} = 13$ TeV with the ATLAS detector, Eur. Phys. J. C **81**, 689 (2020).
[118] ATLAS Collaboration, In situ calibration of large-radius jet energy and mass in 13 TeV proton-proton collisions with the ATLAS detector, Eur. Phys. J. C **79**, 135 (2019).
[119] ATLAS Collaboration, Jet reclustering and close-by effects in ATLAS Run 2, ATLAS-CONF-2017-062, 2017, https://cds.cern.ch/record/2275649.
[120] ATLAS Collaboration, ATLAS flavour-tagging algorithms for the LHC Run 2pp collision dataset, Eur. Phys. J. C **83**, 681 (2023).
[121] ATLAS Collaboration, ATLAS b-jet identification performance and efficiency measurement with $t\bar{t}$ events in pp collisions at $\sqrt{s} = 13$ TeV, Eur. Phys. J. C **79**, 970 (2019).
[122] ATLAS Collaboration, Optimisation and performance studies of the ATLAS b-tagging algorithms for the 2017-18 LHC run, ATL-PHYS-PUB-2017-013, 2017, https://cds.cern.ch/record/2273281.
[123] M. Cacciari, G. P. Salam, and G. Soyez, The catchment area of jets, J. High Energy Phys. 04 (2008) 005.
[124] M. Cacciari and G. P. Salam, Pileup subtraction using jet areas, Phys. Lett. B **659**, 119 (2008).
[125] ATLAS Collaboration, Boosted hadronic vector boson and top quark tagging with ATLAS using Run 2 data, ATL-PHYS-PUB-2020-017, 2020, https://cds.cern.ch/record/2724149.
[126] ATLAS Collaboration, Performance of the ATLAS track reconstruction algorithms in dense environments in LHC Run 2, Eur. Phys. J. C **77**, 673 (2017).
[127] ATLAS Collaboration, Electron reconstruction and identification in the ATLAS experiment using the 2015 and 2016 LHC proton-proton collision data at $\sqrt{s} = 13$ TeV, Eur. Phys. J. C **79**, 639 (2019).
[128] ATLAS Collaboration, Electron and photon performance measurements with the ATLAS detector using the 2015–2017 LHC proton-proton collision data, J. Instrum. **14**, P12006 (2019).
[129] ATLAS Collaboration, Muon reconstruction and identification efficiency in ATLAS using the full Run 2pp collision data set at $\sqrt{s} = 13$ TeV, Eur. Phys. J. C **81**, 578 (2021).
[130] ATLAS Collaboration, Performance of missing transverse momentum reconstruction with the ATLAS detector using proton-proton collisions at $\sqrt{s} = 13$ TeV, Eur. Phys. J. C **78**, 903 (2018).
[131] ATLAS Collaboration, Estimation of non-prompt and fake lepton backgrounds in final states with top quarks produced in proton-proton collisions at $\sqrt{s} = 8$ TeV with the ATLAS detector, ATLAS-CONF-2014-058, 2014, https://cds.cern.ch/record/1951336.
[132] ATLAS Collaboration, Measurements of $t\bar{t}$ differential cross sections of highly boosted top quarks decaying to all-hadronic final states in pp collisions at $\sqrt{s} = 13$ TeV using the ATLAS detector, Phys. Rev. D **98**, 012003 (2018).
[133] ATLAS Collaboration, Measurements of top-quark pair differential and double-differential cross sections in the ℓ + jets channel with pp collisions at $\sqrt{s} = 13$ TeV using the ATLAS detector, Eur. Phys. J. C **79**, 1028 (2019); **80**, 1092(E) (2020).
[134] ATLAS Collaboration, Measurements of top-quark pair differential cross sections in the lepton + jets channel in pp collisions at $\sqrt{s} = 13$ TeV using the ATLAS detector, J. High Energy Phys. 11 (2017) 191.
[135] ATLAS Collaboration, Measurement of the differential cross section of highly boosted top quarks as a function of their transverse momentum in $\sqrt{s} = 8$ TeV proton-proton collisions using the ATLAS detector, Phys. Rev. D **93**, 032009 (2016).
[136] CMS Collaboration, Measurement of differential $t\bar{t}$ production cross sections using top quarks at large transverse momenta in pp collisions at $\sqrt{s} = 13$ TeV, Phys. Rev. D **103**, 052008 (2021).
[137] A. J. Larkoski, I. Moult, and D. Neill, Analytic boosted boson discrimination, J. High Energy Phys. 05 (2016) 117.
[138] S. D. Ellis and D. E. Soper, Successive combination jet algorithm for hadron collisions, Phys. Rev. D **48**, 3160 (1993).
[139] G. D'Agostini, A multidimensional unfolding method based on Bayes' theorem, Nucl. Instrum. Methods Phys. Res., Sect. A **362**, 487 (1995).
[140] T. Adye, Unfolding algorithms and tests using RooUnfold, *Proceedings, 2011 Workshop on Statistical Issues Related to Discovery Claims in Search Experiments and Unfolding (PHYSTAT 2011)* (CERN, Geneva, Switzerland, 2011), 313, arXiv:1105.1160.
[141] ATLAS Collaboration, Measurement of the ATLAS detector jet mass response using forward folding with 80 fb^{-1} of $\sqrt{s} = 13$ TeV pp data, ATLAS-CONF-2020-022, 2020, https://cds.cern.ch/record/2724442.
[142] ATLAS Collaboration, Simulation-based extrapolation of b-tagging calibrations towards high transverse momenta in the ATLAS experiment, ATL-PHYS-PUB-2021-003, 2021, https://cds.cern.ch/record/2753444.
[143] ATLAS Collaboration, Early inner detector tracking performance in the 2015 data at $\sqrt{s} = 13$ TeV, ATL-PHYS-PUB-2015-051, 2015, https://cds.cern.ch/record/2110140.
[144] N. Kidonakis, Next-to-next-to-leading logarithm resummation for s-channel single top quark production, Phys. Rev. D **81**, 054028 (2010).
[145] N. Kidonakis, Next-to-next-to-next-to-leading-order soft-gluon corrections in hard-scattering processes near threshold, Phys. Rev. D **73**, 034001 (2006).
[146] ATLAS Collaboration, ATLAS simulation of boson plus jets processes in Run 2, ATL-PHYS-PUB-2017-006, 2017, https://cds.cern.ch/record/2261937.
[147] D. de Florian *et al.*, *Handbook of LHC Higgs Cross Sections: 4. Deciphering the Nature of the Higgs Sector* (CERN, Geneva, 2017).
[148] ATLAS Collaboration, Study of top-quark pair modelling and uncertainties using ATLAS measurements at $\sqrt{s} =$ 13 TeV, ATL-PHYS-PUB-2020-023, 2020, https://cds.cern.ch/record/2730443.
[149] ATLAS Collaboration, Measurement of the top quark mass in the $t\bar{t} \to$ lepton + jets channel from $\sqrt{s} = 8$ TeV

ATLAS data and combination with previous results, Eur. Phys. J. C **79**, 290 (2019).
[150] CMS Collaboration, Measurement of the top quark mass using proton-proton data at $\sqrt{s} = 7$ and 8 TeV, Phys. Rev. D **93**, 072004 (2016).
[151] ATLAS Collaboration, Measurements of top-quark pair differential cross sections in the lepton + jets channel in pp collisions at $\sqrt{s} = 8$ TeV using the ATLAS detector, Eur. Phys. J. C **76**, 538 (2016).
[152] D. Kar and P. Sarmah, Effect of new jet substructure measurements on PYTHIA8 tunes, arXiv:2101.11395.
[153] CMS Collaboration, Measurement of the jet mass distribution and top quark mass in hadronic decays of boosted top quarks in proton-proton collisions at $\sqrt{s} = 13$ TeV, Eur. Phys. J. C **83**, 560 (2023).
[154] ATLAS Collaboration, ATLAS computing acknowledgements, ATL-SOFT-PUB-2021-003, 2021, https://cds.cern.ch/record/2776662.

G. Aad,[102] B. Abbott,[120] K. Abeling,[55] N. J. Abicht,[49] S. H. Abidi,[29] A. Aboulhorma,[35e] H. Abramowicz,[151] H. Abreu,[150] Y. Abulaiti,[117] A. C. Abusleme Hoffman,[137a] B. S. Acharya,[69a,69b,b] C. Adam Bourdarios,[4] L. Adamczyk,[86a] L. Adamek,[155] S. V. Addepalli,[26] M. J. Addison,[101] J. Adelman,[115] A. Adiguzel,[21c] T. Adye,[134] A. A. Affolder,[136] Y. Afik,[36] M. N. Agaras,[13] J. Agarwala,[73a,73b] A. Aggarwal,[100] C. Agheorghiesei,[27c] A. Ahmad,[36] F. Ahmadov,[38,c] W. S. Ahmed,[104] S. Ahuja,[95] X. Ai,[62a] G. Aielli,[76a,76b] A. Aikot,[163] M. Ait Tamlihat,[35e] B. Aitbenchikh,[35a] I. Aizenberg,[169] M. Akbiyik,[100] T. P. A. Åkesson,[98] A. V. Akimov,[37] D. Akiyama,[168] N. N. Akolkar,[24] K. Al Khoury,[41] G. L. Alberghi,[23b] J. Albert,[165] P. Albicocco,[53] G. L. Albouy,[60] S. Alderweireldt,[52] M. Aleksa,[36] I. N. Aleksandrov,[38] C. Alexa,[27b] T. Alexopoulos,[10] F. Alfonsi,[23b] M. Algren,[56] M. Alhroob,[120] B. Ali,[132] H. M. J. Ali,[91] S. Ali,[148] S. W. Alibocus,[92] M. Aliev,[145] G. Alimonti,[71a] W. Alkakhi,[55] C. Allaire,[66] B. M. M. Allbrooke,[146] J. F. Allen,[52] C. A. Allendes Flores,[137f] P. P. Allport,[20] A. Aloisio,[72a,72b] F. Alonso,[90] C. Alpigiani,[138] M. Alvarez Estevez,[99] A. Alvarez Fernandez,[100] M. Alves Cardoso,[56] M. G. Alviggi,[72a,72b] M. Aly,[101] Y. Amaral Coutinho,[83b] A. Ambler,[104] C. Amelung,[36] M. Amerl,[101] C. G. Ames,[109] D. Amidei,[106] S. P. Amor Dos Santos,[130a] K. R. Amos,[163] V. Ananiev,[125] C. Anastopoulos,[139] T. Andeen,[11] J. K. Anders,[36] S. Y. Andrean,[47a,47b] A. Andreazza,[71a,71b] S. Angelidakis,[9] A. Angerami,[41,d] A. V. Anisenkov,[37] A. Annovi,[74a] C. Antel,[56] M. T. Anthony,[139] E. Antipov,[145] M. Antonelli,[53] F. Anulli,[75a] M. Aoki,[84] T. Aoki,[153] J. A. Aparisi Pozo,[163] M. A. Aparo,[146] L. Aperio Bella,[48] C. Appelt,[18] A. Apyan,[26] N. Aranzabal,[36] C. Arcangeletti,[53] A. T. H. Arce,[51] E. Arena,[92] J-F. Arguin,[108] S. Argyropoulos,[54] J.-H. Arling,[48] O. Arnaez,[4] H. Arnold,[114] G. Artoni,[75a,75b] H. Asada,[111] K. Asai,[118] S. Asai,[153] N. A. Asbah,[61] K. Assamagan,[29] R. Astalos,[28a] S. Atashi,[160] R. J. Atkin,[33a] M. Atkinson,[162] H. Atmani,[35f] P. A. Atmasiddha,[106] K. Augsten,[132] S. Auricchio,[72a,72b] A. D. Auriol,[20] V. A. Austrup,[101] G. Avolio,[36] K. Axiotis,[56] G. Azuelos,[108,e] D. Babal,[28b] H. Bachacou,[135] K. Bachas,[152,f] A. Bachiu,[34] F. Backman,[47a,47b] A. Badea,[61] P. Bagnaia,[75a,75b] M. Bahmani,[18] A. J. Bailey,[163] V. R. Bailey,[162] J. T. Baines,[134] L. Baines,[94] C. Bakalis,[10] O. K. Baker,[172] E. Bakos,[15] D. Bakshi Gupta,[8] V. Balakrishnan,[120] R. Balasubramanian,[114] E. M. Baldin,[37] P. Balek,[86a] E. Ballabene,[23b,23a] F. Balli,[135] L. M. Baltes,[63a] W. K. Balunas,[32] J. Balz,[100] E. Banas,[87] M. Bandieramonte,[129] A. Bandyopadhyay,[24] S. Bansal,[24] L. Barak,[151] M. Barakat,[48] E. L. Barberio,[105] D. Barberis,[57b,57a] M. Barbero,[102] M. Z. Barel,[114] K. N. Barends,[33a] T. Barillari,[110] M-S. Barisits,[36] T. Barklow,[143] P. Baron,[122] D. A. Baron Moreno,[101] A. Baroncelli,[62a] G. Barone,[29] A. J. Barr,[126] J. D. Barr,[96] L. Barranco Navarro,[47a,47b] F. Barreiro,[99] J. Barreiro Guimarães da Costa,[14a] U. Barron,[151] M. G. Barros Teixeira,[130a] S. Barsov,[37] F. Bartels,[63a] R. Bartoldus,[143] A. E. Barton,[91] P. Bartos,[28a] A. Basan,[100] M. Baselga,[49] A. Bassalat,[66,g] M. J. Basso,[156a] C. R. Basson,[101] R. L. Bates,[59] S. Batlamous,[35e] J. R. Batley,[32] B. Batool,[141] M. Battaglia,[136] D. Battulga,[18] M. Bauce,[75a,75b] M. Bauer,[36] P. Bauer,[24] L. T. Bazzano Hurrell,[30] J. B. Beacham,[51] T. Beau,[127] P. H. Beauchemin,[158] F. Becherer,[54] P. Bechtle,[24] H. P. Beck,[19,h] K. Becker,[167] A. J. Beddall,[82] V. A. Bednyakov,[38] C. P. Bee,[145] L. J. Beemster,[15] T. A. Beermann,[36] M. Begalli,[83d] M. Begel,[29] A. Behera,[145] J. K. Behr,[48] J. F. Beirer,[55] F. Beisiegel,[24] M. Belfkir,[159] G. Bella,[151] L. Bellagamba,[23b] A. Bellerive,[34] P. Bellos,[20] K. Beloborodov,[37] N. L. Belyaev,[37] D. Benchekroun,[35a] F. Bendebba,[35a] Y. Benhammou,[151] M. Benoit,[29] J. R. Bensinger,[26] S. Bentvelsen,[114] L. Beresford,[48] M. Beretta,[53] E. Bergeaas Kuutmann,[161] N. Berger,[4] B. Bergmann,[132] J. Beringer,[17a] G. Bernardi,[5] C. Bernius,[143] F. U. Bernlochner,[24] F. Bernon,[36,102]

T. Berry,[95] P. Berta,[133] A. Berthold,[50] I. A. Bertram,[91] S. Bethke,[110] A. Betti,[75a,75b] A. J. Bevan,[94] M. Bhamjee,[33c] S. Bhatta,[145] D. S. Bhattacharya,[166] P. Bhattarai,[143] V. S. Bhopatkar,[121] R. Bi,[29,i] R. M. Bianchi,[129] G. Bianco,[23b,23a] O. Biebel,[109] R. Bielski,[123] M. Biglietti,[77a] T. R. V. Billoud,[132] M. Bindi,[55] A. Bingul,[21b] C. Bini,[75a,75b] A. Biondini,[92] C. J. Birch-sykes,[101] G. A. Bird,[20,134] M. Birman,[169] M. Biros,[133] S. Biryukov,[146] T. Bisanz,[49] E. Bisceglie,[43b,43a] J. P. Biswal,[134] D. Biswas,[141] A. Bitadze,[101] K. Bjørke,[125] I. Bloch,[48] C. Blocker,[26] A. Blue,[59] U. Blumenschein,[94] J. Blumenthal,[100] G. J. Bobbink,[114] V. S. Bobrovnikov,[37] M. Boehler,[54] B. Boehm,[166] D. Bogavac,[36] A. G. Bogdanchikov,[37] C. Bohm,[47a] V. Boisvert,[95] P. Bokan,[48] T. Bold,[86a] M. Bomben,[5] M. Bona,[94] M. Boonekamp,[135] C. D. Booth,[95] A. G. Borbély,[59] I. S. Bordulev,[37] H. M. Borecka-Bielska,[108] L. S. Borgna,[96] G. Borissov,[91] D. Bortoletto,[126] D. Boscherini,[23b] M. Bosman,[13] J. D. Bossio Sola,[36] K. Bouaouda,[35a] N. Bouchhar,[163] J. Boudreau,[129] E. V. Bouhova-Thacker,[91] D. Boumediene,[40] R. Bouquet,[5] A. Boveia,[119] J. Boyd,[36] D. Boye,[29] I. R. Boyko,[38] J. Bracinik,[20] N. Brahimi,[62d] G. Brandt,[171] O. Brandt,[32] F. Braren,[48] B. Brau,[103] J. E. Brau,[123] R. Brener,[169] L. Brenner,[114] R. Brenner,[161] S. Bressler,[169] D. Britton,[59] D. Britzger,[110] I. Brock,[24] G. Brooijmans,[41] W. K. Brooks,[137f] E. Brost,[29] L. M. Brown,[165] L. E. Bruce,[61] T. L. Bruckler,[126] P. A. Bruckman de Renstrom,[87] B. Brüers,[48] A. Bruni,[23b] G. Bruni,[23b] M. Bruschi,[23b] N. Bruscino,[75a,75b] T. Buanes,[16] Q. Buat,[138] D. Buchin,[110] A. G. Buckley,[59] O. Bulekov,[37] B. A. Bullard,[143] S. Burdin,[92] C. D. Burgard,[49] A. M. Burger,[40] B. Burghgrave,[8] O. Burlayenko,[54] J. T. P. Burr,[32] C. D. Burton,[11] J. C. Burzynski,[142] E. L. Busch,[41] V. Büscher,[100] P. J. Bussey,[59] J. M. Butler,[25] C. M. Buttar,[59] J. M. Butterworth,[96] W. Buttinger,[134] C. J. Buxo Vazquez,[107] A. R. Buzykaev,[37] S. Cabrera Urbán,[163] L. Cadamuro,[66] D. Caforio,[58] H. Cai,[129] Y. Cai,[14a,14e] V. M. M. Cairo,[36] O. Cakir,[3a] N. Calace,[36] P. Calafiura,[17a] G. Calderini,[127] P. Calfayan,[68] G. Callea,[59] L. P. Caloba,[83b] D. Calvet,[40] S. Calvet,[40] T. P. Calvet,[102] M. Calvetti,[74a,74b] R. Camacho Toro,[127] S. Camarda,[36] D. Camarero Munoz,[26] P. Camarri,[76a,76b] M. T. Camerlingo,[72a,72b] D. Cameron,[36] C. Camincher,[165] M. Campanelli,[96] A. Camplani,[42] V. Canale,[72a,72b] A. Canesse,[104] J. Cantero,[163] Y. Cao,[162] F. Capocasa,[26] M. Capua,[43b,43a] A. Carbone,[71a,71b] R. Cardarelli,[76a] J. C. J. Cardenas,[8] F. Cardillo,[163] T. Carli,[36] G. Carlino,[72a] J. I. Carlotto,[13] B. T. Carlson,[129,j] E. M. Carlson,[165,156a] L. Carminati,[71a,71b] A. Carnelli,[135] M. Carnesale,[75a,75b] S. Caron,[113] E. Carquin,[137f] S. Carrá,[71a] G. Carratta,[23b,23a] F. Carrio Argos,[33g] J. W. S. Carter,[155] T. M. Carter,[52] M. P. Casado,[13,k] M. Caspar,[48] E. G. Castiglia,[172] F. L. Castillo,[4] L. Castillo Garcia,[13] V. Castillo Gimenez,[163] N. F. Castro,[130a,130e] A. Catinaccio,[36] J. R. Catmore,[125] V. Cavaliere,[29] N. Cavalli,[23b,23a] V. Cavasinni,[74a,74b] Y. C. Cekmecelioglu,[48] E. Celebi,[21a] F. Celli,[126] M. S. Centonze,[70a,70b] V. Cepaitis,[56] K. Cerny,[122] A. S. Cerqueira,[83a] A. Cerri,[146] L. Cerrito,[76a,76b] F. Cerutti,[17a] B. Cervato,[141] A. Cervelli,[23b] G. Cesarini,[53] S. A. Cetin,[82] Z. Chadi,[35a] D. Chakraborty,[115] J. Chan,[170] W. Y. Chan,[153] J. D. Chapman,[32] E. Chapon,[135] B. Chargeishvili,[149b] D. G. Charlton,[20] T. P. Charman,[94] M. Chatterjee,[19] C. Chauhan,[133] S. Chekanov,[6] S. V. Chekulaev,[156a] G. A. Chelkov,[38,l] A. Chen,[106] B. Chen,[151] B. Chen,[165] H. Chen,[14c] H. Chen,[29] J. Chen,[62c] J. Chen,[142] M. Chen,[126] S. Chen,[153] S. J. Chen,[14c] X. Chen,[62c,135] X. Chen,[14b,m] Y. Chen,[62a] C. L. Cheng,[170] H. C. Cheng,[64a] S. Cheong,[143] A. Cheplakov,[38] E. Cheremushkina,[48] E. Cherepanova,[114] R. Cherkaoui El Moursli,[35e] E. Cheu,[7] K. Cheung,[65] L. Chevalier,[135] V. Chiarella,[53] G. Chiarelli,[74a] N. Chiedde,[102] G. Chiodini,[70a] A. S. Chisholm,[20] A. Chitan,[27b] M. Chitishvili,[163] M. V. Chizhov,[38] K. Choi,[11] A. R. Chomont,[75a,75b] Y. Chou,[103] E. Y. S. Chow,[114] T. Chowdhury,[33g] K. L. Chu,[169] M. C. Chu,[64a] X. Chu,[14a,14e] J. Chudoba,[131] J. J. Chwastowski,[87] D. Cieri,[110] K. M. Ciesla,[86a] V. Cindro,[93] A. Ciocio,[17a] F. Cirotto,[72a,72b] Z. H. Citron,[169,n] M. Citterio,[71a] D. A. Ciubotaru,[27b] B. M. Ciungu,[155] A. Clark,[56] P. J. Clark,[52] J. M. Clavijo Columbie,[48] S. E. Clawson,[48] C. Clement,[47a,47b] J. Clercx,[48] Y. Coadou,[102] M. Cobal,[69a,69c] A. Coccaro,[57b] R. F. Coelho Barrue,[130a] R. Coelho Lopes De Sa,[103] S. Coelli,[71a] H. Cohen,[151] A. E. C. Coimbra,[71a,71b] B. Cole,[41] J. Collot,[60] P. Conde Muiño,[130a,130g] M. P. Connell,[33c] S. H. Connell,[33c] I. A. Connelly,[59] E. I. Conroy,[126] F. Conventi,[72a,o] H. G. Cooke,[20] A. M. Cooper-Sarkar,[126] A. Cordeiro Oudot Choi,[127] F. Cormier,[164] L. D. Corpe,[40] M. Corradi,[75a,75b] F. Corriveau,[104,p] A. Cortes-Gonzalez,[18] M. J. Costa,[163] F. Costanza,[4] D. Costanzo,[139] B. M. Cote,[119] G. Cowan,[95] K. Cranmer,[170] D. Cremonini,[23b,23a] S. Crépé-Renaudin,[60] F. Crescioli,[127] M. Cristinziani,[141] M. Cristoforetti,[78a,78b] V. Croft,[114] J. E. Crosby,[121] G. Crosetti,[43b,43a] A. Cueto,[99] T. Cuhadar Donszelmann,[160] H. Cui,[14a,14e] Z. Cui,[7] W. R. Cunningham,[59] F. Curcio,[43b,43a] P. Czodrowski,[36] M. M. Czurylo,[63b]

M. J. Da Cunha Sargedas De Sousa,[57b,57a] J. V. Da Fonseca Pinto,[83b] C. Da Via,[101] W. Dabrowski,[86a] T. Dado,[49] S. Dahbi,[33g] T. Dai,[106] D. Dal Santo,[19] C. Dallapiccola,[103] M. Dam,[42] G. D'amen,[29] V. D'Amico,[109] J. Damp,[100] J. R. Dandoy,[128] M. F. Daneri,[30] M. Danninger,[142] V. Dao,[36] G. Darbo,[57b] S. Darmora,[6] S. J. Das,[29,i] S. D'Auria,[71a,71b] C. David,[156b] T. Davidek,[133] B. Davis-Purcell,[34] I. Dawson,[94] H. A. Day-hall,[132] K. De,[8] R. De Asmundis,[72a] N. De Biase,[48] S. De Castro,[23b,23a] N. De Groot,[113] P. de Jong,[114] H. De la Torre,[115] A. De Maria,[14c] A. De Salvo,[75a] U. De Sanctis,[76a,76b] A. De Santo,[146] J. B. De Vivie De Regie,[60] D. V. Dedovich,[38] J. Degens,[114] A. M. Deiana,[44] F. Del Corso,[23b,23a] J. Del Peso,[99] F. Del Rio,[63a] F. Deliot,[135] C. M. Delitzsch,[49] M. Della Pietra,[72a,72b] D. Della Volpe,[56] A. Dell'Acqua,[36] L. Dell'Asta,[71a,71b] M. Delmastro,[4] P. A. Delsart,[60] S. Demers,[172] M. Demichev,[38] S. P. Denisov,[37] L. D'Eramo,[40] D. Derendarz,[87] F. Derue,[127] P. Dervan,[92] K. Desch,[24] C. Deutsch,[24] F. A. Di Bello,[57b,57a] A. Di Ciaccio,[76a,76b] L. Di Ciaccio,[4] A. Di Domenico,[75a,75b] C. Di Donato,[72a,72b] A. Di Girolamo,[36] G. Di Gregorio,[5] A. Di Luca,[78a,78b] B. Di Micco,[77a,77b] R. Di Nardo,[77a,77b] C. Diaconu,[102] M. Diamantopoulou,[34] F. A. Dias,[114] T. Dias Do Vale,[142] M. A. Diaz,[137a,137b] F. G. Diaz Capriles,[24] M. Didenko,[163] E. B. Diehl,[106] L. Diehl,[54] S. Díez Cornell,[48] C. Diez Pardos,[141] C. Dimitriadi,[161,24,161] A. Dimitrievska,[17a] J. Dingfelder,[24] I-M. Dinu,[27b] S. J. Dittmeier,[63b] F. Dittus,[36] F. Djama,[102] T. Djobava,[149b] J. I. Djuvsland,[16] C. Doglioni,[101,98] A. Dohnalova,[28a] J. Dolejsi,[133] Z. Dolezal,[133] K. M. Dona,[39] M. Donadelli,[83c] B. Dong,[107] J. Donini,[40] A. D'Onofrio,[77a,77b] M. D'Onofrio,[92] J. Dopke,[134] A. Doria,[72a] N. Dos Santos Fernandes,[130a] P. Dougan,[101] M. T. Dova,[90] A. T. Doyle,[59] M. A. Draguet,[126] E. Dreyer,[169] I. Drivas-koulouris,[10] A. S. Drobac,[158] M. Drozdova,[56] D. Du,[62a] T. A. du Pree,[114] F. Dubinin,[37] M. Dubovsky,[28a] E. Duchovni,[169] G. Duckeck,[109] O. A. Ducu,[27b] D. Duda,[52] A. Dudarev,[36] E. R. Duden,[26] M. D'uffizi,[101] L. Duflot,[66] M. Dührssen,[36] C. Dülsen,[171] A. E. Dumitriu,[27b] M. Dunford,[63a] S. Dungs,[49] K. Dunne,[47a,47b] A. Duperrin,[102] H. Duran Yildiz,[3a] M. Düren,[58] A. Durglishvili,[149b] B. L. Dwyer,[115] G. I. Dyckes,[17a] M. Dyndal,[86a] S. Dysch,[101] B. S. Dziedzic,[87] Z. O. Earnshaw,[146] G. H. Eberwein,[126] B. Eckerova,[28a] S. Eggebrecht,[55] E. Egidio Purcino De Souza,[127] L. F. Ehrke,[56] G. Eigen,[16] K. Einsweiler,[17a] T. Ekelof,[161] P. A. Ekman,[98] S. El Farkh,[35b] Y. El Ghazali,[35b] H. El Jarrari,[35e,148] A. El Moussaouy,[35a] V. Ellajosyula,[161] M. Ellert,[161] F. Ellinghaus,[171] A. A. Elliot,[94] N. Ellis,[36] J. Elmsheuser,[29] M. Elsing,[36] D. Emeliyanov,[134] Y. Enari,[153] I. Ene,[17a] S. Epari,[13] J. Erdmann,[49] P. A. Erland,[87] M. Errenst,[171] M. Escalier,[66] C. Escobar,[163] E. Etzion,[151] G. Evans,[130a] H. Evans,[68] L. S. Evans,[95] M. O. Evans,[146] A. Ezhilov,[37] S. Ezzarqtouni,[35a] F. Fabbri,[59] L. Fabbri,[23b,23a] G. Facini,[96] V. Fadeyev,[136] R. M. Fakhrutdinov,[37] S. Falciano,[75a] L. F. Falda Ulhoa Coelho,[36] P. J. Falke,[24] J. Faltova,[133] C. Fan,[162] Y. Fan,[14a] Y. Fang,[14a,14e] M. Fanti,[71a,71b] M. Faraj,[69a,69b] Z. Farazpay,[97] A. Farbin,[8] A. Farilla,[77a] T. Farooque,[107] S. M. Farrington,[52] F. Fassi,[35e] D. Fassouliotis,[9] M. Faucci Giannelli,[76a,76b] W. J. Fawcett,[32] L. Fayard,[66] P. Federic,[133] P. Federicova,[131] O. L. Fedin,[37,l] G. Fedotov,[37] M. Feickert,[170] L. Feligioni,[102] D. E. Fellers,[123] C. Feng,[62b] M. Feng,[14b] Z. Feng,[114] M. J. Fenton,[160] A. B. Fenyuk,[37] L. Ferencz,[48] R. A. M. Ferguson,[91] S. I. Fernandez Luengo,[137f] M. J. V. Fernoux,[102] J. Ferrando,[48] A. Ferrari,[161] P. Ferrari,[114,113] R. Ferrari,[73a] D. Ferrere,[56] C. Ferretti,[106] F. Fiedler,[100] A. Filipčič,[93] E. K. Filmer,[1] F. Filthaut,[113] M. C. N. Fiolhais,[130a,130c,q] L. Fiorini,[163] W. C. Fisher,[107] T. Fitschen,[101] P. M. Fitzhugh,[135] I. Fleck,[141] P. Fleischmann,[106] T. Flick,[171] M. Flores,[33d,r] L. R. Flores Castillo,[64a] L. Flores Sanz De Acedo,[36] F. M. Follega,[78a,78b] N. Fomin,[16] J. H. Foo,[155] B. C. Forland,[68] A. Formica,[135] A. C. Forti,[101] E. Fortin,[36] A. W. Fortman,[61] M. G. Foti,[17a] L. Fountas,[9,s] D. Fournier,[66] H. Fox,[91] P. Francavilla,[74a,74b] S. Francescato,[61] S. Franchellucci,[56] M. Franchini,[23b,23a] S. Franchino,[63a] D. Francis,[36] L. Franco,[113] L. Franconi,[48] M. Franklin,[61] G. Frattari,[26] A. C. Freegard,[94] W. S. Freund,[83b] Y. Y. Frid,[151] J. Friend,[59] N. Fritzsche,[50] A. Froch,[54] D. Froidevaux,[36] J. A. Frost,[126] Y. Fu,[62a] M. Fujimoto,[118,t] E. Fullana Torregrosa,[163,a] K. Y. Fung,[64a] E. Furtado De Simas Filho,[83b] M. Furukawa,[153] J. Fuster,[163] A. Gabrielli,[23b,23a] A. Gabrielli,[155] P. Gadow,[36] G. Gagliardi,[57b,57a] L. G. Gagnon,[17a] E. J. Gallas,[126] B. J. Gallop,[134] K. K. Gan,[119] S. Ganguly,[153] J. Gao,[62a] Y. Gao,[52] F. M. Garay Walls,[137a,137b] B. Garcia,[29] C. García,[163] A. Garcia Alonso,[114] A. G. Garcia Caffaro,[172] J. E. García Navarro,[163] M. Garcia-Sciveres,[17a] G. L. Gardner,[128] R. W. Gardner,[39] N. Garelli,[158] D. Garg,[80] R. B. Garg,[143,u] J. M. Gargan,[52] C. A. Garner,[155] S. J. Gasiorowski,[138] P. Gaspar,[83b] G. Gaudio,[73a] V. Gautam,[13] P. Gauzzi,[75a,75b] I. L. Gavrilenko,[37] A. Gavrilyuk,[37] C. Gay,[164] G. Gaycken,[48] E. N. Gazis,[10] A. A. Geanta,[27b] C. M. Gee,[136] C. Gemme,[57b] M. H. Genest,[60] S. Gentile,[75a,75b] A. D. Gentry,[112] S. George,[95] W. F. George,[20] T. Geralis,[46] P. Gessinger-Befurt,[36]

M. E. Geyik,[171] M. Ghani,[167] M. Ghneimat,[141] K. Ghorbanian,[94] A. Ghosal,[141] A. Ghosh,[160] A. Ghosh,[7] B. Giacobbe,[23b] S. Giagu,[75a,75b] T. Giani,[114] P. Giannetti,[74a] A. Giannini,[62a] S. M. Gibson,[95] M. Gignac,[136] D. T. Gil,[86b] A. K. Gilbert,[86a] B. J. Gilbert,[41] D. Gillberg,[34] G. Gilles,[114] N. E. K. Gillwald,[48] L. Ginabat,[127] D. M. Gingrich,[2,e] M. P. Giordani,[69a,69c] P. F. Giraud,[135] G. Giugliarelli,[69a,69c] D. Giugni,[71a] F. Giuli,[36] I. Gkialas,[9,s] L. K. Gladilin,[37] C. Glasman,[99] G. R. Gledhill,[123] G. Glemža,[48] M. Glisic,[123] I. Gnesi,[43b,v] Y. Go,[29,i] M. Goblirsch-Kolb,[36] B. Gocke,[49] D. Godin,[108] B. Gokturk,[21a] S. Goldfarb,[105] T. Golling,[56] M. G. D. Gololo,[33g] D. Golubkov,[37] J. P. Gombas,[107] A. Gomes,[130a,130b] G. Gomes Da Silva,[141] A. J. Gomez Delegido,[163] R. Gonçalo,[130a,130c] G. Gonella,[123] L. Gonella,[20] A. Gongadze,[149c] F. Gonnella,[20] J. L. Gonski,[41] R. Y. González Andana,[52] S. González de la Hoz,[163] S. Gonzalez Fernandez,[13] R. Gonzalez Lopez,[92] C. Gonzalez Renteria,[17a] M. V. Gonzalez Rodrigues,[48] R. Gonzalez Suarez,[161] S. Gonzalez-Sevilla,[56] G. R. Gonzalvo Rodriguez,[163] L. Goossens,[36] B. Gorini,[36] E. Gorini,[70a,70b] A. Gorišek,[93] T. C. Gosart,[128] A. T. Goshaw,[51] M. I. Gostkin,[38] S. Goswami,[121] C. A. Gottardo,[36] S. A. Gotz,[109] M. Gouighri,[35b] V. Goumarre,[48] A. G. Goussiou,[138] N. Govender,[33c] I. Grabowska-Bold,[86a] K. Graham,[34] E. Gramstad,[125] S. Grancagnolo,[70a,70b] M. Grandi,[146] C. M. Grant,[1,135] P. M. Gravila,[27f] F. G. Gravili,[70a,70b] H. M. Gray,[17a] M. Greco,[70a,70b] C. Grefe,[24] I. M. Gregor,[48] P. Grenier,[143] C. Grieco,[13] A. A. Grillo,[136] K. Grimm,[31] S. Grinstein,[13,w] J.-F. Grivaz,[66] E. Gross,[169] J. Grosse-Knetter,[55] C. Grud,[106] J. C. Grundy,[126] L. Guan,[106] W. Guan,[29] C. Gubbels,[164] J. G. R. Guerrero Rojas,[163] G. Guerrieri,[69a,69c] F. Guescini,[110] R. Gugel,[100] J. A. M. Guhit,[106] A. Guida,[18] T. Guillemin,[4] E. Guilloton,[167,134] S. Guindon,[36] F. Guo,[14a,14e] J. Guo,[62c] L. Guo,[48] Y. Guo,[106] R. Gupta,[48] S. Gurbuz,[24] S. S. Gurdasani,[54] G. Gustavino,[36] M. Guth,[56] P. Gutierrez,[120] L. F. Gutierrez Zagazeta,[128] C. Gutschow,[96] C. Gwenlan,[126] C. B. Gwilliam,[92] E. S. Haaland,[125] A. Haas,[117] M. Habedank,[48] C. Haber,[17a] H. K. Hadavand,[8] A. Hadef,[100] S. Hadzic,[110] J. J. Hahn,[141] E. H. Haines,[96] M. Haleem,[166] J. Haley,[121] J. J. Hall,[139] G. D. Hallewell,[102] L. Halser,[19] K. Hamano,[165] M. Hamer,[24] G. N. Hamity,[52] E. J. Hampshire,[95] J. Han,[62b] K. Han,[62a] L. Han,[14c] L. Han,[62a] S. Han,[17a] Y. F. Han,[155] K. Hanagaki,[84] M. Hance,[136] D. A. Hangal,[41,d] H. Hanif,[142] M. D. Hank,[128] R. Hankache,[101] J. B. Hansen,[42] J. D. Hansen,[42] P. H. Hansen,[42] K. Hara,[157] D. Harada,[56] T. Harenberg,[171] S. Harkusha,[37] M. L. Harris,[103] Y. T. Harris,[126] J. Harrison,[13] N. M. Harrison,[119] P. F. Harrison,[167] N. M. Hartman,[110] N. M. Hartmann,[109] Y. Hasegawa,[140] A. Hasib,[52] S. Haug,[19] R. Hauser,[107] C. M. Hawkes,[20] R. J. Hawkings,[36] Y. Hayashi,[153] S. Hayashida,[111] D. Hayden,[107] C. Hayes,[106] R. L. Hayes,[114] C. P. Hays,[126] J. M. Hays,[94] H. S. Hayward,[92] F. He,[62a] M. He,[14a,14e] Y. He,[154] Y. He,[48] N. B. Heatley,[94] V. Hedberg,[98] A. L. Heggelund,[125] N. D. Hehir,[94,a] C. Heidegger,[54] K. K. Heidegger,[54] W. D. Heidorn,[81] J. Heilman,[34] S. Heim,[48] T. Heim,[17a] J. G. Heinlein,[128] J. J. Heinrich,[123] L. Heinrich,[110,x] J. Hejbal,[131] L. Helary,[48] A. Held,[170] S. Hellesund,[16] C. M. Helling,[164] S. Hellman,[47a,47b] R. C. W. Henderson,[91] L. Henkelmann,[32] A. M. Henriques Correia,[36] H. Herde,[98] Y. Hernández Jiménez,[145] L. M. Herrmann,[24] T. Herrmann,[50] G. Herten,[54] R. Hertenberger,[109] L. Hervas,[36] M. E. Hesping,[100] N. P. Hessey,[156a] H. Hibi,[85] S. J. Hillier,[20] J. R. Hinds,[107] F. Hinterkeuser,[24] M. Hirose,[124] S. Hirose,[157] D. Hirschbuehl,[171] T. G. Hitchings,[101] B. Hiti,[93] J. Hobbs,[145] R. Hobincu,[27e] N. Hod,[169] M. C. Hodgkinson,[139] B. H. Hodkinson,[32] A. Hoecker,[36] J. Hofer,[48] T. Holm,[24] M. Holzbock,[110] L. B. A. H. Hommels,[32] B. P. Honan,[101] J. Hong,[62c] T. M. Hong,[129] B. H. Hooberman,[162] W. H. Hopkins,[6] Y. Horii,[111] S. Hou,[148] A. S. Howard,[93] J. Howarth,[59] J. Hoya,[6] M. Hrabovsky,[122] A. Hrynevich,[48] T. Hryn'ova,[4] P. J. Hsu,[65] S.-C. Hsu,[138] Q. Hu,[62a] Y. F. Hu,[14a,14e] S. Huang,[64b] X. Huang,[14c] Y. Huang,[139] Y. Huang,[14a] Z. Huang,[101] Z. Hubacek,[132] M. Huebner,[24] F. Huegging,[24] T. B. Huffman,[126] C. A. Hugli,[48] M. Huhtinen,[36] S. K. Huiberts,[16] R. Hulsken,[104] N. Huseynov,[12] J. Huston,[107] J. Huth,[61] R. Hyneman,[143] G. Iacobucci,[56] G. Iakovidis,[29] I. Ibragimov,[141] L. Iconomidou-Fayard,[66] P. Iengo,[72a,72b] R. Iguchi,[153] T. Iizawa,[126] Y. Ikegami,[84] N. Ilic,[155] H. Imam,[35a] M. Ince Lezki,[56] T. Ingebretsen Carlson,[47a,47b] G. Introzzi,[73a,73b] M. Iodice,[77a] V. Ippolito,[75a,75b] R. K. Irwin,[92] M. Ishino,[153] W. Islam,[170] C. Issever,[18,48] S. Istin,[21a,y] H. Ito,[168] J. M. Iturbe Ponce,[64a] R. Iuppa,[78a,78b] A. Ivina,[169] J. M. Izen,[45] V. Izzo,[72a] P. Jacka,[131,132] P. Jackson,[1] R. M. Jacobs,[48] B. P. Jaeger,[142] C. S. Jagfeld,[109] G. Jain,[156a] P. Jain,[54] G. Jäkel,[171] K. Jakobs,[54] T. Jakoubek,[169] J. Jamieson,[59] K. W. Janas,[86a] M. Javurkova,[103] F. Jeanneau,[135] L. Jeanty,[123] J. Jejelava,[149a,z] P. Jenni,[54,aa] C. E. Jessiman,[34] S. Jézéquel,[4] C. Jia,[62b] J. Jia,[145] X. Jia,[61] X. Jia,[14a,14e] Z. Jia,[14c] Y. Jiang,[62a] S. Jiggins,[48] J. Jimenez Pena,[13] S. Jin,[14c] A. Jinaru,[27b] O. Jinnouchi,[154] P. Johansson,[139] K. A. Johns,[7]

J. W. Johnson,[136] D. M. Jones,[32] E. Jones,[48] P. Jones,[32] R. W. L. Jones,[91] T. J. Jones,[92] H. L. Joos,[55,36] R. Joshi,[119] J. Jovicevic,[15] X. Ju,[17a] J. J. Junggeburth,[103] T. Junkermann,[63a] A. Juste Rozas,[13,w] M. K. Juzek,[87] S. Kabana,[137e] A. Kaczmarska,[87] M. Kado,[110] H. Kagan,[119] M. Kagan,[143] A. Kahn,[41] A. Kahn,[128] C. Kahra,[100] T. Kaji,[153] E. Kajomovitz,[150] N. Kakati,[169] I. Kalaitzidou,[54] C. W. Kalderon,[29] A. Kamenshchikov,[155] N. J. Kang,[136] D. Kar,[33g] K. Karava,[126] M. J. Kareem,[156b] E. Karentzos,[54] I. Karkanias,[152] O. Karkout,[114] S. N. Karpov,[38] Z. M. Karpova,[38] V. Kartvelishvili,[91] A. N. Karyukhin,[37] E. Kasimi,[152] J. Katzy,[48] S. Kaur,[34] K. Kawade,[140] M. P. Kawale,[120] T. Kawamoto,[135] E. F. Kay,[36] F. I. Kaya,[158] S. Kazakos,[107] V. F. Kazanin,[37] Y. Ke,[145] J. M. Keaveney,[33a] R. Keeler,[165] G. V. Kehris,[61] J. S. Keller,[34] A. S. Kelly,[96] J. J. Kempster,[146] K. E. Kennedy,[41] P. D. Kennedy,[100] O. Kepka,[131] B. P. Kerridge,[167] S. Kersten,[171] B. P. Kerševan,[93] S. Keshri,[66] L. Keszeghova,[28a] S. Ketabchi Haghighat,[155] M. Khandoga,[127] A. Khanov,[121] A. G. Kharlamov,[37] T. Kharlamova,[37] E. E. Khoda,[138] T. J. Khoo,[18] G. Khoriauli,[166] J. Khubua,[149b] Y. A. R. Khwaira,[66] A. Kilgallon,[123] D. W. Kim,[47a,47b] Y. K. Kim,[39] N. Kimura,[96] M. K. Kingston,[55] A. Kirchhoff,[55] C. Kirfel,[24] F. Kirfel,[24] J. Kirk,[134] A. E. Kiryunin,[110] C. Kitsaki,[10] O. Kivernyk,[24] M. Klassen,[63a] C. Klein,[34] L. Klein,[166] M. H. Klein,[106] M. Klein,[92] S. B. Klein,[56] U. Klein,[92] P. Klimek,[36] A. Klimentov,[29] T. Klioutchnikova,[36] P. Kluit,[114] S. Kluth,[110] E. Kneringer,[79] T. M. Knight,[155] A. Knue,[49] R. Kobayashi,[88] D. Kobylianskii,[169] S. F. Koch,[126] M. Kocian,[143] P. Kodyš,[133] D. M. Koeck,[123] P. T. Koenig,[24] T. Koffas,[34] M. Kolb,[135] I. Koletsou,[4] T. Komarek,[122] K. Köneke,[54] A. X. Y. Kong,[1] T. Kono,[118] N. Konstantinidis,[96] B. Konya,[98] R. Kopeliansky,[68] S. Koperny,[86a] K. Korcyl,[87] K. Kordas,[152,bb] G. Koren,[151] A. Korn,[96] S. Korn,[55] I. Korolkov,[13] N. Korotkova,[37] B. Kortman,[114] O. Kortner,[110] S. Kortner,[110] W. H. Kostecka,[115] V. V. Kostyukhin,[141] A. Kotsokechagia,[135] A. Kotwal,[51] A. Koulouris,[36] A. Kourkoumeli-Charalampidi,[73a,73b] C. Kourkoumelis,[9] E. Kourlitis,[110,x] O. Kovanda,[146] R. Kowalewski,[165] W. Kozanecki,[135] A. S. Kozhin,[37] V. A. Kramarenko,[37] G. Kramberger,[93] P. Kramer,[100] M. W. Krasny,[127] A. Krasznahorkay,[36] J. W. Kraus,[171] J. A. Kremer,[100] T. Kresse,[50] J. Kretzschmar,[92] K. Kreul,[18] P. Krieger,[155] S. Krishnamurthy,[103] M. Krivos,[133] K. Krizka,[20] K. Kroeninger,[49] H. Kroha,[110] J. Kroll,[131] J. Kroll,[128] K. S. Krowpman,[107] U. Kruchonak,[38] H. Krüger,[24] N. Krumnack,[81] M. C. Kruse,[51] J. A. Krzysiak,[87] O. Kuchinskaia,[37] S. Kuday,[3a] S. Kuehn,[36] R. Kuesters,[54] T. Kuhl,[48] V. Kukhtin,[38] Y. Kulchitsky,[37,l] S. Kuleshov,[137d,137b] M. Kumar,[33g] N. Kumari,[48] A. Kupco,[131] T. Kupfer,[49] A. Kupich,[37] O. Kuprash,[54] H. Kurashige,[85] L. L. Kurchaninov,[156a] O. Kurdysh,[66] Y. A. Kurochkin,[37] A. Kurova,[37] M. Kuze,[154] A. K. Kvam,[103] J. Kvita,[122] T. Kwan,[104] N. G. Kyriacou,[106] L. A. O. Laatu,[102] C. Lacasta,[163] F. Lacava,[75a,75b] H. Lacker,[18] D. Lacour,[127] N. N. Lad,[96] E. Ladygin,[38] B. Laforge,[127] T. Lagouri,[137e] F. Z. Lahbabi,[35a] S. Lai,[55] I. K. Lakomiec,[86a] N. Lalloue,[60] J. E. Lambert,[165] S. Lammers,[68] W. Lampl,[7] C. Lampoudis,[152,bb] A. N. Lancaster,[115] E. Lançon,[29] U. Landgraf,[54] M. P. J. Landon,[94] V. S. Lang,[54] R. J. Langenberg,[103] O. K. B. Langrekken,[125] A. J. Lankford,[160] F. Lanni,[36] K. Lantzsch,[24] A. Lanza,[73a] A. Lapertosa,[57b,57a] J. F. Laporte,[135] T. Lari,[71a] F. Lasagni Manghi,[23b] M. Lassnig,[36] V. Latonova,[131] A. Laudrain,[100] A. Laurier,[150] S. D. Lawlor,[95] Z. Lawrence,[101] M. Lazzaroni,[71a,71b] B. Le,[101] E. M. Le Boulicaut,[51] B. Leban,[93] A. Lebedev,[81] M. LeBlanc,[101] F. Ledroit-Guillon,[60] A. C. A. Lee,[96] S. C. Lee,[148] S. Lee,[47a,47b] T. F. Lee,[92] L. L. Leeuw,[33c] H. P. Lefebvre,[95] M. Lefebvre,[165] C. Leggett,[17a] G. Lehmann Miotto,[36] M. Leigh,[56] W. A. Leight,[103] W. Leinonen,[113] A. Leisos,[152,cc] M. A. L. Leite,[83c] C. E. Leitgeb,[48] R. Leitner,[133] K. J. C. Leney,[44] T. Lenz,[24] S. Leone,[74a] C. Leonidopoulos,[52] A. Leopold,[144] C. Leroy,[108] R. Les,[107] C. G. Lester,[32] M. Levchenko,[37] J. Levêque,[4] D. Levin,[106] L. J. Levinson,[169] M. P. Lewicki,[87] D. J. Lewis,[4] A. Li,[5] B. Li,[62b] C. Li,[62a] C-Q. Li,[62c] H. Li,[62a] H. Li,[62b] H. Li,[14c] H. Li,[14b] H. Li,[62b] K. Li,[138] L. Li,[62c] M. Li,[14a,14e] Q. Y. Li,[62a] S. Li,[14a,14e] S. Li,[62d,62c,dd] T. Li,[5] X. Li,[104] Z. Li,[126] Z. Li,[104] Z. Li,[92] Z. Li,[14a,14e] S. Liang,[14a,14e] Z. Liang,[14a] M. Liberatore,[135] B. Liberti,[76a] K. Lie,[64c] J. Lieber Marin,[83b] H. Lien,[68] K. Lin,[107] R. E. Lindley,[7] J. H. Lindon,[2] E. Lipeles,[128] A. Lipniacka,[16] A. Lister,[164] J. D. Little,[4] B. Liu,[14a] B. X. Liu,[142] D. Liu,[62d,62c] J. B. Liu,[62a] J. K. K. Liu,[32] K. Liu,[62d,62c] M. Liu,[62a] M. Y. Liu,[62a] P. Liu,[14a] Q. Liu,[62d,138,62c] X. Liu,[62a] Y. Liu,[14d,14e] Y. L. Liu,[62b] Y. W. Liu,[62a] J. Llorente Merino,[142] S. L. Lloyd,[94] E. M. Lobodzinska,[48] P. Loch,[7] S. Loffredo,[76a,76b] T. Lohse,[18] K. Lohwasser,[139] E. Loiacono,[48] M. Lokajicek,[131,a] J. D. Lomas,[20] J. D. Long,[162] I. Longarini,[160] L. Longo,[70a,70b] R. Longo,[162] I. Lopez Paz,[67] A. Lopez Solis,[48] J. Lorenz,[109] N. Lorenzo Martinez,[4] A. M. Lory,[109] G. Löschcke Centeno,[146] O. Loseva,[37] X. Lou,[47a,47b] X. Lou,[14a,14e] A. Lounis,[66] J. Love,[6]

P. A. Love,[91] G. Lu,[14a,14e] M. Lu,[80] S. Lu,[128] Y. J. Lu,[65] H. J. Lubatti,[138] C. Luci,[75a,75b] F. L. Lucio Alves,[14c] A. Lucotte,[60] F. Luehring,[68] I. Luise,[145] O. Lukianchuk,[66] O. Lundberg,[144] B. Lund-Jensen,[144] N. A. Luongo,[123] M. S. Lutz,[151] D. Lynn,[29] H. Lyons,[92] R. Lysak,[131] E. Lytken,[98] V. Lyubushkin,[38] T. Lyubushkina,[38] M. M. Lyukova,[145] H. Ma,[29] K. Ma,[62a] L. L. Ma,[62b] Y. Ma,[121] D. M. Mac Donell,[165] G. Maccarrone,[53] J. C. MacDonald,[100] P. C. Machado De Abreu Farias,[83b] R. Madar,[40] W. F. Mader,[50] T. Madula,[96] J. Maeda,[85] T. Maeno,[29] M. Maerker,[50] H. Maguire,[139] V. Maiboroda,[135] A. Maio,[130a,130b,130d] K. Maj,[86a] O. Majersky,[48] S. Majewski,[123] N. Makovec,[66] V. Maksimovic,[15] B. Malaescu,[127] Pa. Malecki,[87] V. P. Maleev,[37] F. Malek,[60] M. Mali,[93] D. Malito,[95] U. Mallik,[80] S. Maltezos,[10] S. Malyukov,[38] J. Mamuzic,[13] G. Mancini,[53] G. Manco,[73a,73b] J. P. Mandalia,[94] I. Mandić,[93] L. Manhaes de Andrade Filho,[83a] I. M. Maniatis,[169] J. Manjarres Ramos,[102,ee] D. C. Mankad,[169] A. Mann,[109] B. Mansoulie,[135] S. Manzoni,[36] A. Marantis,[152,cc] G. Marchiori,[5] M. Marcisovsky,[131] C. Marcon,[71a] M. Marinescu,[20] M. Marjanovic,[120] E. J. Marshall,[91] Z. Marshall,[17a] S. Marti-Garcia,[163] T. A. Martin,[167] V. J. Martin,[52] B. Martin dit Latour,[16] L. Martinelli,[75a,75b] M. Martinez,[13,w] P. Martinez Agullo,[163] V. I. Martinez Outschoorn,[103] P. Martinez Suarez,[13] S. Martin-Haugh,[134] V. S. Martoiu,[27b] A. C. Martyniuk,[96] A. Marzin,[36] D. Mascione,[78a,78b] L. Masetti,[100] T. Mashimo,[153] J. Masik,[101] A. L. Maslennikov,[37] L. Massa,[23b] P. Massarotti,[72a,72b] P. Mastrandrea,[74a,74b] A. Mastroberardino,[43b,43a] T. Masubuchi,[153] T. Mathisen,[161] J. Matousek,[133] N. Matsuzawa,[153] J. Maurer,[27b] B. Maček,[93] D. A. Maximov,[37] R. Mazini,[148] I. Maznas,[152] M. Mazza,[107] S. M. Mazza,[136] E. Mazzeo,[71a,71b] C. Mc Ginn,[29] J. P. Mc Gowan,[104] S. P. Mc Kee,[106] E. F. McDonald,[105] A. E. McDougall,[114] J. A. Mcfayden,[146] R. P. McGovern,[128] G. Mchedlidze,[149b] R. P. Mckenzie,[33g] T. C. Mclachlan,[48] D. J. Mclaughlin,[96] K. D. McLean,[165] S. J. McMahon,[134] P. C. McNamara,[105] C. M. Mcpartland,[92] R. A. McPherson,[165,p] S. Mehlhase,[109] A. Mehta,[92] D. Melini,[150] B. R. Mellado Garcia,[33g] A. H. Melo,[55] F. Meloni,[48] A. M. Mendes Jacques Da Costa,[101] H. Y. Meng,[155] L. Meng,[91] S. Menke,[110] M. Mentink,[36] E. Meoni,[43b,43a] C. Merlassino,[126] L. Merola,[72a,72b] C. Meroni,[71a,71b] G. Merz,[106] O. Meshkov,[37] J. Metcalfe,[6] A. S. Mete,[6] C. Meyer,[68] J-P. Meyer,[135] R. P. Middleton,[134] L. Mijović,[52] G. Mikenberg,[169] M. Mikestikova,[131] M. Mikuž,[93] H. Mildner,[100] A. Milic,[36] C. D. Milke,[44] D. W. Miller,[39] L. S. Miller,[34] A. Milov,[169] D. A. Milstead,[47a,47b] T. Min,[14c] A. A. Minaenko,[37] I. A. Minashvili,[149b] L. Mince,[59] A. I. Mincer,[117] B. Mindur,[86a] M. Mineev,[38] Y. Mino,[88] L. M. Mir,[13] M. Miralles Lopez,[163] M. Mironova,[17a] A. Mishima,[153] M. C. Missio,[113] A. Mitra,[167] V. A. Mitsou,[163] Y. Mitsumori,[111] O. Miu,[155] P. S. Miyagawa,[94] T. Mkrtchyan,[63a] M. Mlinarevic,[96] T. Mlinarevic,[96] M. Mlynarikova,[36] S. Mobius,[19] P. Moder,[48] P. Mogg,[109] A. F. Mohammed,[14a,14e] S. Mohapatra,[41] G. Mokgatitswane,[33g] L. Moleri,[169] B. Mondal,[141] S. Mondal,[132] K. Mönig,[48] E. Monnier,[102] L. Monsonis Romero,[163] J. Montejo Berlingen,[13] M. Montella,[119] F. Montereali,[77a,77b] F. Monticelli,[90] S. Monzani,[69a,69c] N. Morange,[66] A. L. Moreira De Carvalho,[130a] M. Moreno Llácer,[163] C. Moreno Martinez,[56] P. Morettini,[57b] S. Morgenstern,[36] M. Morii,[61] M. Morinaga,[153] A. K. Morley,[36] F. Morodei,[75a,75b] L. Morvaj,[36] P. Moschovakos,[36] B. Moser,[36] M. Mosidze,[149b] T. Moskalets,[54] P. Moskvitina,[113] J. Moss,[31,ff] E. J. W. Moyse,[103] O. Mtintsilana,[33g] S. Muanza,[102] J. Mueller,[129] D. Muenstermann,[91] R. Müller,[19] G. A. Mullier,[161] A. J. Mullin,[32] J. J. Mullin,[128] D. P. Mungo,[155] D. Munoz Perez,[163] F. J. Munoz Sanchez,[101] M. Murin,[101] W. J. Murray,[167,134] A. Murrone,[71a,71b] J. M. Muse,[120] M. Muškinja,[17a] C. Mwewa,[29] A. G. Myagkov,[37,l] A. J. Myers,[8] A. A. Myers,[129] G. Myers,[68] M. Myska,[132] B. P. Nachman,[17a] O. Nackenhorst,[49] A. Nag,[50] K. Nagai,[126] K. Nagano,[84] J. L. Nagle,[29,i] E. Nagy,[102] A. M. Nairz,[36] Y. Nakahama,[84] K. Nakamura,[84] K. Nakkalil,[5] H. Nanjo,[124] R. Narayan,[44] E. A. Narayanan,[112] I. Naryshkin,[37] M. Naseri,[34] S. Nasri,[159] C. Nass,[24] G. Navarro,[22a] J. Navarro-Gonzalez,[163] R. Nayak,[151] A. Nayaz,[18] P. Y. Nechaeva,[37] F. Nechansky,[48] L. Nedic,[126] T. J. Neep,[20] A. Negri,[73a,73b] M. Negrini,[23b] C. Nellist,[114] C. Nelson,[104] K. Nelson,[106] S. Nemecek,[131] M. Nessi,[36,gg] M. S. Neubauer,[162] F. Neuhaus,[100] J. Neundorf,[48] R. Newhouse,[164] P. R. Newman,[20] C. W. Ng,[129] Y. W. Y. Ng,[48] B. Ngair,[35e] H. D. N. Nguyen,[108] R. B. Nickerson,[126] R. Nicolaidou,[135] J. Nielsen,[136] M. Niemeyer,[55] J. Niermann,[55,36] N. Nikiforou,[36] V. Nikolaenko,[37,l] I. Nikolic-Audit,[127] K. Nikolopoulos,[20] P. Nilsson,[29] I. Ninca,[48] H. R. Nindhito,[56] G. Ninio,[151] A. Nisati,[75a] N. Nishu,[2] R. Nisius,[110] J-E. Nitschke,[50] E. K. Nkadimeng,[33g] T. Nobe,[153] D. L. Noel,[32] T. Nommensen,[147] M. B. Norfolk,[139] R. R. B. Norisam,[96] B. J. Norman,[34] J. Novak,[93] T. Novak,[48] L. Novotny,[132] R. Novotny,[112] L. Nozka,[122] K. Ntekas,[160] N. M. J. Nunes De Moura Junior,[83b] E. Nurse,[96] J. Ocariz,[127] A. Ochi,[85] I. Ochoa,[130a]

S. Oerdek,[48,hh] J. T. Offermann,[39] A. Ogrodnik,[133] A. Oh,[101] C. C. Ohm,[144] H. Oide,[84] R. Oishi,[153] M. L. Ojeda,[48] M. W. O'Keefe,[92] Y. Okumura,[153] L. F. Oleiro Seabra,[130a] S. A. Olivares Pino,[137d] D. Oliveira Damazio,[29] D. Oliveira Goncalves,[83a] J. L. Oliver,[160] A. Olszewski,[87] Ö. O. Öncel,[54] A. P. O'Neill,[19] A. Onofre,[130a,130e] P. U. E. Onyisi,[11] M. J. Oreglia,[39] G. E. Orellana,[90] D. Orestano,[77a,77b] N. Orlando,[13] R. S. Orr,[155] V. O'Shea,[59] L. M. Osojnak,[128] R. Ospanov,[62a] G. Otero y Garzon,[30] H. Otono,[89] P. S. Ott,[63a] G. J. Ottino,[17a] M. Ouchrif,[35d] J. Ouellette,[29] F. Ould-Saada,[125] M. Owen,[59] R. E. Owen,[134] K. Y. Oyulmaz,[21a] V. E. Ozcan,[21a] N. Ozturk,[8] S. Ozturk,[82] H. A. Pacey,[126] A. Pacheco Pages,[13] C. Padilla Aranda,[13] G. Padovano,[75a,75b] S. Pagan Griso,[17a] G. Palacino,[68] A. Palazzo,[70a,70b] S. Palestini,[36] J. Pan,[172] T. Pan,[64a] D. K. Panchal,[11] C. E. Pandini,[114] J. G. Panduro Vazquez,[95] H. D. Pandya,[1] H. Pang,[14b] P. Pani,[48] G. Panizzo,[69a,69c] L. Paolozzi,[56] C. Papadatos,[108] S. Parajuli,[44] A. Paramonov,[6] C. Paraskevopoulos,[10] D. Paredes Hernandez,[64b] T. H. Park,[155] M. A. Parker,[32] F. Parodi,[57b,57a] E. W. Parrish,[115] V. A. Parrish,[52] J. A. Parsons,[41] U. Parzefall,[54] B. Pascual Dias,[108] L. Pascual Dominguez,[151] E. Pasqualucci,[75a] S. Passaggio,[57b] F. Pastore,[95] P. Pasuwan,[47a,47b] P. Patel,[87] U. M. Patel,[51] J. R. Pater,[101] T. Pauly,[36] J. Pearkes,[143] M. Pedersen,[125] R. Pedro,[130a] S. V. Peleganchuk,[37] O. Penc,[36] E. A. Pender,[52] H. Peng,[62a] K. E. Penski,[109] M. Penzin,[37] B. S. Peralva,[83d] A. P. Pereira Peixoto,[60] L. Pereira Sanchez,[47a,47b] D. V. Perepelitsa,[29,i] E. Perez Codina,[156a] M. Perganti,[10] L. Perini,[71a,71b,a] H. Pernegger,[36] O. Perrin,[40] K. Peters,[48] R. F. Y. Peters,[101] B. A. Petersen,[36] T. C. Petersen,[42] E. Petit,[102] V. Petousis,[132] C. Petridou,[152,bb] A. Petrukhin,[141] M. Pettee,[17a] N. E. Pettersson,[36] A. Petukhov,[37] K. Petukhova,[133] R. Pezoa,[137f] L. Pezzotti,[36] G. Pezzullo,[172] T. M. Pham,[170] T. Pham,[105] P. W. Phillips,[134] G. Piacquadio,[145] E. Pianori,[17a] F. Piazza,[71a,71b] R. Piegaia,[30] D. Pietreanu,[27b] A. D. Pilkington,[101] M. Pinamonti,[69a,69c] J. L. Pinfold,[2] B. C. Pinheiro Pereira,[130a] A. E. Pinto Pinoargote,[100,135] L. Pintucci,[69a,69c] K. M. Piper,[146] A. Pirttikoski,[56] D. A. Pizzi,[34] L. Pizzimento,[64b] A. Pizzini,[114] M.-A. Pleier,[29] V. Plesanovs,[54] V. Pleskot,[133] E. Plotnikova,[38] G. Poddar,[4] R. Poettgen,[98] L. Poggioli,[127] I. Pokharel,[55] S. Polacek,[133] G. Polesello,[73a] A. Poley,[142,156a] R. Polifka,[132] A. Polini,[23b] C. S. Pollard,[167] Z. B. Pollock,[119] V. Polychronakos,[29] E. Pompa Pacchi,[75a,75b] D. Ponomarenko,[113] L. Pontecorvo,[36] S. Popa,[27a] G. A. Popeneciu,[27d] A. Poreba,[36] D. M. Portillo Quintero,[156a] S. Pospisil,[132] M. A. Postill,[139] P. Postolache,[27c] K. Potamianos,[167] P. A. Potepa,[86a] I. N. Potrap,[38] C. J. Potter,[32] H. Potti,[1] T. Poulsen,[48] J. Poveda,[163] M. E. Pozo Astigarraga,[36] A. Prades Ibanez,[163] J. Pretel,[54] D. Price,[101] M. Primavera,[70a] M. A. Principe Martin,[99] R. Privara,[122] T. Procter,[59] M. L. Proffitt,[138] N. Proklova,[128] K. Prokofiev,[64c] G. Proto,[110] S. Protopopescu,[29] J. Proudfoot,[6] M. Przybycien,[86a] W. W. Przygoda,[86b] J. E. Puddefoot,[139] D. Pudzha,[37] D. Pyatiizbyantseva,[37] J. Qian,[106] D. Qichen,[101] Y. Qin,[101] T. Qiu,[52] A. Quadt,[55] M. Queitsch-Maitland,[101] G. Quetant,[56] R. P. Quinn,[164] G. Rabanal Bolanos,[61] D. Rafanoharana,[54] F. Ragusa,[71a,71b] J. L. Rainbolt,[39] J. A. Raine,[56] S. Rajagopalan,[29] E. Ramakoti,[37] K. Ran,[48,14e] N. P. Rapheeha,[33g] H. Rasheed,[27b] V. Raskina,[127] D. F. Rassloff,[63a] S. Rave,[100] B. Ravina,[55] I. Ravinovich,[169] M. Raymond,[36] A. L. Read,[125] N. P. Readioff,[139] D. M. Rebuzzi,[73a,73b] G. Redlinger,[29] A. S. Reed,[110] K. Reeves,[26] J. A. Reidelsturz,[171] D. Reikher,[151] A. Rej,[141] C. Rembser,[36] A. Renardi,[48] M. Renda,[27b] M. B. Rendel,[110] F. Renner,[48] A. G. Rennie,[160] A. L. Rescia,[48] S. Resconi,[71a] M. Ressegotti,[57b,57a] S. Rettie,[36] J. G. Reyes Rivera,[107] E. Reynolds,[17a] O. L. Rezanova,[37] P. Reznicek,[133] N. Ribaric,[91] E. Ricci,[78a,78b] R. Richter,[110] S. Richter,[47a,47b] E. Richter-Was,[86b] M. Ridel,[127] S. Ridouani,[35d] P. Rieck,[117] P. Riedler,[36] E. M. Riefel,[47a,47b] M. Rijssenbeek,[145] A. Rimoldi,[73a,73b] M. Rimoldi,[48] L. Rinaldi,[23b,23a] T. T. Rinn,[29] M. P. Rinnagel,[109] G. Ripellino,[161] I. Riu,[13] P. Rivadeneira,[48] J. C. Rivera Vergara,[165] F. Rizatdinova,[121] E. Rizvi,[94] B. A. Roberts,[167] B. R. Roberts,[17a] S. H. Robertson,[104,p] D. Robinson,[32] C. M. Robles Gajardo,[137f] M. Robles Manzano,[100] A. Robson,[59] A. Rocchi,[76a,76b] C. Roda,[74a,74b] S. Rodriguez Bosca,[63a] Y. Rodriguez Garcia,[22a] A. Rodriguez Rodriguez,[54] A. M. Rodríguez Vera,[156b] S. Roe,[36] J. T. Roemer,[160] A. R. Roepe-Gier,[136] J. Roggel,[171] O. Røhne,[125] R. A. Rojas,[103] C. P. A. Roland,[68] J. Roloff,[29] A. Romaniouk,[37] E. Romano,[73a,73b] M. Romano,[23b] A. C. Romero Hernandez,[162] N. Rompotis,[92] L. Roos,[127] S. Rosati,[75a] B. J. Rosser,[39] E. Rossi,[126] E. Rossi,[72a,72b] L. P. Rossi,[57b] L. Rossini,[54] R. Rosten,[119] M. Rotaru,[27b] B. Rottler,[54] C. Rougier,[102,ee] D. Rousseau,[66] D. Rousso,[32] A. Roy,[162] S. Roy-Garand,[155] A. Rozanov,[102] Y. Rozen,[150] X. Ruan,[33g] A. Rubio Jimenez,[163] A. J. Ruby,[92] V. H. Ruelas Rivera,[18] T. A. Ruggeri,[1] A. Ruggiero,[126] A. Ruiz-Martinez,[163] A. Rummler,[36] Z. Rurikova,[54] N. A. Rusakovich,[38] H. L. Russell,[165] G. Russo,[75a,75b] J. P. Rutherfoord,[7] S. Rutherford Colmenares,[32] K. Rybacki,[91] M. Rybar,[133]

E. B. Rye,[125] A. Ryzhov,[44] J. A. Sabater Iglesias,[56] P. Sabatini,[163] L. Sabetta,[75a,75b] H. F-W. Sadrozinski,[136] F. Safai Tehrani,[75a] B. Safarzadeh Samani,[146] M. Safdari,[143] S. Saha,[165] M. Sahinsoy,[110] M. Saimpert,[135] M. Saito,[153] T. Saito,[153] D. Salamani,[36] A. Salnikov,[143] J. Salt,[163] A. Salvador Salas,[13] D. Salvatore,[43b,43a] F. Salvatore,[146] A. Salzburger,[36] D. Sammel,[54] D. Sampsonidis,[152,bb] D. Sampsonidou,[123] J. Sánchez,[163] A. Sanchez Pineda,[4] V. Sanchez Sebastian,[163] H. Sandaker,[125] C. O. Sander,[48] J. A. Sandesara,[103] M. Sandhoff,[171] C. Sandoval,[22b] D. P. C. Sankey,[134] T. Sano,[88] A. Sansoni,[53] L. Santi,[75a,75b] C. Santoni,[40] H. Santos,[130a,130b] S. N. Santpur,[17a] A. Santra,[169] K. A. Saoucha,[116b] J. G. Saraiva,[130a,130d] J. Sardain,[7] O. Sasaki,[84] K. Sato,[157] C. Sauer,[63b] F. Sauerburger,[54] E. Sauvan,[4] P. Savard,[155,e] R. Sawada,[153] C. Sawyer,[134] L. Sawyer,[97] I. Sayago Galvan,[163] C. Sbarra,[23b] A. Sbrizzi,[23b,23a] T. Scanlon,[96] J. Schaarschmidt,[138] P. Schacht,[110] D. Schaefer,[39] U. Schäfer,[100] A. C. Schaffer,[66,44] D. Schaile,[109] R. D. Schamberger,[145] C. Scharf,[18] M. M. Schefer,[19] V. A. Schegelsky,[37] D. Scheirich,[133] F. Schenck,[18] M. Schernau,[160] C. Scheulen,[55] C. Schiavi,[57b,57a] E. J. Schioppa,[70a,70b] M. Schioppa,[43b,43a] B. Schlag,[143,u] K. E. Schleicher,[54] S. Schlenker,[36] J. Schmeing,[171] M. A. Schmidt,[171] K. Schmieden,[100] C. Schmitt,[100] S. Schmitt,[48] L. Schoeffel,[135] A. Schoening,[63b] P. G. Scholer,[54] E. Schopf,[126] M. Schott,[100] J. Schovancova,[36] S. Schramm,[56] F. Schroeder,[171] T. Schroer,[56] H-C. Schultz-Coulon,[63a] M. Schumacher,[54] B. A. Schumm,[136] Ph. Schune,[135] A. J. Schuy,[138] H. R. Schwartz,[136] A. Schwartzman,[143] T. A. Schwarz,[106] Ph. Schwemling,[135] R. Schwienhorst,[107] A. Sciandra,[136] G. Sciolla,[26] F. Scuri,[74a] C. D. Sebastiani,[92] K. Sedlaczek,[115] P. Seema,[18] S. C. Seidel,[112] A. Seiden,[136] B. D. Seidlitz,[41] C. Seitz,[48] J. M. Seixas,[83b] G. Sekhniaidze,[72a] S. J. Sekula,[44] L. Selem,[60] N. Semprini-Cesari,[23b,23a] D. Sengupta,[56] V. Senthilkumar,[163] L. Serin,[66] L. Serkin,[69a,69b] M. Sessa,[76a,76b] H. Severini,[120] F. Sforza,[57b,57a] A. Sfyrla,[56] E. Shabalina,[55] R. Shaheen,[144] J. D. Shahinian,[128] D. Shaked Renous,[169] L. Y. Shan,[14a] M. Shapiro,[17a] A. Sharma,[36] A. S. Sharma,[164] P. Sharma,[80] S. Sharma,[48] P. B. Shatalov,[37] K. Shaw,[146] S. M. Shaw,[101] A. Shcherbakova,[37] Q. Shen,[62c,5] P. Sherwood,[96] L. Shi,[96] X. Shi,[14a] C. O. Shimmin,[172] J. D. Shinner,[95] I. P. J. Shipsey,[126] S. Shirabe,[56,gg] M. Shiyakova,[38,ii] J. Shlomi,[169] M. J. Shochet,[39] J. Shojaii,[105] D. R. Shope,[125] B. Shrestha,[120] S. Shrestha,[119,jj] E. M. Shrif,[33g] M. J. Shroff,[165] P. Sicho,[131] A. M. Sickles,[162] E. Sideras Haddad,[33g] A. Sidoti,[23b] F. Siegert,[50] Dj. Sijacki,[15] R. Sikora,[86a] F. Sili,[90] J. M. Silva,[20] M. V. Silva Oliveira,[29] S. B. Silverstein,[47a] S. Simion,[66] R. Simoniello,[36] E. L. Simpson,[59] H. Simpson,[146] L. R. Simpson,[106] N. D. Simpson,[98] S. Simsek,[82] S. Sindhu,[55] P. Sinervo,[155] S. Singh,[155] S. Sinha,[48] S. Sinha,[101] M. Sioli,[23b,23a] I. Siral,[36] E. Sitnikova,[48] S. Yu. Sivoklokov,[37,a] J. Sjölin,[47a,47b] A. Skaf,[55] E. Skorda,[20] P. Skubic,[120] M. Slawinska,[87] V. Smakhtin,[169] B. H. Smart,[134] J. Smiesko,[36] S. Yu. Smirnov,[37] Y. Smirnov,[37] L. N. Smirnova,[37,l] O. Smirnova,[98] A. C. Smith,[41] E. A. Smith,[39] H. A. Smith,[126] J. L. Smith,[92] R. Smith,[143] M. Smizanska,[91] K. Smolek,[132] A. A. Snesarev,[37] S. R. Snider,[155] H. L. Snoek,[114] S. Snyder,[29] R. Sobie,[165,p] A. Soffer,[151] C. A. Solans Sanchez,[36] E. Yu. Soldatov,[37] U. Soldevila,[163] A. A. Solodkov,[37] S. Solomon,[26] A. Soloshenko,[38] K. Solovieva,[54] O. V. Solovyanov,[40] V. Solovyev,[37] P. Sommer,[36] A. Sonay,[13] W. Y. Song,[156b] J. M. Sonneveld,[114] A. Sopczak,[132] A. L. Sopio,[96] F. Sopkova,[28b] V. Sothilingam,[63a] S. Sottocornola,[68] R. Soualah,[116b] Z. Soumaimi,[35e] D. South,[48] N. Soybelman,[169] S. Spagnolo,[70a,70b] M. Spalla,[110] D. Sperlich,[54] G. Spigo,[36] S. Spinali,[91] D. P. Spiteri,[59] M. Spousta,[133] E. J. Staats,[34] A. Stabile,[71a,71b] R. Stamen,[63a] A. Stampekis,[20] M. Standke,[24] E. Stanecka,[87] M. V. Stange,[50] B. Stanislaus,[17a] M. M. Stanitzki,[48] B. Stapf,[48] E. A. Starchenko,[37] G. H. Stark,[136] J. Stark,[102,ee] D. M. Starko,[156b] P. Staroba,[131] P. Starovoitov,[63a] S. Stärz,[104] R. Staszewski,[87] G. Stavropoulos,[46] J. Steentoft,[161] P. Steinberg,[29] B. Stelzer,[142,156a] H. J. Stelzer,[129] O. Stelzer-Chilton,[156a] H. Stenzel,[58] T. J. Stevenson,[146] G. A. Stewart,[36] J. R. Stewart,[121] M. C. Stockton,[36] G. Stoicea,[27b] M. Stolarski,[130a] S. Stonjek,[110] A. Straessner,[50] J. Strandberg,[144] S. Strandberg,[47a,47b] M. Stratmann,[171] M. Strauss,[120] T. Strebler,[102] P. Strizenec,[28b] R. Ströhmer,[166] D. M. Strom,[123] L. R. Strom,[48] R. Stroynowski,[44] A. Strubig,[47a,47b] S. A. Stucci,[29] B. Stugu,[16] J. Stupak,[120] N. A. Styles,[48] D. Su,[143] S. Su,[62a] W. Su,[62d] X. Su,[62a,66] K. Sugizaki,[153] V. V. Sulin,[37] M. J. Sullivan,[92] D. M. S. Sultan,[78a,78b] L. Sultanaliyeva,[37] S. Sultansoy,[3b] T. Sumida,[88] S. Sun,[106] S. Sun,[170] O. Sunneborn Gudnadottir,[161] N. Sur,[102] M. R. Sutton,[146] H. Suzuki,[157] M. Svatos,[131] M. Swiatlowski,[156a] T. Swirski,[166] I. Sykora,[28a] M. Sykora,[133] T. Sykora,[133] D. Ta,[100] K. Tackmann,[48,hh] A. Taffard,[160] R. Tafirout,[156a] J. S. Tafoya Vargas,[66] E. P. Takeva,[52] Y. Takubo,[84] M. Talby,[102] A. A. Talyshev,[37] K. C. Tam,[64b] N. M. Tamir,[151] A. Tanaka,[153] J. Tanaka,[153] R. Tanaka,[66] M. Tanasini,[57b,57a]

Z. Tao,[164] S. Tapia Araya,[137f] S. Tapprogge,[100] A. Tarek Abouelfadl Mohamed,[107] S. Tarem,[150] K. Tariq,[14a] G. Tarna,[102,27b] G. F. Tartarelli,[71a] P. Tas,[133] M. Tasevsky,[131] E. Tassi,[43b,43a] A. C. Tate,[162] G. Tateno,[153] Y. Tayalati,[35e,kk] G. N. Taylor,[105] W. Taylor,[156b] H. Teagle,[92] A. S. Tee,[170] R. Teixeira De Lima,[143] P. Teixeira-Dias,[95] J. J. Teoh,[155] K. Terashi,[153] J. Terron,[99] S. Terzo,[13] M. Testa,[53] R. J. Teuscher,[155,p] A. Thaler,[79] O. Theiner,[56] N. Themistokleous,[52] T. Theveneaux-Pelzer,[102] O. Thielmann,[171] D. W. Thomas,[95] J. P. Thomas,[20] E. A. Thompson,[17a] P. D. Thompson,[20] E. Thomson,[128] Y. Tian,[55] V. Tikhomirov,[37,l] Yu. A. Tikhonov,[37] S. Timoshenko,[37] D. Timoshyn,[133] E. X. L. Ting,[1] P. Tipton,[172] S. H. Tlou,[33g] A. Tnourji,[40] K. Todome,[154] S. Todorova-Nova,[133] S. Todt,[50] M. Togawa,[84] J. Tojo,[89] S. Tokár,[28a] K. Tokushuku,[84] O. Toldaiev,[68] R. Tombs,[32] M. Tomoto,[84,111] L. Tompkins,[143,u] K. W. Topolnicki,[86b] E. Torrence,[123] H. Torres,[102,ee] E. Torró Pastor,[163] M. Toscani,[30] C. Tosciri,[39] M. Tost,[11] D. R. Tovey,[139] A. Traeet,[16] I. S. Trandafir,[27b] T. Trefzger,[166] A. Tricoli,[29] I. M. Trigger,[156a] S. Trincaz-Duvoid,[127] D. A. Trischuk,[26] B. Trocmé,[60] C. Troncon,[71a] L. Truong,[33c] M. Trzebinski,[87] A. Trzupek,[87] F. Tsai,[145] M. Tsai,[106] A. Tsiamis,[152,bb] P. V. Tsiareshka,[37] S. Tsigaridas,[156a] A. Tsirigotis,[152,cc] V. Tsiskaridze,[155] E. G. Tskhadadze,[149a] M. Tsopoulou,[152,bb] Y. Tsujikawa,[88] I. I. Tsukerman,[37] V. Tsulaia,[17a] S. Tsuno,[84] O. Tsur,[150] K. Tsuri,[118] D. Tsybychev,[145] Y. Tu,[64b] A. Tudorache,[27b] V. Tudorache,[27b] A. N. Tuna,[36] S. Turchikhin,[57b,57a] I. Turk Cakir,[3a] R. Turra,[71a] T. Turtuvshin,[38,ll] P. M. Tuts,[41] S. Tzamarias,[152,bb] P. Tzanis,[10] E. Tzovara,[100] F. Ukegawa,[157] P. A. Ulloa Poblete,[137c,137b] E. N. Umaka,[29] G. Unal,[36] M. Unal,[11] A. Undrus,[29] G. Unel,[160] J. Urban,[28b] P. Urquijo,[105] G. Usai,[8] R. Ushioda,[154] M. Usman,[108] Z. Uysal,[21b] L. Vacavant,[102] V. Vacek,[132] B. Vachon,[104] K. O. H. Vadla,[125] T. Vafeiadis,[36] A. Vaitkus,[96] C. Valderanis,[109] E. Valdes Santurio,[47a,47b] M. Valente,[156a] S. Valentinetti,[23b,23a] A. Valero,[163] E. Valiente Moreno,[163] A. Vallier,[102,ee] J. A. Valls Ferrer,[163] D. R. Van Arneman,[114] T. R. Van Daalen,[138] A. Van Der Graaf,[49] P. Van Gemmeren,[6] M. Van Rijnbach,[125,36] S. Van Stroud,[96] I. Van Vulpen,[114] M. Vanadia,[76a,76b] W. Vandelli,[36] M. Vandenbroucke,[135] E. R. Vandewall,[121] D. Vannicola,[151] L. Vannoli,[57b,57a] R. Vari,[75a] E. W. Varnes,[7] C. Varni,[17b] T. Varol,[148] D. Varouchas,[66] L. Varriale,[163] K. E. Varvell,[147] M. E. Vasile,[27b] L. Vaslin,[40] G. A. Vasquez,[165] A. Vasyukov,[38] F. Vazeille,[40] T. Vazquez Schroeder,[36] J. Veatch,[31] V. Vecchio,[101] M. J. Veen,[103] I. Veliscek,[126] L. M. Veloce,[155] F. Veloso,[130a,130c] S. Veneziano,[75a] A. Ventura,[70a,70b] S. Ventura Gonzalez,[135] A. Verbytskyi,[110] M. Verducci,[74a,74b] C. Vergis,[24] M. Verissimo De Araujo,[83b] W. Verkerke,[114] J. C. Vermeulen,[114] C. Vernieri,[143] M. Vessella,[103] M. C. Vetterli,[142,e] A. Vgenopoulos,[152,bb] N. Viaux Maira,[137f] T. Vickey,[139] O. E. Vickey Boeriu,[139] G. H. A. Viehhauser,[126] L. Vigani,[63b] M. Villa,[23b,23a] M. Villaplana Perez,[163] E. M. Villhauer,[52] E. Vilucchi,[53] M. G. Vincter,[34] G. S. Virdee,[20] A. Vishwakarma,[52] A. Visibile,[114] C. Vittori,[36] I. Vivarelli,[146] V. Vladimirov,[167] E. Voevodina,[110] F. Vogel,[109] P. Vokac,[132] Yu. Volkotrub,[86a] J. Von Ahnen,[48] E. Von Toerne,[24] B. Vormwald,[36] V. Vorobel,[133] K. Vorobev,[37] M. Vos,[163] K. Voss,[141] J. H. Vossebeld,[92] M. Vozak,[114] L. Vozdecky,[94] N. Vranjes,[15] M. Vranjes Milosavljevic,[15] M. Vreeswijk,[114] R. Vuillermet,[36] O. Vujinovic,[100] I. Vukotic,[39] S. Wada,[157] C. Wagner,[103] J. M. Wagner,[17a] W. Wagner,[171] S. Wahdan,[171] H. Wahlberg,[90] M. Wakida,[111] J. Walder,[134] R. Walker,[109] W. Walkowiak,[141] A. Wall,[128] T. Wamorkar,[6] A. Z. Wang,[170] C. Wang,[100] C. Wang,[62c] H. Wang,[17a] J. Wang,[64a] R.-J. Wang,[100] R. Wang,[61] R. Wang,[6] S. M. Wang,[148] S. Wang,[62b] T. Wang,[62a] W. T. Wang,[80] W. Wang,[14a] X. Wang,[14c] X. Wang,[162] X. Wang,[62c] Y. Wang,[62d] Y. Wang,[14c] Z. Wang,[106] Z. Wang,[62d,51,62c] Z. Wang,[106] A. Warburton,[104] R. J. Ward,[20] N. Warrack,[59] A. T. Watson,[20] H. Watson,[59] M. F. Watson,[20] E. Watton,[59,134] G. Watts,[138] B. M. Waugh,[96] C. Weber,[29] H. A. Weber,[18] M. S. Weber,[19] S. M. Weber,[63a] C. Wei,[62a] Y. Wei,[126] A. R. Weidberg,[126] E. J. Weik,[117] J. Weingarten,[49] M. Weirich,[100] C. Weiser,[54] C. J. Wells,[48] T. Wenaus,[29] B. Wendland,[49] T. Wengler,[36] N. S. Wenke,[110] N. Wermes,[24] M. Wessels,[63a] A. M. Wharton,[91] A. S. White,[61] A. White,[8] M. J. White,[1] D. Whiteson,[160] L. Wickremasinghe,[124] W. Wiedenmann,[170] C. Wiel,[50] M. Wielers,[134] C. Wiglesworth,[42] D. J. Wilbern,[120] H. G. Wilkens,[36] D. M. Williams,[41] H. H. Williams,[128] S. Williams,[32] S. Willocq,[103] B. J. Wilson,[101] P. J. Windischhofer,[39] F. I. Winkel,[30] F. Winklmeier,[123] B. T. Winter,[54] J. K. Winter,[101] M. Wittgen,[143] M. Wobisch,[97] Z. Wolffs,[114] J. Wollrath,[160] M. W. Wolter,[87] H. Wolters,[130a,130c] A. F. Wongel,[48] S. D. Worm,[48] B. K. Wosiek,[87] K. W. Woźniak,[87] S. Wozniewski,[55] K. Wraight,[59] C. Wu,[20] J. Wu,[14a,14e] M. Wu,[64a] M. Wu,[113] S. L. Wu,[170] X. Wu,[56] Y. Wu,[62a] Z. Wu,[135] J. Wuerzinger,[110,x] T. R. Wyatt,[101] B. M. Wynne,[52] S. Xella,[42] L. Xia,[14c] M. Xia,[14b] J. Xiang,[64c] M. Xie,[62a] X. Xie,[62a] S. Xin,[14a,14e] J. Xiong,[17a] D. Xu,[14a] H. Xu,[62a]

L. Xu,[62a] R. Xu,[128] T. Xu,[106] Y. Xu,[14b] Z. Xu,[52] Z. Xu,[14a] B. Yabsley,[147] S. Yacoob,[33a] Y. Yamaguchi,[154] E. Yamashita,[153] H. Yamauchi,[157] T. Yamazaki,[17a] Y. Yamazaki,[85] J. Yan,[62c] S. Yan,[126] Z. Yan,[25] H. J. Yang,[62c,62d] H. T. Yang,[62a] S. Yang,[62a] T. Yang,[64c] X. Yang,[62a] X. Yang,[14a] Y. Yang,[44] Y. Yang,[62a] Z. Yang,[62a] W-M. Yao,[17a] Y. C. Yap,[48] H. Ye,[14c] H. Ye,[55] J. Ye,[14a] S. Ye,[29] X. Ye,[62a] Y. Yeh,[96] I. Yeletskikh,[38] B. K. Yeo,[17b] M. R. Yexley,[96] P. Yin,[41] K. Yorita,[168] S. Younas,[27b] C. J. S. Young,[36] C. Young,[143] C. Yu,[14a,14e] Y. Yu,[62a] M. Yuan,[106] R. Yuan,[62b,mm] L. Yue,[96] M. Zaazoua,[62a] B. Zabinski,[87] E. Zaid,[52] T. Zakareishvili,[149b] N. Zakharchuk,[34] S. Zambito,[56] J. A. Zamora Saa,[137d,137b] J. Zang,[153] D. Zanzi,[54] O. Zaplatilek,[132] C. Zeitnitz,[171] H. Zeng,[14a] J. C. Zeng,[162] D. T. Zenger Jr.,[26] O. Zenin,[37] T. Ženiš,[28a] S. Zenz,[94] S. Zerradi,[35a] D. Zerwas,[66] M. Zhai,[14a,14e] B. Zhang,[14c] D. F. Zhang,[139] J. Zhang,[62b] J. Zhang,[6] K. Zhang,[14a,14e] L. Zhang,[14c] P. Zhang,[14a,14e] R. Zhang,[170] S. Zhang,[106] T. Zhang,[153] X. Zhang,[62c] X. Zhang,[62b] Y. Zhang,[62c,5] Y. Zhang,[96] Z. Zhang,[17a] Z. Zhang,[66] H. Zhao,[138] P. Zhao,[51] T. Zhao,[62b] Y. Zhao,[136] Z. Zhao,[62a] A. Zhemchugov,[38] J. Zheng,[14c] K. Zheng,[162] X. Zheng,[62a] Z. Zheng,[143] D. Zhong,[162] B. Zhou,[106] H. Zhou,[7] N. Zhou,[62c] Y. Zhou,[7] C. G. Zhu,[62b] J. Zhu,[106] Y. Zhu,[62c] Y. Zhu,[62a] X. Zhuang,[14a] K. Zhukov,[37] V. Zhulanov,[37] N. I. Zimine,[38] J. Zinsser,[63b] M. Ziolkowski,[141] L. Živković,[15] A. Zoccoli,[23b,23a] K. Zoch,[56] T. G. Zorbas,[139] O. Zormpa,[46] W. Zou,[41] and L. Zwalinski[36]

(ATLAS Collaboration)

[1]*Department of Physics, University of Adelaide, Adelaide, Australia*
[2]*Department of Physics, University of Alberta, Edmonton, Alberta, Canada*
[3a]*Department of Physics, Ankara University, Ankara, Türkiye*
[3b]*Division of Physics, TOBB University of Economics and Technology, Ankara, Türkiye*
[4]*LAPP, Université Savoie Mont Blanc, CNRS/IN2P3, Annecy, France*
[5]*APC, Université Paris Cité, CNRS/IN2P3, Paris, France*
[6]*High Energy Physics Division, Argonne National Laboratory, Argonne, Illinois, USA*
[7]*Department of Physics, University of Arizona, Tucson, Arizona, USA*
[8]*Department of Physics, University of Texas at Arlington, Arlington, Texas, USA*
[9]*Physics Department, National and Kapodistrian University of Athens, Athens, Greece*
[10]*Physics Department, National Technical University of Athens, Zografou, Greece*
[11]*Department of Physics, University of Texas at Austin, Austin, Texas, USA*
[12]*Institute of Physics, Azerbaijan Academy of Sciences, Baku, Azerbaijan*
[13]*Institut de Física d'Altes Energies (IFAE), Barcelona Institute of Science and Technology, Barcelona, Spain*
[14a]*Institute of High Energy Physics, Chinese Academy of Sciences, Beijing, China*
[14b]*Physics Department, Tsinghua University, Beijing, China*
[14c]*Department of Physics, Nanjing University, Nanjing, China*
[14d]*School of Science, Shenzhen Campus of Sun Yat-sen University, China*
[14e]*University of Chinese Academy of Science (UCAS), Beijing, China*
[15]*Institute of Physics, University of Belgrade, Belgrade, Serbia*
[16]*Department for Physics and Technology, University of Bergen, Bergen, Norway*
[17a]*Physics Division, Lawrence Berkeley National Laboratory, Berkeley, California, USA*
[17b]*University of California, Berkeley, California, USA*
[18]*Institut für Physik, Humboldt Universität zu Berlin, Berlin, Germany*
[19]*Albert Einstein Center for Fundamental Physics and Laboratory for High Energy Physics, University of Bern, Bern, Switzerland*
[20]*School of Physics and Astronomy, University of Birmingham, Birmingham, United Kingdom*
[21a]*Department of Physics, Bogazici University, Istanbul, Türkiye*
[21b]*Department of Physics Engineering, Gaziantep University, Gaziantep, Türkiye*
[21c]*Department of Physics, Istanbul University, Istanbul, Türkiye*
[22a]*Facultad de Ciencias y Centro de Investigaciónes, Universidad Antonio Nariño, Bogotá, Colombia*
[22b]*Departamento de Física, Universidad Nacional de Colombia, Bogotá, Colombia*
[23a]*Dipartimento di Fisica e Astronomia A. Righi, Università di Bologna, Bologna, Italy*
[23b]*INFN Sezione di Bologna, Italy*
[24]*Physikalisches Institut, Universität Bonn, Bonn, Germany*
[25]*Department of Physics, Boston University, Boston, Massachusetts, USA*
[26]*Department of Physics, Brandeis University, Waltham, Massachusetts, USA*

[27a]Transilvania University of Brasov, Brasov, Romania
[27b]Horia Hulubei National Institute of Physics and Nuclear Engineering, Bucharest, Romania
[27c]Department of Physics, Alexandru Ioan Cuza University of Iasi, Iasi, Romania
[27d]National Institute for Research and Development of Isotopic and Molecular Technologies, Physics Department, Cluj-Napoca, Romania
[27e]National University of Science and Technology Politechnica, Bucharest, Romania
[27f]West University in Timisoara, Timisoara, Romania
[27g]Faculty of Physics, University of Bucharest, Bucharest, Romania
[28a]Faculty of Mathematics, Physics and Informatics, Comenius University, Bratislava, Slovak Republic
[28b]Department of Subnuclear Physics, Institute of Experimental Physics of the Slovak Academy of Sciences, Kosice, Slovak Republic
[29]Physics Department, Brookhaven National Laboratory, Upton, New York, USA
[30]Universidad de Buenos Aires, Facultad de Ciencias Exactas y Naturales, Departamento de Física, y CONICET, Instituto de Física de Buenos Aires (IFIBA), Buenos Aires, Argentina
[31]California State University, California, USA
[32]Cavendish Laboratory, University of Cambridge, Cambridge, United Kingdom
[33a]Department of Physics, University of Cape Town, Cape Town, South Africa
[33b]iThemba Labs, Western Cape, South Africa
[33c]Department of Mechanical Engineering Science, University of Johannesburg, Johannesburg, South Africa
[33d]National Institute of Physics, University of the Philippines Diliman (Philippines), Philippines
[33e]University of South Africa, Department of Physics, Pretoria, South Africa
[33f]University of Zululand, KwaDlangezwa, South Africa
[33g]School of Physics, University of the Witwatersrand, Johannesburg, South Africa
[34]Department of Physics, Carleton University, Ottawa, Ontario, Canada
[35a]Faculté des Sciences Ain Chock, Réseau Universitaire de Physique des Hautes Energies—Université Hassan II, Casablanca, Morocco
[35b]Faculté des Sciences, Université Ibn-Tofail, Kénitra, Morocco
[35c]Faculté des Sciences Semlalia, Université Cadi Ayyad, LPHEA-Marrakech, Morocco
[35d]LPMR, Faculté des Sciences, Université Mohamed Premier, Oujda, Morocco
[35e]Faculté des sciences, Université Mohammed V, Rabat, Morocco
[35f]Institute of Applied Physics, Mohammed VI Polytechnic University, Ben Guerir, Morocco
[36]CERN, Geneva, Switzerland
[37]Affiliated with an institute covered by a cooperation agreement with CERN
[38]Affiliated with an international laboratory covered by a cooperation agreement with CERN
[39]Enrico Fermi Institute, University of Chicago, Chicago, Illinois, USA
[40]LPC, Université Clermont Auvergne, CNRS/IN2P3, Clermont-Ferrand, France
[41]Nevis Laboratory, Columbia University, Irvington New York, USA
[42]Niels Bohr Institute, University of Copenhagen, Copenhagen, Denmark
[43a]Dipartimento di Fisica, Università della Calabria, Rende, Italy
[43b]INFN Gruppo Collegato di Cosenza, Laboratori Nazionali di Frascati, Italy
[44]Physics Department, Southern Methodist University, Dallas, Texas, USA
[45]Physics Department, University of Texas at Dallas, Richardson, Texas, USA
[46]National Centre for Scientific Research "Demokritos", Agia Paraskevi, Greece
[47a]Department of Physics, Stockholm University, Sweden
[47b]Oskar Klein Centre, Stockholm, Sweden
[48]Deutsches Elektronen-Synchrotron DESY, Hamburg and Zeuthen, Germany
[49]Fakultät Physik, Technische Universität Dortmund, Dortmund, Germany
[50]Institut für Kern- und Teilchenphysik, Technische Universität Dresden, Dresden, Germany
[51]Department of Physics, Duke University, Durham, North Carolina, USA
[52]SUPA—School of Physics and Astronomy, University of Edinburgh, Edinburgh, United Kingdom
[53]INFN e Laboratori Nazionali di Frascati, Frascati, Italy
[54]Physikalisches Institut, Albert-Ludwigs-Universität Freiburg, Freiburg, Germany
[55]II. Physikalisches Institut, Georg-August-Universität Göttingen, Göttingen, Germany
[56]Département de Physique Nucléaire et Corpusculaire, Université de Genève, Genève, Switzerland
[57a]Dipartimento di Fisica, Università di Genova, Genova, Italy
[57b]INFN Sezione di Genova, Italy
[58]II. Physikalisches Institut, Justus-Liebig-Universität Giessen, Giessen, Germany
[59]SUPA—School of Physics and Astronomy, University of Glasgow, Glasgow, United Kingdom
[60]LPSC, Université Grenoble Alpes, CNRS/IN2P3, Grenoble INP, Grenoble, France

[61]*Laboratory for Particle Physics and Cosmology, Harvard University, Cambridge, Massachusetts, USA*
[62a]*Department of Modern Physics and State Key Laboratory of Particle Detection and Electronics, University of Science and Technology of China, Hefei, China*
[62b]*Institute of Frontier and Interdisciplinary Science and Key Laboratory of Particle Physics and Particle Irradiation (MOE), Shandong University, Qingdao, China*
[62c]*School of Physics and Astronomy, Shanghai Jiao Tong University, Key Laboratory for Particle Astrophysics and Cosmology (MOE), SKLPPC, Shanghai, China*
[62d]*Tsung-Dao Lee Institute, Shanghai, China*
[63a]*Kirchhoff-Institut für Physik, Ruprecht-Karls-Universität Heidelberg, Heidelberg, Germany*
[63b]*Physikalisches Institut, Ruprecht-Karls-Universität Heidelberg, Heidelberg, Germany*
[64a]*Department of Physics, Chinese University of Hong Kong, Shatin, N.T., Hong Kong, China*
[64b]*Department of Physics, University of Hong Kong, Hong Kong, China*
[64c]*Department of Physics and Institute for Advanced Study, Hong Kong University of Science and Technology, Clear Water Bay, Kowloon, Hong Kong, China*
[65]*Department of Physics, National Tsing Hua University, Hsinchu, Taiwan*
[66]*IJCLab, Université Paris-Saclay, CNRS/IN2P3, 91405, Orsay, France*
[67]*Centro Nacional de Microelectrónica (IMB-CNM-CSIC), Barcelona, Spain*
[68]*Department of Physics, Indiana University, Bloomington, Indiana, USA*
[69a]*INFN Gruppo Collegato di Udine, Sezione di Trieste, Udine, Italy*
[69b]*ICTP, Trieste, Italy*
[69c]*Dipartimento Politecnico di Ingegneria e Architettura, Università di Udine, Udine, Italy*
[70a]*INFN Sezione di Lecce, Italy*
[70b]*Dipartimento di Matematica e Fisica, Università del Salento, Lecce, Italy*
[71a]*INFN Sezione di Milano, Italy*
[71b]*Dipartimento di Fisica, Università di Milano, Milano, Italy*
[72a]*INFN Sezione di Napoli, Italy*
[72b]*Dipartimento di Fisica, Università di Napoli, Napoli, Italy*
[73a]*INFN Sezione di Pavia, Italy*
[73b]*Dipartimento di Fisica, Università di Pavia, Pavia, Italy*
[74a]*INFN Sezione di Pisa, Italy*
[74b]*Dipartimento di Fisica E. Fermi, Università di Pisa, Pisa, Italy*
[75a]*INFN Sezione di Roma, Italy*
[75b]*Dipartimento di Fisica, Sapienza Università di Roma, Roma, Italy*
[76a]*INFN Sezione di Roma Tor Vergata, Italy*
[76b]*Dipartimento di Fisica, Università di Roma Tor Vergata, Roma, Italy*
[77a]*INFN Sezione di Roma Tre, Italy*
[77b]*Dipartimento di Matematica e Fisica, Università Roma Tre, Roma, Italy*
[78a]*INFN-TIFPA, Italy*
[78b]*Università degli Studi di Trento, Trento, Italy*
[79]*Universität Innsbruck, Department of Astro and Particle Physics, Innsbruck, Austria*
[80]*University of Iowa, Iowa City, Iowa, USA*
[81]*Department of Physics and Astronomy, Iowa State University, Ames, Iowa, USA*
[82]*Istinye University, Sariyer, Istanbul, Türkiye*
[83a]*Departamento de Engenharia Elétrica, Universidade Federal de Juiz de Fora (UFJF), Juiz de Fora, Brazil*
[83b]*Universidade Federal do Rio De Janeiro COPPE/EE/IF, Rio de Janeiro, Brazil*
[83c]*Instituto de Física, Universidade de São Paulo, São Paulo, Brazil*
[83d]*Rio de Janeiro State University, Rio de Janeiro, Brazil*
[84]*KEK, High Energy Accelerator Research Organization, Tsukuba, Japan*
[85]*Graduate School of Science, Kobe University, Kobe, Japan*
[86a]*AGH University of Krakow, Faculty of Physics and Applied Computer Science, Krakow, Poland*
[86b]*Marian Smoluchowski Institute of Physics, Jagiellonian University, Krakow, Poland*
[87]*Institute of Nuclear Physics Polish Academy of Sciences, Krakow, Poland*
[88]*Faculty of Science, Kyoto University, Kyoto, Japan*
[89]*Research Center for Advanced Particle Physics and Department of Physics, Kyushu University, Fukuoka, Japan*
[90]*Instituto de Física La Plata, Universidad Nacional de La Plata and CONICET, La Plata, Argentina*
[91]*Physics Department, Lancaster University, Lancaster, United Kingdom*
[92]*Oliver Lodge Laboratory, University of Liverpool, Liverpool, United Kingdom*

[93]Department of Experimental Particle Physics, Jožef Stefan Institute and Department of Physics, University of Ljubljana, Ljubljana, Slovenia
[94]School of Physics and Astronomy, Queen Mary University of London, London, United Kingdom
[95]Department of Physics, Royal Holloway University of London, Egham, United Kingdom
[96]Department of Physics and Astronomy, University College London, London, United Kingdom
[97]Louisiana Tech University, Ruston, Los Angeles, USA
[98]Fysiska institutionen, Lunds universitet, Lund, Sweden
[99]Departamento de Física Teorica C-15 and CIAFF, Universidad Autónoma de Madrid, Madrid, Spain
[100]Institut für Physik, Universität Mainz, Mainz, Germany
[101]School of Physics and Astronomy, University of Manchester, Manchester, United Kingdom
[102]CPPM, Aix-Marseille Université, CNRS/IN2P3, Marseille, France
[103]Department of Physics, University of Massachusetts, Amherst, Massachusetts, USA
[104]Department of Physics, McGill University, Montreal, Quebec, Canada
[105]School of Physics, University of Melbourne, Victoria, Australia
[106]Department of Physics, University of Michigan, Ann Arbor, Michigan, USA
[107]Department of Physics and Astronomy, Michigan State University, East Lansing, Michigan, USA
[108]Group of Particle Physics, University of Montreal, Montreal, Quebec, Canada
[109]Fakultät für Physik, Ludwig-Maximilians-Universität München, München, Germany
[110]Max-Planck-Institut für Physik (Werner-Heisenberg-Institut), München, Germany
[111]Graduate School of Science and Kobayashi-Maskawa Institute, Nagoya University, Nagoya, Japan
[112]Department of Physics and Astronomy, University of New Mexico, Albuquerque, New Mexico, USA
[113]Institute for Mathematics, Astrophysics and Particle Physics, Radboud University/Nikhef, Nijmegen, Netherlands
[114]Nikhef National Institute for Subatomic Physics and University of Amsterdam, Amsterdam, Netherlands
[115]Department of Physics, Northern Illinois University, DeKalb, Illinois, USA
[116a]New York University Abu Dhabi, Abu Dhabi, United Arab Emirates
[116b]University of Sharjah, Sharjah, United Arab Emirates
[117]Department of Physics, New York University, New York, New York, USA
[118]Ochanomizu University, Otsuka, Bunkyo-ku, Tokyo, Japan
[119]Ohio State University, Columbus, Ohio, USA
[120]Homer L. Dodge Department of Physics and Astronomy, University of Oklahoma, Norman, Oklahoma, USA
[121]Department of Physics, Oklahoma State University, Stillwater, Oklahoma, USA
[122]Palacký University, Joint Laboratory of Optics, Olomouc, Czech Republic
[123]Institute for Fundamental Science, University of Oregon, Eugene, Oregon, USA
[124]Graduate School of Science, Osaka University, Osaka, Japan
[125]Department of Physics, University of Oslo, Oslo, Norway
[126]Department of Physics, Oxford University, Oxford, United Kingdom
[127]LPNHE, Sorbonne Université, Université Paris Cité, CNRS/IN2P3, Paris, France
[128]Department of Physics, University of Pennsylvania, Philadelphia, Pennsylvania, USA
[129]Department of Physics and Astronomy, University of Pittsburgh, Pittsburgh, Pennsylvania, USA
[130a]Laboratório de Instrumentação e Física Experimental de Partículas—LIP, Lisboa, Portugal
[130b]Departamento de Física, Faculdade de Ciências, Universidade de Lisboa, Lisboa, Portugal
[130c]Departamento de Física, Universidade de Coimbra, Coimbra, Portugal
[130d]Centro de Física Nuclear da Universidade de Lisboa, Lisboa, Portugal
[130e]Departamento de Física, Universidade do Minho, Braga, Portugal
[130f]Departamento de Física Teórica y del Cosmos, Universidad de Granada, Granada (Spain), Spain
[130g]Departamento de Física, Instituto Superior Técnico, Universidade de Lisboa, Lisboa, Portugal
[131]Institute of Physics of the Czech Academy of Sciences, Prague, Czech Republic
[132]Czech Technical University in Prague, Prague, Czech Republic
[133]Charles University, Faculty of Mathematics and Physics, Prague, Czech Republic
[134]Particle Physics Department, Rutherford Appleton Laboratory, Didcot, United Kingdom
[135]IRFU, CEA, Université Paris-Saclay, Gif-sur-Yvette, France
[136]Santa Cruz Institute for Particle Physics, University of California Santa Cruz, Santa Cruz, California, USA
[137a]Departamento de Física, Pontificia Universidad Católica de Chile, Santiago, Chile
[137b]Millennium Institute for Subatomic physics at high energy frontier (SAPHIR), Santiago, Chile
[137c]Instituto de Investigación Multidisciplinario en Ciencia y Tecnología, y Departamento de Física, Universidad de La Serena, Chile
[137d]Universidad Andres Bello, Department of Physics, Santiago, Chile

[137e]*Instituto de Alta Investigación, Universidad de Tarapacá, Arica, Chile*
[137f]*Departamento de Física, Universidad Técnica Federico Santa María, Valparaíso, Chile*
[138]*Department of Physics, University of Washington, Seattle, Washington, USA*
[139]*Department of Physics and Astronomy, University of Sheffield, Sheffield, United Kingdom*
[140]*Department of Physics, Shinshu University, Nagano, Japan*
[141]*Department Physik, Universität Siegen, Siegen, Germany*
[142]*Department of Physics, Simon Fraser University, Burnaby, British Columbia, Canada*
[143]*SLAC National Accelerator Laboratory, Stanford, California, USA*
[144]*Department of Physics, Royal Institute of Technology, Stockholm, Sweden*
[145]*Departments of Physics and Astronomy, Stony Brook University, Stony Brook, New York, USA*
[146]*Department of Physics and Astronomy, University of Sussex, Brighton, United Kingdom*
[147]*School of Physics, University of Sydney, Sydney, Australia*
[148]*Institute of Physics, Academia Sinica, Taipei, Taiwan*
[149a]*E. Andronikashvili Institute of Physics, Iv. Javakhishvili Tbilisi State University, Tbilisi, Georgia*
[149b]*High Energy Physics Institute, Tbilisi State University, Tbilisi, Georgia*
[149c]*University of Georgia, Tbilisi, Georgia*
[150]*Department of Physics, Technion, Israel Institute of Technology, Haifa, Israel*
[151]*Raymond and Beverly Sackler School of Physics and Astronomy, Tel Aviv University, Tel Aviv, Israel*
[152]*Department of Physics, Aristotle University of Thessaloniki, Thessaloniki, Greece*
[153]*International Center for Elementary Particle Physics and Department of Physics, University of Tokyo, Tokyo, Japan*
[154]*Department of Physics, Tokyo Institute of Technology, Tokyo, Japan*
[155]*Department of Physics, University of Toronto, Toronto, Ontario, Canada*
[156a]*TRIUMF, Vancouver, British Columbia, Canada*
[156b]*Department of Physics and Astronomy, York University, Toronto, Ontario, Canada*
[157]*Division of Physics and Tomonaga Center for the History of the Universe, Faculty of Pure and Applied Sciences, University of Tsukuba, Tsukuba, Japan*
[158]*Department of Physics and Astronomy, Tufts University, Medford, Massachusetts, USA*
[159]*United Arab Emirates University, Al Ain, United Arab Emirates*
[160]*Department of Physics and Astronomy, University of California Irvine, Irvine, California, USA*
[161]*Department of Physics and Astronomy, University of Uppsala, Uppsala, Sweden*
[162]*Department of Physics, University of Illinois, Urbana, Illinois, USA*
[163]*Instituto de Física Corpuscular (IFIC), Centro Mixto Universidad de Valencia—CSIC, Valencia, Spain*
[164]*Department of Physics, University of British Columbia, Vancouver, British Columbia, Canada*
[165]*Department of Physics and Astronomy, University of Victoria, Victoria, British Columbia, Canada*
[166]*Fakultät für Physik und Astronomie, Julius-Maximilians-Universität Würzburg, Würzburg, Germany*
[167]*Department of Physics, University of Warwick, Coventry, United Kingdom*
[168]*Waseda University, Tokyo, Japan*
[169]*Department of Particle Physics and Astrophysics, Weizmann Institute of Science, Rehovot, Israel*
[170]*Department of Physics, University of Wisconsin, Madison, Wisconsin, USA*
[171]*Fakultät für Mathematik und Naturwissenschaften, Fachgruppe Physik, Bergische Universität Wuppertal, Wuppertal, Germany*
[172]*Department of Physics, Yale University, New Haven, Connecticut, USA*

[a]Deceased.
[b]Also at Department of Physics, King's College London, London, United Kingdom.
[c]Also at Institute of Physics, Azerbaijan Academy of Sciences, Baku, Azerbaijan.
[d]Also at Lawrence Livermore National Laboratory, Livermore, USA.
[e]Also at TRIUMF, Vancouver, British Columbia, Canada.
[f]Also at Department of Physics, University of Thessaly, Greece.
[g]Also at An-Najah National University, Nablus, Palestine.
[h]Also at Department of Physics, University of Fribourg, Fribourg, Switzerland.
[i]Also at University of Colorado Boulder, Department of Physics, Colorado, USA.
[j]Also at Department of Physics, Westmont College, Santa Barbara, USA.
[k]Also at Departament de Fisica de la Universitat Autonoma de Barcelona, Barcelona, Spain.
[l]Also at Affiliated with an institute covered by a cooperation agreement with CERN.
[m]Also at The Collaborative Innovation Center of Quantum Matter (CICQM), Beijing, China.
[n]Also at Department of Physics, Ben Gurion University of the Negev, Beer Sheva, Israel.
[o]Also at Università di Napoli Parthenope, Napoli, Italy.
[p]Also at Institute of Particle Physics (IPP), Canada.

[q]Also at Borough of Manhattan Community College, City University of New York, New York, New York, USA.
[r]Also at National Institute of Physics, University of the Philippines Diliman (Philippines), Philippines.
[s]Also at Department of Financial and Management Engineering, University of the Aegean, Chios, Greece.
[t]Also at Ochanomizu University, Otsuka, Bunkyo-ku, Tokyo, Japan.
[u]Also at Department of Physics, Stanford University, Stanford, California, USA.
[v]Also at Centro Studi e Ricerche Enrico Fermi, Italy.
[w]Also at Institucio Catalana de Recerca i Estudis Avancats, ICREA, Barcelona, Spain.
[x]Also at Technical University of Munich, Munich, Germany.
[y]Also at Yeditepe University, Physics Department, Istanbul, Türkiye.
[z]Also at Institute of Theoretical Physics, Ilia State University, Tbilisi, Georgia.
[aa]Also at CERN, Geneva, Switzerland.
[bb]Also at Center for Interdisciplinary Research and Innovation (CIRI-AUTH), Thessaloniki, Greece.
[cc]Also at Hellenic Open University, Patras, Greece.
[dd]Also at Center for High Energy Physics, Peking University, China.
[ee]Also at L2IT, Université de Toulouse, CNRS/IN2P3, UPS, Toulouse, France.
[ff]Also at Department of Physics, California State University, Sacramento, USA.
[gg]Also at Département de Physique Nucléaire et Corpusculaire, Université de Genève, Genève, Switzerland.
[hh]Also at Institut für Experimentalphysik, Universität Hamburg, Hamburg, Germany.
[ii]Also at Institute for Nuclear Research and Nuclear Energy (INRNE) of the Bulgarian Academy of Sciences, Sofia, Bulgaria.
[jj]Also at Washington College, Chestertown, Maryland, USA.
[kk]Also at Institute of Applied Physics, Mohammed VI Polytechnic University, Ben Guerir, Morocco.
[ll]Also at Institute of Physics and Technology, Mongolian Academy of Sciences, Ulaanbaatar, Mongolia.
[mm]Also at Department of Physics and Astronomy, Michigan State University, East Lansing, Michigan, USA.